

AIRMI-HAWK



REMOVE BEFORE FLIGHT

ARM-Hawk

This work forms the thorough description of my bachelor's thesis "Stall Protection System for a Remotely Controlled Airplane", conducted at the Technical University Vienna (TU Wien). It is part of the ARM-Hawk project. Both this work and the ARM-Hawk project are released under the GNU General Public License v3.0.

Daniel Pusztai

13.12.2018

Contents

1 Introduction	1
2 Modeling the Aircraft	4
2.1 Propulsive Forces and Moments	4
2.1.1 Energy and Momentum Balance	4
2.1.2 Forces and Moments at the Propeller Hub.....	7
2.1.3 Electric Drive System.....	12
2.2 Aerodynamic Forces and Moments	12
2.2.1 Section Coefficients.....	13
2.2.2 Wing coefficients.....	15
2.2.3 Vehicle coefficients.....	18
2.3 Assembling the Model.....	22
3 Flight Hardware	24
3.1 Airframe.....	24
3.2 Flight Computer	25
3.3 Air Data Sensor Unit.....	26
3.4 Inertial Navigation System	31
3.4.1 Inertial Measurement Unit	33
3.4.2 Measuring the Vehicle's Attitude	37
3.4.3 State Estimation with Kalman Filter	40
3.5 RPM Sensor	45
4 Lateral Stability Augmentation	47
4.1 Linearized Dynamics.....	48
4.2 Controller Design.....	49
4.2.1 Roll Damper	50
4.2.2 Bank Controller.....	50

4.2.3 Yaw Damper	51
4.2.4 Turn Coordinator	51
4.3 Flight Test Results.....	53
5 Stall Protection	55
5.1 Longitudinal State Space Model	56
5.2 Control Laws.....	58
5.2.1 Standby Mode	59
5.2.2 α -Hold Mode.....	59
5.2.3 γ -Hold Mode.....	60
5.3 Flight Test Results.....	60
A Nomenclature	63
B Propulsion Data	67
B.1 Propeller Disk Air Velocity State.....	67
B.2 Thrust Coefficients.....	68
B.3 Powertrain.....	73
C Aerodynamic Data	74
C.1 Main Wing	75
C.2 Horizontal Stabilizer	77
C.3 Vertical Stabilizer	79
C.4 Parasitic Drag	81
C.5 Aerodynamic Coefficients of the Vehicle	82
D INS Parameters	84
E Complete Simulink Model	86
F Technical Drawings	87
References	91

Chapter 1

Introduction

To avoid a stall, the angle of attack (AOA) of an airplane must not exceed the critical one. Some large jet- or propeller-powered multi engine aircrafts employ control systems that effectively limit the AOA in an approaching stall. These systems usually employ a feedback control on the elevator and an independent open loop control for the throttle [1, pp.862-863, 871]. For single engine propeller-driven airplanes the complexity of the stall situation increases as the airflow around the inner wing sections and the empennage is severely affected by the prop wash. Especially large propellers with a high-power drive system can cause a strong asymmetry in the aerodynamic condition of the plane and parts of the airplane's lifting surface may experience a flow separation before others. Additionally, a single large propeller at the nose of an aircraft decreases the aerodynamic stability of the aircraft at low airspeeds [2, pp.637]. Both effects impose big unexpected moments on the vehicle, which can easily lead to a complete loss of control.

The stall protection system is developed for a single motor electric airplane with a wingspan of 1.5 m, a mass of 6.5kg and a thrust to weight ratio of 1.4 (Figure 1.1). Due to the relatively small wing area and the very large propeller this plane abruptly rolls on its back and loses altitude rapidly as soon as it stalls. It is therefore crucial to develop an accurate model of the propulsive system, including forces and moments acting on the propeller, as well as the prop wash. This is done in Chapter 2.1 by performing an analytic integration of the blade sections, involving simplified nonlinear aerodynamics to account for partial propeller stalls, as they occur at low airspeeds. The equations are then linearized yielding a reference set of equations for thrust and torque and a perturbation set of equations for the forces and moments in radial directions. The unknown parameters have been fixed by performing a series of static thrust tests. Following is an analysis of the vehicle's aerodynamics. The methods used mainly follow the approach

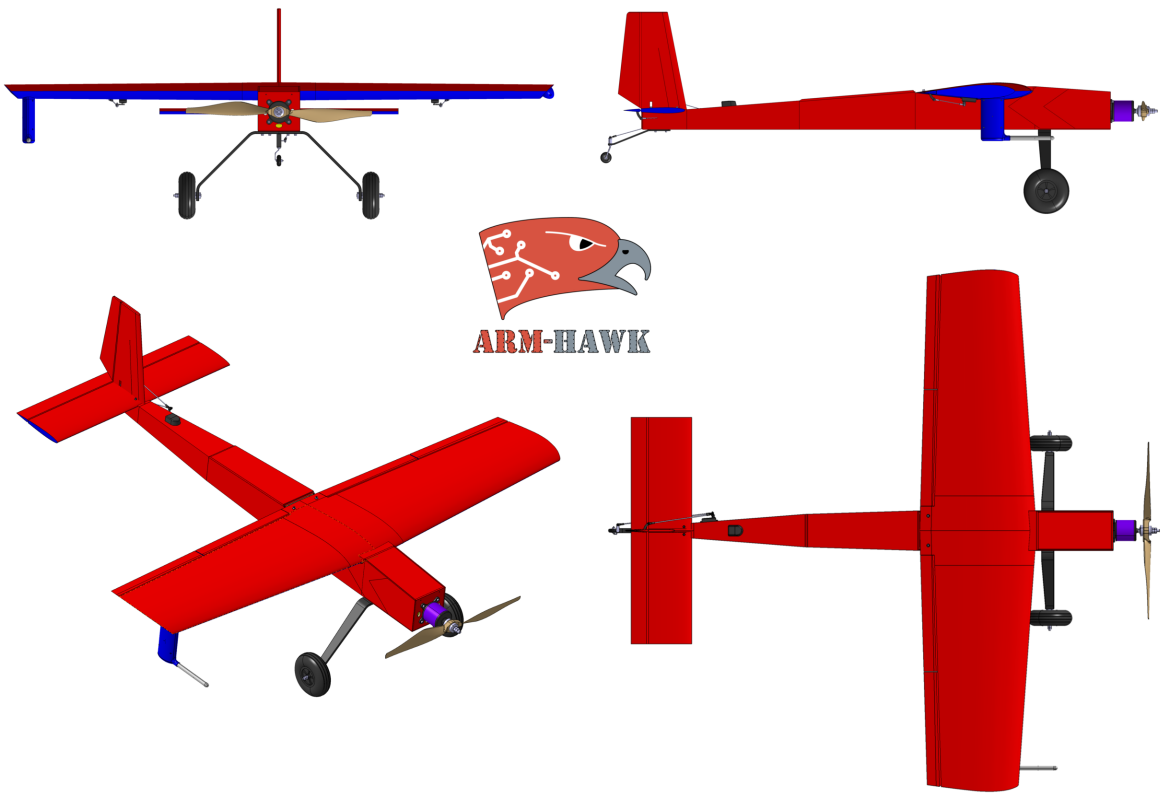


Figure 1.1: ARM-Hawk Airframe

described in [3]. Firstly, aerodynamic polar diagrams are numerically computed for the two-dimensional wing sections using *ANSYS*. These datasets are then numerically integrated over the wingspan to yield the aerodynamic coefficients for the three-dimensional wing. Finally all lifting surfaces are combined to obtain the vehicle's six aerodynamic coefficients in dependence of the air velocity vector, control surface deflections and the prop wash. A nonlinear Simulink model of the complete aircraft is assembled at the end of the chapter.

Chapter 3 deals with the task of building a flight computer and associated hardware which can measure the complete state vector with high precision. The most important task is the measurement of the AOA. Due to the small scale of the airplane traditional alpha vanes [1 pp.372-373] are not feasible. An alternative approach has been taken, by developing a 5-hole spherical pressure probe, as used in wind tunnel measurements [4, pp.159-162], [5, pp.384]. To shorten the development time a thorough wind tunnel calibration of the probe has been skipped and a numerical simulation formed the foundation for the probe's characteristics. Chapter 3.4 deals with the estimation of the inertial state.

Commercial Inertial Navigation Systems (INS) are too big to be fitted into the plane, whereas smaller and cheaper units do not work accurately enough in a highly dynamic environment, as it is the case with this airplane. To overcome these problems, the state estimation has to be performed by the flight computer. The data for this task comes from a set of small consumer-grade sensors which have been extensively calibrated. The sensor's data are processed at different sample times and combined with two extended Kalman filters. The chapter ends with the construction of an electronic RPM sensor to measure the motor speed, which will be needed by the stall protection later on.

The strong asymmetry, the prop wash induces in the vehicle's aerodynamics, has to be eliminated. This is done by designing a set of controllers for the lateral motion of the plane in chapter 4, called the Stability Augmentation System (SAS). It ensures aerodynamic symmetry by reducing the sideslip angle to zero. Additionally, the SAS provides bank angle control to limit the flight envelope during the operation of the stall protection system, as well as improving handling qualities at low-speed flight. The SAS is gain-scheduled to ensure identical dynamics at the whole range of flight speeds.

The design of the stall protection is described in chapter 5, along with the necessary linearization of the longitudinal dynamics. An optimal trajectory is discussed, to transition the plane from the approaching stall back to a safe state. Based on that trajectory, a dead-beat controller is designed which applies power to the motor and flies the plane at maximum AOA until a minimum positive climb gradient is achieved. To ensure correct operation of the controller at a variety of flight states, the underlying linear state space model is parametrized.

The appendix closes this work by summarizing the used nomenclature, as well as describing how the parameter identification for the nonlinear model was done.

The source code of the developed flight computer is available at the project's *GitHub* page. Videos of the flight tests can be found at the project's *YouTube* channel.



[GitHub project page](#)



[YouTube channel](#)

Chapter 2

Modeling the Aircraft

2.1 Propulsive Forces and Moments

The forces and moments on the propeller are calculated by combining an expanded version of Froude's momentum theory [5, pp.126], [6, pp.108-111] with the blade element theory [2, pp.634], [4, pp.109].

2.1.1 Energy and Momentum Balance

Figure 2.1 shows the idealized streamtube for the flow through an infinitely thin rotor disk (Station 1). Station 0 represents the flow ahead of the propeller, station

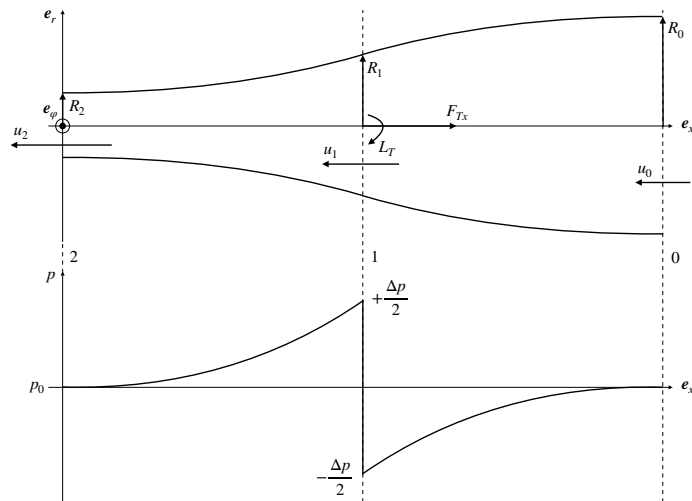


Figure 2.1: Streamtube through propeller disk

2 the flow downstream of it. The static pressure at station 0 and 2 equals the ambient pressure. The classic momentum theory is expanded by including the flow vorticity induced by the propeller. A rigid-body vortex is assumed. Furthermore, it is assumed that forces and moments in radial propeller directions do not impact the shape of the streamline¹ and can therefore be neglected in the following calculations. Momentum, angular momentum and energy balance can be written as [6, pp.73-74]:

$$\int_A \rho \mathbf{u} \mathbf{u} \cdot d\mathbf{A} + \int_A p d\mathbf{A} = \mathbf{F}_T \quad (2.1)$$

$$\int_A (\rho \mathbf{x} \times \mathbf{u}) \mathbf{u} \cdot d\mathbf{A} = \mathbf{M}_T \quad (2.2)$$

$$\int_A \rho \left(\frac{\mathbf{u}^2}{2} + h + gz \right) \mathbf{u} \cdot d\mathbf{A} = \dot{Q} \quad (2.3)$$

Here A is the surface area of the integrated volume, \mathbf{u} the air velocity vector, \mathbf{x} a position vector, h the specific enthalpy, z the potential height and \dot{Q} the added power. Substituting the velocity ansatz

$$\mathbf{u} = -u \mathbf{e}_x + \Omega r \mathbf{e}_\varphi$$

into equations (2.1) and (2.2), and evaluating the integrals between station 0 and 2 yields the propeller's axial thrust and torque:

$$F_{Tx} = \rho \dot{V} (u_2 - u_0) \quad (2.4)$$

$$L_T = -\frac{\rho}{2} \dot{V} \Omega_2 R_2^2 \quad (2.5)$$

Integrating (2.3) by assuming a constant specific internal energy e

$$h = e + \frac{p}{\rho} \quad e = \text{const.}$$

and taking the energy balance between 0 and 2 yields:

$$\rho \dot{V} \left(\frac{\Omega_2^2}{4} R_2^2 + \frac{u_2^2}{2} - \frac{u_0^2}{2} \right) = P_{mech} = -L_T \omega_P \quad (2.6)$$

P_{mech} is the mechanical power delivered to the propeller by the motor and ω_P is the propeller's angular velocity. (2.6) is based on the assumption that the vorticity ahead of the streamtube Ω_0 is zero. If we furthermore assume that there is no

¹ Although there clearly has to be some form of deviation to produce radial forces and moments

energy exchange between the translational and rotational components of \mathbf{u} , we can repeat the calculation of (2.6) while neglecting the rotational components of \mathbf{u} :

$$\rho \dot{V} \left(\frac{u_2^2}{2} - \frac{u_0^2}{2} \right) = P_{mech} \eta_{prop} = - F_{Tx} u_1 \quad (2.7)$$

Substituting (2.4) into (2.6) leads to an expression for the axial velocity u_1 at the rotor disk:

$$u_1 = \frac{u_0 + u_2}{2} \quad (2.8)$$

The angular velocity at the rotor disk Ω_1 can be found by formulating an energy balance at station 1

$$P_{mech} = F_{Tx} u_1 - L_T \Omega_1$$

and substituting (2.5), (2.6), and (2.7) into it:

$$\Omega_1 = \frac{\Omega_2}{2} \quad (2.9)$$

Using (2.4), (2.5), and (2.8) the induced velocity aft of the streamtube can be found as:

$$U_i = u_2 = \sqrt{\frac{2F_{Tx}}{\rho R_1^2 \pi} + u_0^2} \quad (2.10)$$

$$\Omega_i = \Omega_2 = -\frac{2L_T u_2}{\rho \pi u_1^2 R_1^2} \quad (2.11)$$

The aerodynamic efficiency factor of the propeller is found by dividing (2.7) by (2.6):

$$\eta_{prop} = \left| \frac{F_{Tx} u_1}{L_T \omega_P} \right| \quad (2.12)$$

The derived equations are valid as long as following conditions apply:

$$u_0 \geq 0$$

$$F_{Tx} \geq -\rho \pi R_P^2 \frac{u_0^2}{2}$$

2.1.2 Forces and Moments at the Propeller Hub

To simplify the following calculations, a new coordinate system, the hub coordinate system (Figure 2.2), is introduced. It is always aligned with the radial components of the relative air velocity at the hub \mathbf{v}_H , or the radial components of the vehicle's angular velocity $\boldsymbol{\omega}_V$. These two vectors don't align generally, but since the solution will be linearized with respect to these components a separate hub coordinate system for each of them can be used. From here on, though, it will be assumed for reasons of simplicity that the two vectors align². The transformation matrix from the hub coordinate system to the vehicle coordinate system is as follows:

$$T_{VH} = \begin{bmatrix} 1 & 0 & 0 \\ 0 & \cos \psi & -\sin \psi \\ 0 & \sin \psi & \cos \psi \end{bmatrix} \quad (2.13a)$$

$$\sin \psi_V = \frac{W'_H}{\tilde{V}'} \quad / \quad \sin \psi_Q = \frac{R}{\tilde{Q}} \quad (2.13b)$$

$$\cos \psi_V = \frac{V'_H}{\tilde{V}'} \quad / \quad \cos \psi_Q = \frac{Q}{\tilde{Q}} \quad (2.13c)$$

$$\tilde{V}' = \sqrt{V'^2_H + W'^2_H} \quad / \quad \tilde{Q} = \sqrt{Q^2 + R^2} \quad (2.13d)$$

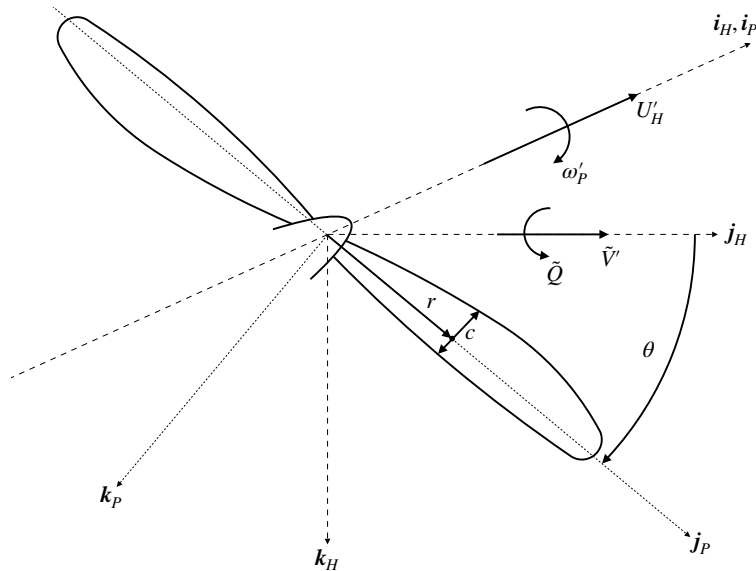


Figure 2.2: Hub coordinate system

² They will be split at the end of the calculations in this chapter

The air velocity at the propeller hub is needed in (2.13) and can be obtained with the hub position vector \mathbf{r}_{HV} and equation (2.8) as follows (small terms are neglected):

$$\mathbf{v}_H^V = \begin{bmatrix} U'_H \\ V'_H \\ W'_H \end{bmatrix} = \mathbf{v}_V^V + \boldsymbol{\omega}_V^V \times \mathbf{r}_{HV}^V = \begin{bmatrix} u_1 \\ V' + RX_H \\ W' - QX_H \end{bmatrix} \quad (2.14)$$

Figure 2.3 shows a cut through a blade section. The coordinate system shown (Index P) is aligned with the rotation axis and the radial blade direction. The forces and moments are given per unit length of propeller blade. \hat{V}_T indicates the projection of the relative air velocity vector at the blade's quarter chord point \mathbf{v}_P^P onto the $i_P - k_P$ plane:

$$\hat{V}_T = \sqrt{U_P'^2 + W_P'^2} \quad (2.15a)$$

$$\mathbf{v}_P^P = \begin{bmatrix} U_P' \\ V_P' \\ W_P' \end{bmatrix} = \begin{bmatrix} U'_H + \tilde{Q}r \sin \theta \\ \tilde{V}' \cos \theta \\ \omega'_P r - \tilde{V}' \sin \theta \end{bmatrix} \quad (2.15b)$$

Here, the relative propeller angular speed ω'_P is needed:

$$\omega'_P = \omega_P - \Omega_1 \quad (2.16)$$

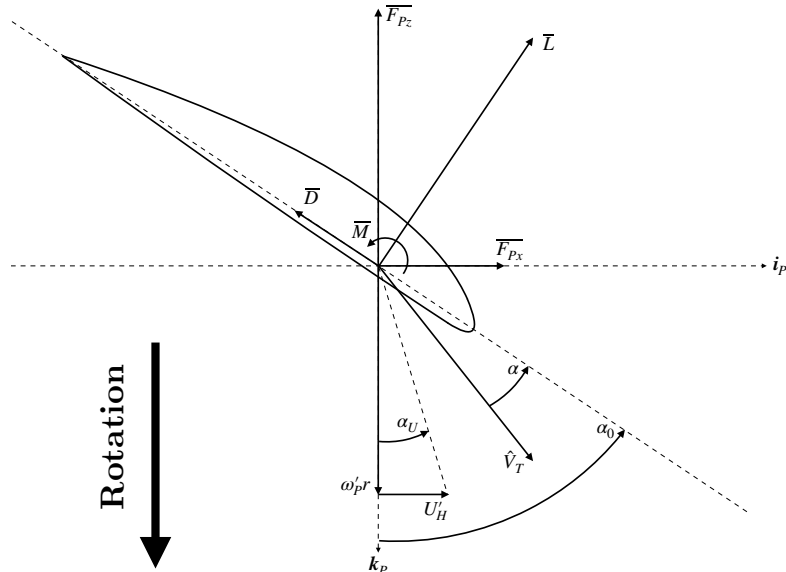


Figure 2.3: Forces and moments on a blade section

The forces at the blade section can now be obtained:

$$\bar{L} = \frac{1}{2} \rho \hat{V}_T^2 c_l(\alpha) c \quad (2.17a)$$

$$\bar{D} = \frac{1}{2} \rho \hat{V}_T^2 c_d(\alpha) c \quad (2.17b)$$

$$\bar{F}_{Px} = \bar{L} \cos(\alpha_0 - \alpha) - \bar{D} \sin(\alpha_0 - \alpha) \quad (2.18a)$$

$$\bar{F}_{Pz} = -\bar{L} \sin(\alpha_0 - \alpha) - \bar{D} \cos(\alpha_0 - \alpha) \quad (2.18b)$$

The blade section moments can be ignored since the opposing propeller blades cancel each other out. The resulting hub forces and moments are obtained by integrating equations (2.18) for N propeller blades and taking the average over one revolution:

$$\mathbf{F}_H^H = \frac{N}{2\pi} \int_0^{2\pi} \int_0^{R_P} \begin{bmatrix} \bar{F}_{Px} \\ -\bar{F}_{Pz} \sin \theta \\ \bar{F}_{Pz} \cos \theta \end{bmatrix} dr d\theta \quad (2.19a)$$

$$\mathbf{M}_H^H = \frac{N}{2\pi} \int_0^{2\pi} \int_0^{R_P} \begin{bmatrix} \bar{F}_{Pz} \\ \bar{F}_{Px} \sin \theta \\ -\bar{F}_{Px} \cos \theta \end{bmatrix} r dr d\theta \quad (2.19b)$$

These will be linearized as follows:

$$\mathbf{F}_H = \mathbf{F}_{H0} + \mathbf{F}_{HV} \tilde{V}' + \mathbf{F}_{HQ} \tilde{Q} \quad (2.20a)$$

$$\mathbf{M}_H = \mathbf{M}_{H0} + \mathbf{M}_{HV} \tilde{V}' + \mathbf{M}_{HQ} \tilde{Q} \quad (2.20b)$$

\mathbf{F}_{H0} and \mathbf{M}_{H0} will only contain axial components and are therefore independent of the coordinate system, whereas $\mathbf{F}_{HV}/\mathbf{M}_{HV}$ and $\mathbf{F}_{HQ}/\mathbf{M}_{HQ}$ will be given in different hub coordinate systems and will need an additional transformation before adding together. For the following calculations, the hub advance ratio J_1 is defined as:

$$J_1 = \frac{U'_H}{\omega_P R_P} \quad (2.21)$$

To evaluate (2.19), the parameters in (2.17) and (2.18) have to be linearized. Firstly, the dynamic pressure

$$q = \frac{1}{2} \rho \hat{V}_T^2$$

is linearized at $V'_H = 0$ and $Q_H = 0$:

$$q_0 = \frac{1}{2} \rho (U_H^2 + \omega_P^2 r^2) = \frac{1}{2} \rho (J_1^2 + \bar{r}^2) \omega_P^2 R_P^2 \quad (2.22a)$$

$$q_V = -\rho \omega'_P r = -\rho \bar{r} \omega'_P R \quad (2.22b)$$

$$q_Q = \rho U'_H r = \rho \bar{r} J_1 \omega'_P R^2 \quad (2.22c)$$

$$q = q_0 + q_V V'_H \sin \theta + q_Q Q_H \sin \theta \quad (2.22d)$$

A similar linearization is obtained for the local angle of attack:

$$\alpha_0 = \arctan\left(\frac{p}{2\pi r}\right) = \arctan\left(\frac{p}{2\pi \bar{r} R}\right) \quad (2.23a)$$

$$\alpha_U = \arctan\left(\frac{U'_H}{\omega'_P r}\right) = \arctan\left(\frac{J_1}{\bar{r}}\right) \quad (2.23b)$$

$$\alpha_V = -\frac{U'_H}{\omega_P^2 r^2 + U_H'^2} = -\frac{J_1}{J_1^2 + \bar{r}^2} \frac{1}{\omega'_P R_P} \quad (2.23c)$$

$$\alpha_Q = -\frac{\omega'_P r^2}{\omega_P^2 r^2 + U_H'^2} = -\frac{\bar{r}^2}{J_1^2 + \bar{r}^2} \frac{1}{\omega'_P} \quad (2.23d)$$

$$\alpha = \alpha_0 - \alpha_U + \alpha_V V'_H \sin \theta + \alpha_Q Q_H \sin \theta \quad (2.23e)$$

The above equations contain the propeller pitch p and the normalized radius $\bar{r} = r/R_P$. Since the blade section aerodynamic coefficients are unknown, a simple linear model for lift and a quadratic model for drag (Figure 2.4) are inserted into (2.17):

$$c_l = \begin{cases} c_{la} \alpha & \text{for } R_{stall} \leq r \leq R_P \\ c_{la} \alpha_{max} & \text{for } 0 \leq r \leq R_{stall} \end{cases} \quad (2.24)$$

$$c_d = c_{da} \alpha^2 \quad (2.25)$$

$$\bar{R}_{stall} = \frac{\frac{p}{R_P} - 2\pi J_1 + \sqrt{\left(\frac{p}{R_P} - 2\pi J_1\right)^2 - 8\pi \frac{p}{R_P} J_1 \tan^2(\alpha_{max})}}{4\pi \tan(\alpha_{max})} \quad (2.26)$$

(2.26) is obtained by setting $\alpha = \alpha_{max}$ in (2.23e). Only the bigger solution is considered, since blade elements near the hub have negligible impacts.

After substituting (2.24) and (2.25) into equations (2.17), equation (2.18) can be linearized according to (2.20) with the help of (2.22) and (2.23). Finally, (2.19) can be integrated by splitting the integrals at R_{stall} according to (2.26), which leads to the following expressions:

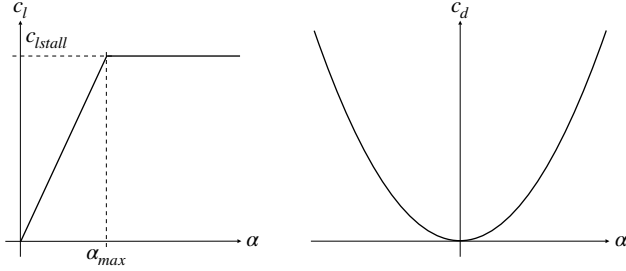


Figure 2.4: Blade section aerodynamic coefficients

$$\mathbf{F}_H^V = \rho \begin{bmatrix} C_{TFx}(J_1) \omega_P^2 R_P^4 \\ (C_{TFyV}(J_1) V'_H \cos \psi_V + C_{TFyQ}(J_1) R_P Q_H \cos \psi_Q) \omega_P' R_P^3 \\ (C_{TFyV}(J_1) V'_H \sin \psi_V + C_{TFyQ}(J_1) R_P Q_H \sin \psi_Q) \omega_P' R_P^3 \end{bmatrix} \quad (2.27a)$$

$$\mathbf{M}_H^V = \rho \begin{bmatrix} C_{TMx}(J_1) \omega_P^2 R_P^5 \\ (C_{TMyV}(J_1) V'_H \cos \psi_V + C_{TMyQ}(J_1) R_P Q_H \cos \psi_Q) \omega_P' R_P^4 \\ (C_{TMyV}(J_1) V'_H \sin \psi_V + C_{TMyQ}(J_1) R_P Q_H \sin \psi_Q) \omega_P' R_P^4 \end{bmatrix} \quad (2.27b)$$

The transformation into the vehicle coordinate system according to (2.13) has already been included here. The thrust coefficients only depend on the advance ratio and are obtained as follows:

$$C_{TFx}(J_1) = N(f_{x1}(J_1) c_{l\alpha} \alpha_{max} + f_{x2}(J_1) c_{l\alpha} + f_{x3}(J_1) c_{d\alpha}) \quad (2.28a)$$

$$C_{TFyV}(J_1) = N(f_{y1}(J_1) c_{l\alpha} \alpha_{max} + f_{y2}(J_1) c_{l\alpha} + f_{y3}(J_1) c_{d\alpha}) \quad (2.28b)$$

$$C_{TFyQ}(J_1) = N(f_{y4}(J_1) c_{l\alpha} \alpha_{max} + f_{y5}(J_1) c_{l\alpha} + f_{y6}(J_1) c_{d\alpha}) \quad (2.28c)$$

$$C_{TMx}(J_1) = N(m_{x1}(J_1) c_{l\alpha} \alpha_{max} + m_{x2}(J_1) c_{l\alpha} + m_{x3}(J_1) c_{d\alpha}) \quad (2.28d)$$

$$C_{TMyV}(J_1) = N(m_{y1}(J_1) c_{l\alpha} \alpha_{max} + m_{y2}(J_1) c_{l\alpha} + m_{y3}(J_1) c_{d\alpha}) \quad (2.28e)$$

$$C_{TMyQ}(J_1) = N(m_{y4}(J_1) c_{l\alpha} \alpha_{max} + m_{y5}(J_1) c_{l\alpha} + m_{y6}(J_1) c_{d\alpha}) \quad (2.28f)$$

The coefficients f_{x*} , f_{y*} , m_{x*} , and m_{y*} contain integrals, that have to be evaluated numerically for different advance ratios. This leaves the three unknown aerodynamic parameters $c_{l\alpha}$, α_{max} , and $c_{d\alpha}$, which have to be obtained from experimental tests. Both the numerical integration and the parameter identification are summarized in appendix B.

The equations derived in this chapter are valid under the following conditions:

$$\omega_P \geq 0$$

$$U'_H \geq 0$$

2.1.3 Electric Drive System

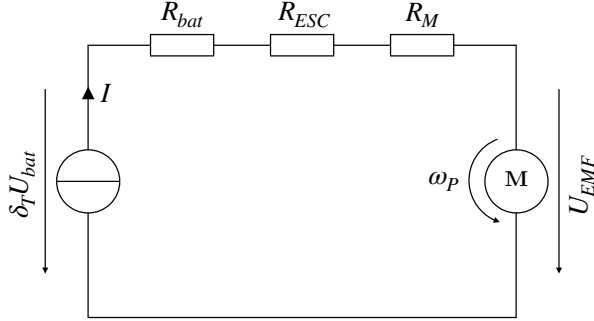


Figure 2.5: Circuit diagram of the powertrain

The electric powertrain consists of a lithium polymer battery, an electronic speed controller and a brushless DC motor (Figure 2.5). By applying Kirchhoff's law and an angular momentum balance, the following two equations can be derived:

$$\begin{aligned}\delta_T U_{bat} &= (R_{bat} + R_{ESC} + R_M)I + \frac{\omega_P}{k_V} \\ k_T(I - I_0) + L_T &= I_P \dot{\omega}_P\end{aligned}$$

They contain the motor constants k_V and k_T , the propeller moment of inertia I_P , the motor current I_0 due to friction, and the throttle command δ_T . By substituting them into another, the motor's differential equation can be formulated as:

$$\dot{\omega}_P = \frac{L_T + k_T}{I_P} \left(\frac{\delta_T U_{bat} - \frac{\omega_P}{k_V}}{R_{bat} + R_{ESC} + R_M} - I_0 \right) \quad (2.29)$$

The parameters of (2.29) can be found in appendix B.

2.2 Aerodynamic Forces and Moments

The aerodynamic forces and moments are derived in three steps:

1. Computing the aerodynamic section coefficients numerically with CFD.
2. Integrating the section coefficients for each lifting surface into wing coefficients.
3. Adding all three lifting surfaces' coefficients together, to form the vehicle's six aerodynamic coefficients.

In the following calculations, the aerodynamic state is usually described in terms of airspeed V_T , angle of attack α , and sideslip angle β . These quantities are related to the relative air velocity vector in vehicle coordinates by the following expressions [2, pp.78]:

$$\mathbf{v}_{rel}^V = \begin{bmatrix} U' \\ V' \\ W' \end{bmatrix} = \begin{bmatrix} V_T \cos \alpha \cos \beta \\ V_T \sin \beta \\ V_T \sin \alpha \cos \beta \end{bmatrix} \quad (2.30)$$

$$V_T = \sqrt{U'^2 + V'^2 + W'^2} \quad (2.31a)$$

$$\tan \alpha = \frac{W'}{U'} \quad (2.31b)$$

$$\sin \beta = \frac{V'}{V_T} \quad (2.31c)$$

2.2.1 Section Coefficients

The section coefficients are obtained from transient CFD computations with *ANSYS CFX* (Figure 2.6). The resulting lift, drag and moment plots can be found in appendix C. The effects of trailing edge flaps on the aerodynamic coefficients are added in the form of an empirical model³, which shall be described here.

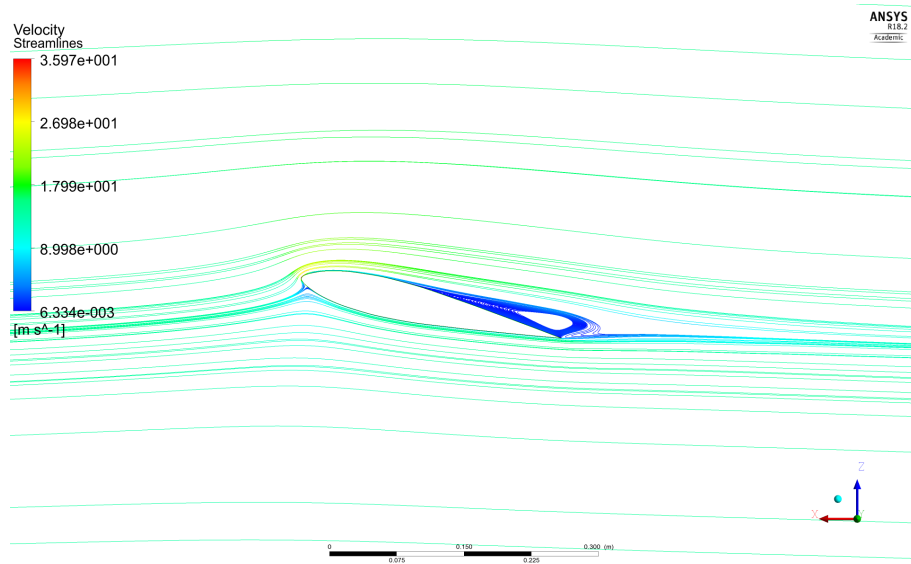


Figure 2.6: CFD simulation of the main wing's airfoil at 13 degrees angle of attack

³ Flight simulations proved the model to be sufficiently accurate

When a control surface is deflected, two effects on the section lift curve can be observed: a vertical and a horizontal shift, both depending on the amount of deflection δ [3, pp.169]. The maximum increase in lift for a plain flap is [7, pp.189]:

$$\max |c_{l\delta}\delta| = 0.8$$

If the flap is deflected above that point, maximum lift will start to decrease due to airflow separation. This relationship can be approximated by the following formula:

$$c_l(\alpha, \delta) = c_l(\alpha + \alpha_\delta\delta) + c_{l\delta}\delta$$

Here $c_{l\delta}(\delta)$ is the flap lift effectiveness and $\alpha_\delta(\delta)$ the flap angle of attack effectiveness. Both can be found by forcing the condition

$$c_l(\alpha, \delta) = c_{l\alpha}\alpha + \bar{c}_{l\delta}\delta$$

and inspecting figure 2.7:

$$c_{l\delta}(\delta) = \bar{c}_{l\delta} - \frac{\bar{c}_{l\delta}^2}{3.2} |\delta| \quad (2.32a)$$

$$\alpha_\delta(\delta) = \frac{\bar{c}_{l\delta}^2}{3.2c_{l\alpha}} |\delta| \quad (2.32b)$$

The flap lift effectiveness at zero deflection $\bar{c}_{l\delta}$ depends on the geometry of the flap and can be found in appendix C. By using (2.30), the section coefficients with trailing edge flap deflection can be found as:

$$c_l(\alpha, \delta) = c_l(\alpha + \alpha_\delta(\delta)\delta) + c_{l\delta}(\delta)\delta \quad (2.33a)$$

$$c_d(\alpha, \delta) = c_d(\alpha + \alpha_\delta(\delta)\delta) \quad (2.33b)$$

$$c_{m025}(\alpha, \delta) = c_{m025}(\alpha + \alpha_\delta(\delta)\delta) + c_{m\delta}\delta \quad (2.33c)$$

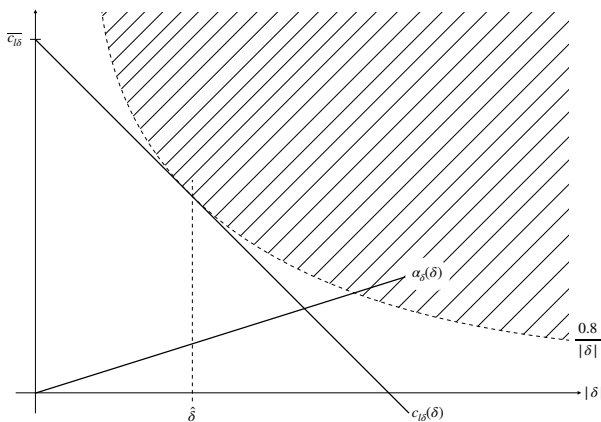


Figure 2.7: Trailing edge flap lift effectiveness

Here c_l , c_d , and c_{m025} are the section lift, drag, and moment coefficients in dependence of the angle of attack, obtained from the CFD simulations. The flap moment effectiveness $c_{m\delta}$ [3, pp.170] can also be found in appendix C.

2.2.2 Wing coefficients

A thorough description of the aerodynamic effects on a three-dimensional wing can be found in [2] and [3]. The following will outline an approach to derive the wing's aerodynamic coefficients, while only including important effects experienced with a small scale high-power propeller plane.

A three-dimensional wing (Figure 2.8) can produce two forces (lift L , drag D) and three moments (pitching moment M , rolling moment L_A , yawing moment N), which are defined by utilizing the wing's aerodynamic coefficients (C_L , C_D , C_{LA} , C_M , C_N):

$$L = q_\infty S C_L \quad (2.34a)$$

$$D = q_\infty S C_D \quad (2.34b)$$

$$L_A = q_\infty S b C_{LA} \quad (2.34c)$$

$$M = q_\infty S \bar{c} C_M \quad (2.34d)$$

$$N = q_\infty S b C_N \quad (2.34e)$$

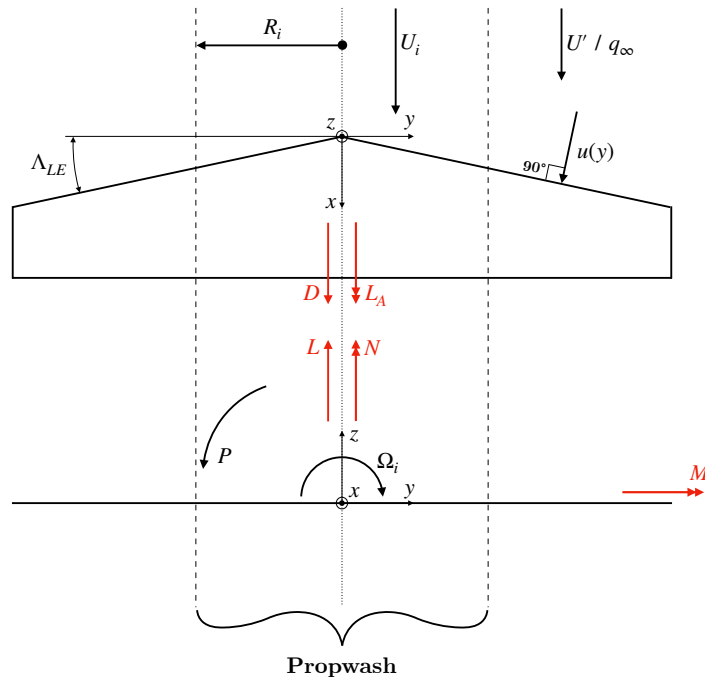


Figure 2.8: Aerodynamic forces and moments (red) on a wing

Here S is the wing area, b the wingspan, and \bar{c} the mean aerodynamic chord, whose values can be found in appendix C, along with other geometric properties. The free stream dynamic pressure q_∞ is defined with the free stream relative air velocity V_T :

$$q_\infty = \frac{1}{2} \rho V_T^2 \quad (2.35)$$

The forces and moments from (2.34) can be obtained by integrating the section coefficients (2.33) over the wingspan:

$$L = \int_{-b/2}^{b/2} \frac{1}{2} \rho u^2(y) k c_l(\alpha(y), \delta(y)) c(y) dy \quad (2.36a)$$

$$D = \int_{-b/2}^{b/2} \frac{1}{2} \rho u^2(y) c_d(\alpha(y), \delta(y)) c(y) dy + q_\infty S \frac{C_L^2}{\pi e A} \quad (2.36b)$$

$$M_{ac} = \int_{-b/2}^{b/2} \frac{1}{2} \rho u^2(y) c_{m025}(\alpha(y), \delta(y)) c^2(y) dy \quad (2.36c)$$

$$+ \int_{-b/2}^{b/2} \frac{1}{2} \rho u^2(y) k c_l(\alpha(y), \delta(y)) c(y) (X_{ac} - x_{ac}(y)) dy$$

$$L_A = \int_{-b/2}^{b/2} \frac{1}{2} \rho u^2(y) k c_l(\alpha(y), \delta(y)) c(y) y dy \quad (2.36d)$$

$$N = - \int_{-b/2}^{b/2} \frac{1}{2} \rho u^2(y) c_d(\alpha(y), \delta(y)) c(y) y dy \quad (2.36e)$$

Both the lift correction factor k and the Oswald efficiency number e come from the losses due to induced drag and are derived in appendix C. To evaluate the integrals, one has to know the local flow $\alpha(y)$ and $u(y)$ at each section, due to propwash and wing roll rate. Local sideslip $\beta(y)$ is neglected in this realization, since the effects on a moderately swept wing are small. By using (2.31) and inspecting figure 2.8, following relations can be found:

$$u(y) = \begin{cases} V_T c_{pw}(y) \cos(\Lambda_{LE} + \beta) & \text{for } y < 0 \\ V_T c_{pw}(y) \cos(\Lambda_{LE} - \beta) & \text{for } y \geq 0 \end{cases} \quad (2.37)$$

$$\alpha(y) = \begin{cases} \arctan \left(\left(\tan(\alpha) + \frac{P}{U'} y - \frac{\Omega_i}{U'} y \right) \frac{U'}{U_i} \right) & \text{for } |y| < R_i \\ \arctan \left(\tan(\alpha) + \frac{P}{U'} y \right) & \text{for } |y| \geq R_i \end{cases} \quad (2.38)$$

(2.37) contains the propwash correction factor c_{pw} , which is defined as the relative air velocity increase in the fully developed slipstream behind the propeller:

$$c_{pw}(y) = \begin{cases} 1 & \text{for } |y| < R_i \\ \sqrt{\left(\frac{U_i}{U'}\right)^2 \cos^2 \alpha \cos^2 \beta + \sin^2 \beta + \sin^2 \alpha \cos^2 \beta} & \text{for } |y| \geq R_i \end{cases} \quad (2.39)$$

By inserting above expressions into (2.36) and comparing the result with (2.34), the aerodynamic coefficients of a lifting surface can be found as:

$$C_L = \frac{k}{S} \left(\cos^2(\Lambda_{LE} + \beta) \int_{-b/2}^0 c_{pw}^2 c_l(\alpha(y), \delta(y)) c dy + \cos^2(\Lambda_{LE} - \beta) \int_0^{b/2} c_{pw}^2 c_l(\alpha(y), \delta(y)) c dy \right) \quad (2.40a)$$

$$C_D = \frac{1}{S} \left(\cos^2(\Lambda_{LE} + \beta) \int_{-b/2}^0 c_{pw}^2 c_d(\alpha(y), \delta(y)) c dy + \cos^2(\Lambda_{LE} - \beta) \int_0^{b/2} c_{pw}^2 c_d(\alpha(y), \delta(y)) c dy \right) + \frac{C_L^2}{\pi e A} \quad (2.40b)$$

$$C_{Mac} = \frac{1}{S\bar{c}} \left(\cos^2(\Lambda_{LE} + \beta) \int_{-b/2}^0 c_{pw}^2 c_{m025}(\alpha(y), \delta(y)) c^2 + k c_l(\alpha(y), \delta(y)) c (X_{ac} - x_{ac}) \right) dy + \cos^2(\Lambda_{LE} - \beta) \int_0^{b/2} c_{pw}^2 c_{m025}(\alpha(y), \delta(y)) c^2 + k c_l(\alpha(y), \delta(y)) c (X_{ac} - x_{ac}) \right) dy \quad (2.40c)$$

$$C_{LA} = \frac{k}{Sb} \left(\cos^2(\Lambda_{LE} + \beta) \int_{-b/2}^0 c_{pw}^2 c_l(\alpha(y), \delta(y)) c y dy + \cos^2(\Lambda_{LE} - \beta) \int_0^{b/2} c_{pw}^2 c_l(\alpha(y), \delta(y)) c y dy \right) \quad (2.40d)$$

$$C_N = -\frac{1}{Sb} \left(\cos^2(\Lambda_{LE} + \beta) \int_{-b/2}^0 c_{pw}^2 c_d(\alpha(y), \delta(y)) c y dy + \cos^2(\Lambda_{LE} - \beta) \int_0^{b/2} c_{pw}^2 c_d(\alpha(y), \delta(y)) c y dy \right) \quad (2.40e)$$

2.2.3 Vehicle coefficients

The vehicle's three aerodynamic forces and moments are connected to the vehicle's six aerodynamic coefficients by the following relations [2, pp.79]:

$$L = q_\infty S_W C_L \quad (2.41a)$$

$$D = q_\infty S_W C_D \quad (2.41b)$$

$$S = q_\infty S_W C_S \quad (2.41c)$$

$$L_A = q_\infty S_W b_W C_{LA} \quad (2.41d)$$

$$M = q_\infty S_W \bar{c}_W C_M \quad (2.41e)$$

$$N = q_\infty S_W b_W C_N \quad (2.41f)$$

They are defined at an arbitrary reference point with the location (Figure 2.9):

$$\mathbf{x}_{ref} = [-0.32m \ 0.0m \ 0.0m]^T$$

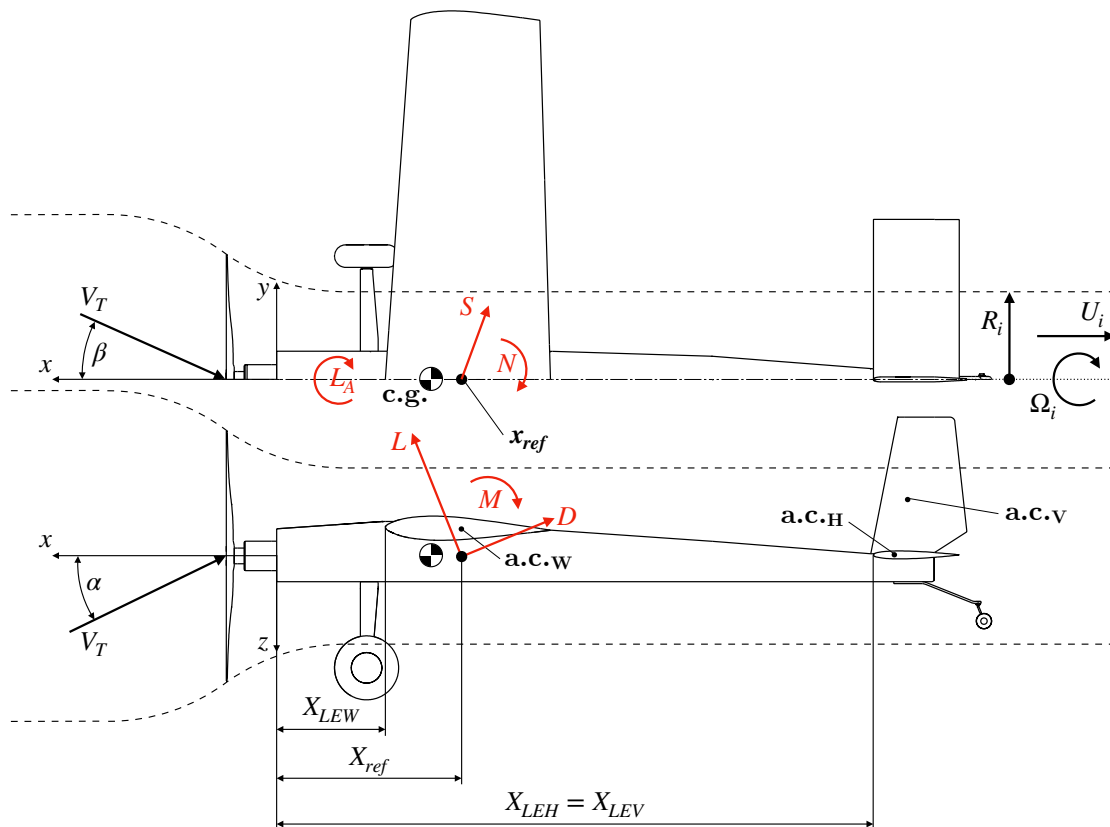


Figure 2.9: Aerodynamic forces and moments on the vehicle

It has to be noted, that the aerodynamic forces (2.41a-c) are given in wind axes, while the aerodynamic moments (2.41d-f) are given in vehicle axes.

To distinguish the aerodynamic and geometric parameters of the different lifting surfaces, the following indices are introduced:

- W for the main wing
- H for the horizontal stabilizer
- V for the vertical stabilizer

Each wing's aerodynamic center has a different aerodynamic state due to the rotational velocity of the plane and the main wing's downwash. At any point on the vehicle, the relative air velocity can be computed as follows:

$$\mathbf{v}_{rel}(\mathbf{x}) = \mathbf{v}_{rel} + \boldsymbol{\omega}_V \times (\mathbf{x} - \mathbf{x}_{ref}) \quad (2.42)$$

By inspecting figure 2.9, and by using the relations from (2.31) and (2.42), the local flow at the lifting surfaces' aerodynamic centers can be obtained as:

$$\alpha_W = \alpha + i_W \quad (2.43a)$$

$$\beta_W = \beta \quad (2.43b)$$

$$\alpha_H = \arctan\left(\tan \alpha - \frac{Q}{U'}(X_{ACH} - X_{ref})\right) + i_H - \frac{d\varepsilon}{d\alpha}\alpha_W \quad (2.44a)$$

$$\beta_H = \arcsin\left(\sin \beta + \frac{R}{U'} \cos \alpha \cos \beta (X_{ACH} - X_{ref})\right) \quad (2.44b)$$

$$\alpha_V = \arctan\left(\frac{\tan \beta}{\cos \alpha} + \frac{R}{U'}(X_{ACV} - X_{ref})\right) \quad (2.45a)$$

$$\beta_V = \arcsin\left(\tan \alpha - \frac{Q}{U'}(X_{ACV} - X_{ref}) \cos \alpha \cos \beta\right) \quad (2.45b)$$

(2.44a) introduces the downwash gradient $d\varepsilon/d\alpha$ at the horizontal tail due to the main wing [3, pp.214-216]. Its value can be found in appendix C. The aerodynamic coefficients can now be obtained by adding the forces and moments of the main wing, horizontal tail, and vertical tail (2.40), as well as the parasitic drag force (see appendix C.4) together and comparing with (2.41):

$$C_L = C_{LW} + \frac{S_H}{S_W} C_{LH} \quad (2.46a)$$

$$C_D = C_{DW} + \frac{S_H}{S_W} C_{DH} + \frac{S_V}{S_W} C_{DV} + C_{DF} \quad (2.46b)$$

$$C_C = -\frac{S_V}{S_W} C_{LV} \quad (2.46c)$$

$$C_{LA} = -C_{LAW} \cos \alpha_W + C_{NW} \sin \alpha_W - \frac{S_H b_H}{S_W b_W} C_{LAH} \cos \alpha_H - \frac{S_V b_V}{S_W b_W} C_{LAV} \cos \alpha_V \quad (2.46d)$$

$$C_M = C_{MW} + \frac{S_H \bar{c}_H}{S_W \bar{c}_W} C_{MH} + \frac{S_H}{S_W \bar{c}_W} C_{LH} \cos \alpha_H (X_{ACH} - X_{ref}) \quad (2.46e)$$

$$C_N = -C_{NW} \cos \alpha_W - \frac{S_V}{S_W b_W} C_{LV} \cos \alpha_V (X_{ACV} - X_{ref}) \quad (2.46f)$$

These dimensionless coefficients are dependent on 12 parameters, being:

- free stream angle of attack α
- free stream sideslip angle β
- vehicle angular rates $P/Q/R$
- control surface deflections $\delta_{A/E/R/F}$
- propwash $U_i/\Omega_i/R_i$

Since the evaluation of (2.40) has to be done numerically, which is computationally expensive in a real-time flight simulation, a lookup table is created. Not all of the above mentioned parameters have a big influence on all of the aerodynamic coefficients. After some considerations, the following dependencies can be found:

$$\left. \begin{array}{l} C_L \left(\alpha, \beta, \frac{Q}{U'} \frac{\Omega_i}{U'}, \frac{U_i}{U'}, \delta_F \right) \\ C_D \left(\alpha, \beta, \frac{\Omega_i}{U'}, \frac{U_i}{U'}, \delta_F \right) \\ C_S \left(\alpha, \beta, \frac{R}{U'}, \frac{\Omega_i}{U'}, \frac{U_i}{U'}, \delta_R \right) \end{array} \right\} \text{in wind axes} \quad (2.47a)$$

$$\left. \begin{array}{l} C_{LA} \left(\alpha, \beta, \frac{P}{U'} \frac{\Omega_i}{U'}, \frac{U_i}{U'}, \delta_A, \delta_R \right) \\ C_M \left(\alpha, \beta, \frac{Q}{U'}, \frac{\Omega_i}{U'}, \frac{U_i}{U'}, \delta_E, \delta_F \right) \\ C_N \left(\alpha, \beta, \frac{R}{U'}, \frac{\Omega_i}{U'}, \frac{U_i}{U'}, \delta_A, \delta_R \right) \end{array} \right\} \text{in vehicle axes} \quad (2.47a)$$

To reduce the size of the obtained dataset further, the input parameters are limited to the following range:

Parameter	Lower range	Upper range	Parameter	Lower range	Upper range
α	$-\pi/2$	$\pi/2$	Ω_i/U'	0m^{-1}	1.5m^{-1}
β	$-\pi/2$	$\pi/2$	δ_A	-25deg	25deg
P/U'	$-2\pi/15\text{m}^{-1}$	$2\pi/15\text{m}^{-1}$	δ_E	-25deg	25deg
Q/U'	$-2\pi/15\text{m}^{-1}$	$2\pi/15\text{m}^{-1}$	δ_R	-40deg	40deg
R/U'	$-2\pi/15\text{m}^{-1}$	$2\pi/15\text{m}^{-1}$	δ_F	0deg	30deg
U_i/U'	0.2	2.0			

Finally, the moment coefficients in vehicle axes are linked to the moment coefficients in wind axes by the following transformation:

$$q_\infty S_W \begin{bmatrix} b_W C_{LA} \\ \bar{c}_W C_M \\ b_W C_N \end{bmatrix}^W = q_\infty S_W T_{WV} \begin{bmatrix} b_W C_{LA} \\ \bar{c}_W C_M \\ b_W C_N \end{bmatrix}^V$$

$$\begin{bmatrix} C_{LA} \\ C_M \\ C_N \end{bmatrix}^W = \begin{bmatrix} 1/b_W & 0 & 0 \\ 0 & 1/\bar{c}_W & 0 \\ 0 & 0 & 1/b_W \end{bmatrix} T_{WV} \begin{bmatrix} b_W & 0 & 0 \\ 0 & \bar{c}_W & 0 \\ 0 & 0 & b_W \end{bmatrix} \begin{bmatrix} C_{LA} \\ C_M \\ C_N \end{bmatrix}^V \quad (2.48)$$

Here T_{WV} is the transformation matrix from vehicle to wind axes.

Appendix C.5 includes plots of some of the computed aerodynamic coefficients at different aerodynamic states. The effect of the propwash on the lift coefficient is especially pronounced (Figure C.7). Figure C.8 shows that the plane has static longitudinal stability up to 20 degrees angle of attack. The pitching moment change from flaps extension is also seen. The intense roll and yaw tendency due to the propwash can be seen in figure C.9 and C.10. Although the case of maximum propwash is only encountered when the plane is applying full throttle at airspeeds well below the stall speed (at the beginning of the takeoff run for example), the impact during normal flight conditions is still strongly noticeable.

2.3 Assembling the Model

The propulsion model (Figure 2.10) and the aerodynamic model (Figure 2.11) are combined with a kinematical model in *Simulink* to form the nonlinear simulation framework (Figure 2.12). Propeller acceleration and gyroscopic moments are also included (Figure 2.12). Both propulsion and aerodynamic data are pre-computed and stored in lookup tables. The simulation is running at 500Hz with an *ode4* (Runge-Kutta) solver. Most of the validation and controller testing was done by manually piloting the plane in *Simulink* in a real-time adapted simulation. Control inputs come from the same radio control, as it is used for the real flight tests, via a joystick interface⁴. Visualization is done with the open-source flight simulator *FlightGear*. The complete model furthermore includes the implemented controllers, as well as a wind and turbulence model according to Military Specification MIL-F-8785C. It can be seen in appendix E.

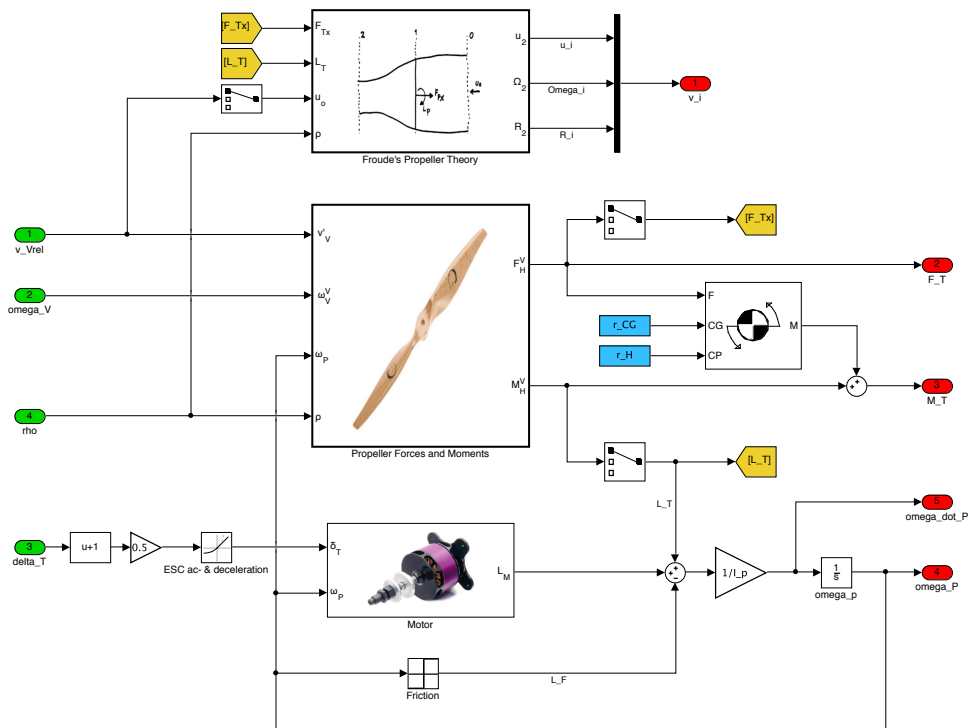


Figure 2.10: Propulsion model in *Simulink*, containing propeller energy and momentum balance, propeller forces and moments, motor dynamics, and shifting of hub forces to centre of gravity

⁴ *Simulink* joystick interface block from Zebb Prime, The University of Adelaide

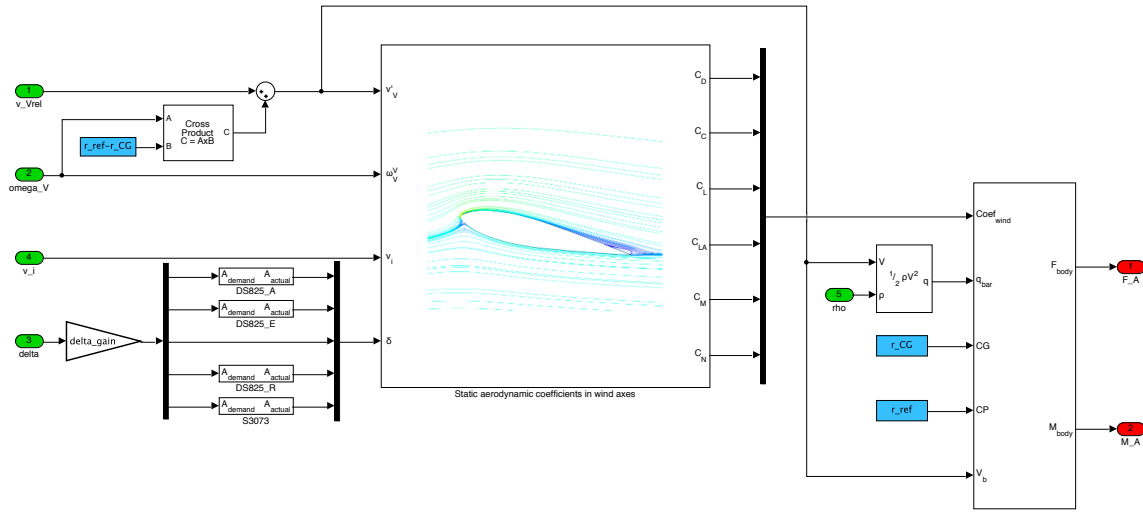


Figure 2.11: Aerodynamic model in *Simulink*, containing actuator dynamics, airflow at reference point, aerodynamic coefficients, and shifting of forces from reference point to centre of gravity

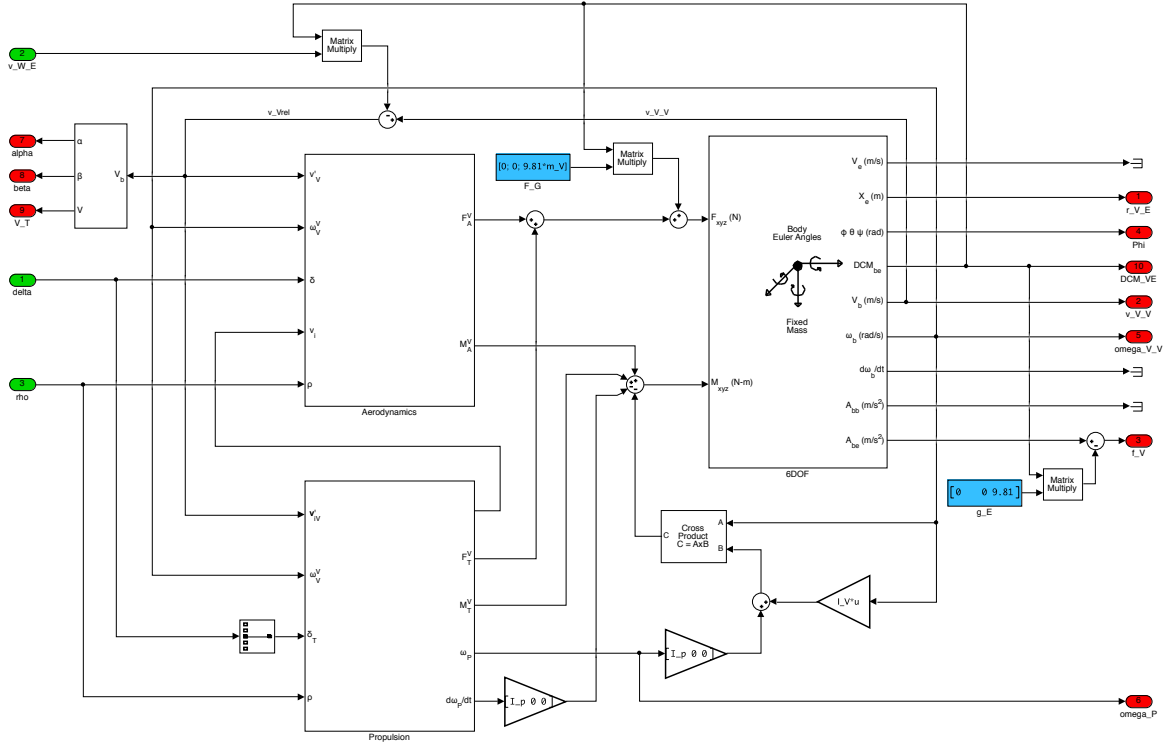


Figure 2.12: Combined *Simulink* model of the propulsion, aerodynamic and kinematical model (*Aerospace Blockset*)

Chapter 3

Flight Hardware

3.1 Airframe

The airplane has been custom built for the requirements of this work (Figure 3.1). It has a wingspan of 1.5m, an aspect ratio of 5.04, an overall length of 1.4m and a dry mass of 4.5kg. Fully loaded with batteries, the flight computer, and sensors, it weighs 6.5kg.

Its electric motor delivers 2.5kW of power and produces 20lbf of thrust with a 20in propeller, running from a 10 cell 4Ah lithium-polymer battery pack. Special high speed servos are utilized, to maximize performance of the implemented controllers. The fuselage is mainly made out of poplar and birch plywood with some glass fibre reinforcements. The wing is balsa sheeted with a foam core and glass fibre reinforcements. A technical drawing of the plane is found in appendix F.



Figure 3.1: ARM-Hawk airframe

3.2 Flight Computer

The flight software runs on an STM32F767ZI 32-bit micro controller. All code is custom written in C++. Tasks of the Flight Computer are:

- System monitoring and fail safe handling
- Data logging
- Flight controls:
 - Reading pilot input
 - Sending servo commands
 - Motor speed measurement and powertrain state estimation
- Air data measurements
- Inertial navigation:
 - Gyroscope, accelerometer, and magnetometer data acquisition and calibration
 - Processing GPS readings
 - Inertial state estimation
- Lateral stability augmentation
- Stall protection

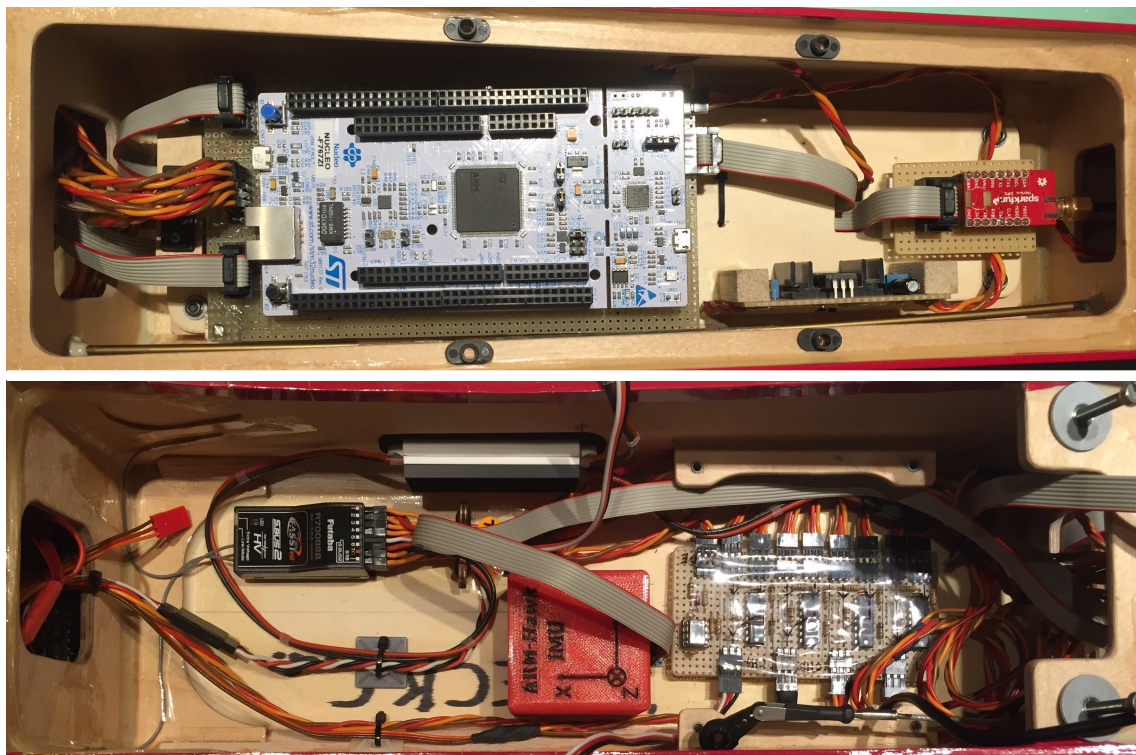


Figure 3.2a (top): Rear equipment area: Flight Computer, power supply, and GPS

Figure 3.2a (bottom): Front equipment area: RC equipment, IMU, and Servo multiplexer

With the exception of the Inertial Navigation System (Chapter 3.4), all of the above tasks are done at a pace of 50Hz. The flight controls (servos) are connected to a self-made servo switch, which allows the pilot to disconnect the Flight Computer from the flight controls in case of failure. The electrical schematic can be found in appendix F. The hardware setup can be seen in figure 3.2.

3.3 Air Data Sensor Unit

The Air Data Sensor Unit measures the vehicle's state relative to the surrounding air. This includes the airspeed, angle of attack, sideslip angle, static pressure (for altitude calculation), and static air temperature. Since mechanical alpha and beta vanes [1, pp.372] are not easily implemented at this scale, an alternative approach has been taken by developing a 5-hole spherical pressure probe, as it is commonly used in wind tunnel measurements [4, pp.159-162], [5, pp.384]. The probe is custom designed and fabricated to meet the project's demands (Figures 3.3 and 3.4). A technical drawing can be found in appendix F. To reduce development time, the calibration in a wind tunnel has been replaced by CFD simulations. The following describes the derivation of the 5-hole probe's characteristics, as well as the numerical calibration of the static pressure port with the help of *ANSYS CFX*.

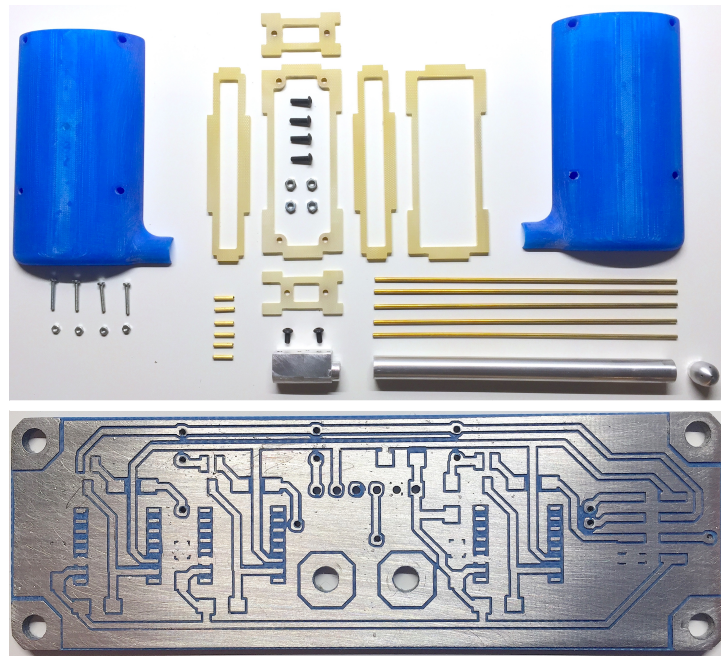


Figure 3.3a (top): Parts layout of the mechanical Air Data Sensor Unit assembly

Figure 3.3b (bottom): Interface PCB hosts three differential and one absolute pressure sensor



Figure 3.4: Air Data Sensor Unit with 5-hole probe head

Figure 3.5 shows the location of the five holes at the probe's tip. The pressure at the ports zero to four is a function of the flow angle θ_i , and the freestream's static and dynamic pressure p_∞ and q_∞ . The relation can be described in form of a dimensionless pressure coefficient c_p as follows:

$$c_p(\theta_i) = \frac{p(\theta_i) - p_\infty}{q_\infty} \quad (3.1)$$

The flow angle θ_i at each pressure port can be obtained from the dot product of the port's position vector \mathbf{x}_{iP}^V with the airspeed vector \mathbf{v}_{rel}^V (2.30):

$$\cos \theta_i = \frac{\mathbf{x}_{iP}^V \cdot \mathbf{v}_{rel}^V}{|\mathbf{x}_{iP}^V| |\mathbf{v}_{rel}^V|} \quad (3.2)$$

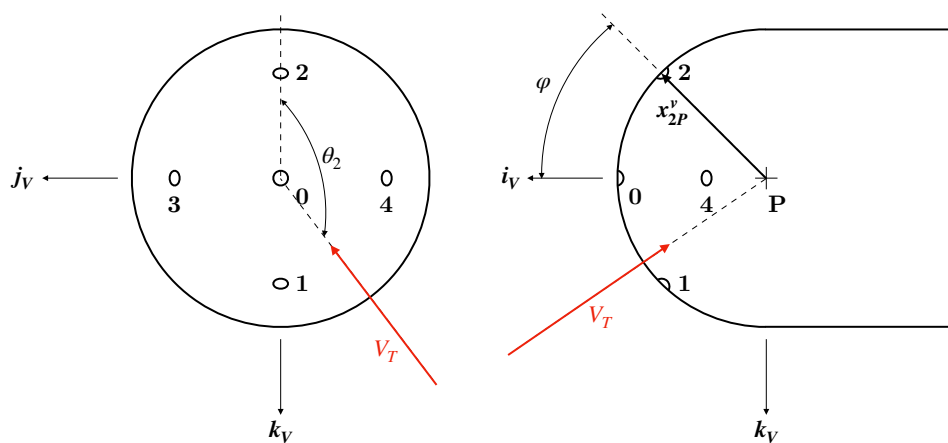


Figure 3.5: Location of pressure ports on the 5-hole probe's tip

Inspecting figure 3.5 and using (3.2) leads to:

$$\cos \theta_0 = \cos \alpha \cos \beta \quad (3.3a)$$

$$\cos \theta_1 = \cos \varphi \cos \alpha \cos \beta + \sin \varphi \sin \alpha \cos \beta \quad (3.3b)$$

$$\cos \theta_2 = \cos \varphi \cos \alpha \cos \beta - \sin \varphi \sin \alpha \cos \beta \quad (3.3c)$$

$$\cos \theta_3 = \cos \varphi \cos \alpha \cos \beta + \sin \varphi \sin \alpha \sin \beta \quad (3.3d)$$

$$\cos \theta_4 = \cos \varphi \cos \alpha \cos \beta - \sin \varphi \sin \alpha \sin \beta \quad (3.3e)$$

The sensor unit contains three differential pressure sensors, connected to the six pressure ports⁵ the following way:

$$\Delta p_{12} = p_1 - p_2 = (c_p(\theta_1) - c_p(\theta_2))q_\infty \quad (3.4a)$$

$$\Delta p_{34} = p_3 - p_4 = (c_p(\theta_3) - c_p(\theta_4))q_\infty \quad (3.4b)$$

$$\Delta p_{0S} = p_0 - p_\infty = c_p(\theta_0)q_\infty \quad (3.4c)$$

A CFD simulation in *ANSYS CFX* (Figure 3.6) finally gives a correlation for the pressure coefficient c_p . The computed probe has a diameter of 12mm and the pressure ports are offset by $\varphi = 45$ degrees from the probe's axis. The obtained data for c_p is interpolated with the following ansatz:

$$c_p(\theta_i) = a_1 \sin(2\theta_i) + a_2 \cos(2\theta_i) + a_3 \quad (3.5)$$

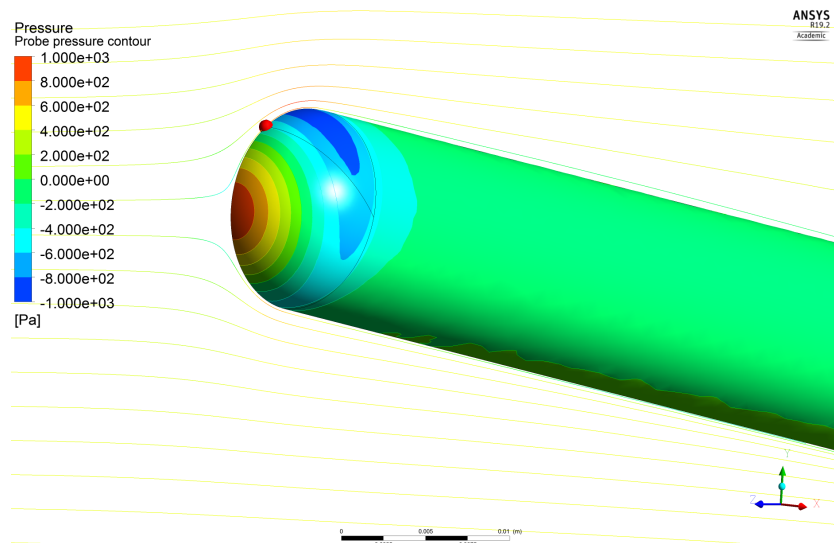


Figure 3.6: ANSYS CFX simulation of the pressure distribution at the 5-hole probe's tip at 10 degrees angle of attack and 40m/s airspeed (red point = pressure port)

⁵ Five at the tip and one free stream static air pressure port at the circumference of the probe's tube

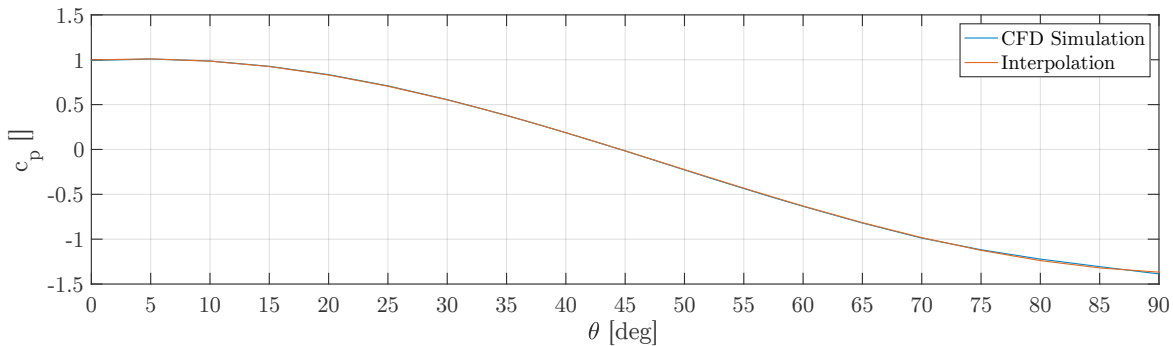


Figure 3.7 (bottom): Pressure coefficient from CFD simulation and from fitted ansatz

Performing a regression analysis and combining the two trigonometric terms leads to the following expression:

$$c_p(\theta_i) = 2.4 \cos^2 \theta_i - 1.4 \quad (3.6)$$

Figure 3.7 shows, that the numerically obtained data fits the chosen ansatz very well. Substituting (3.3) and (3.5) into (3.4) leads to the characteristics of the probe (Figure 3.8). But since the flight computer needs to obtain the free stream velocity vector from the pressure readings, equations (3.3), (3.4), and (3.6) have to be inverted. After some rearranging, the following relations are obtained:

$$\Delta p_{12} - 4.8 \sin \alpha \cos \alpha \cos^2 \beta q_\infty = 0 \quad (3.7a)$$

$$\Delta p_{34} - 4.8 \cos \alpha \sin \beta \cos \beta q_\infty = 0 \quad (3.7b)$$

$$\Delta p_{0S} - 2.4 \cos^2 \alpha \cos^2 \beta q_\infty + 1.4 q_\infty = 0 \quad (3.7c)$$

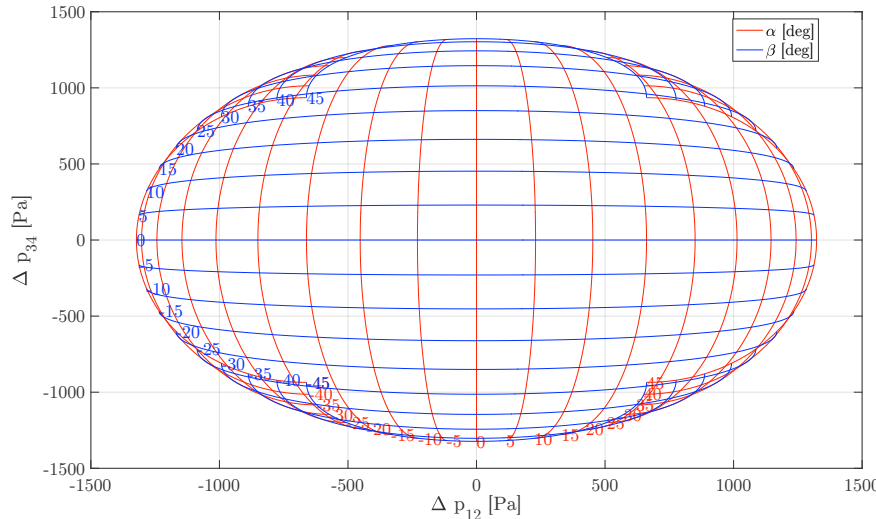


Figure 3.8: Characteristics of the 5-hole probe at 30m/s airspeed

These are solved numerically by using Newton's method [8, pp.977]:

$$\frac{\partial \mathbf{F}}{\partial \mathbf{x}}(\mathbf{x}_n)\boldsymbol{\delta}_n = -\mathbf{F}(\mathbf{x}_n) \quad (3.8a)$$

$$\begin{aligned} \mathbf{x}_{n+1} &= \mathbf{x}_n + w\boldsymbol{\delta}_n \\ \mathbf{x} &= [\alpha \ \beta \ q_\infty]^T \end{aligned} \quad (3.8b)$$

The nonlinear function matrix \mathbf{F} is equal to (3.7) and it's Jacobian can be found as:

$$\frac{\partial \mathbf{F}}{\partial \mathbf{x}} = \begin{bmatrix} 4.8 \cos^2 \beta (\sin^2 \alpha - \cos^2 \alpha) q_\infty & 9.6 \sin \alpha \cos \alpha \sin \beta \cos \beta q_\infty & -4.8 \sin \alpha \cos \alpha \cos^2 \beta \\ 4.8 \sin \alpha \sin \beta \cos \beta q_\infty & 4.8 \cos \alpha (\sin^2 \beta - \cos^2 \beta) q_\infty & -4.8 \cos \alpha \sin \beta \cos \beta \\ 4.8 \sin \alpha \cos \alpha \cos^2 \beta q_\infty & 4.8 \cos^2 \alpha \sin \beta \cos \beta q_\infty & -2.4 \cos^2 \alpha \cos^2 \beta + 1.4 \end{bmatrix}$$

By setting $\cos \alpha = 1$ and $\cos \beta = 1$, one obtains the following initial estimate for the algorithm:

$$q_0 = \max(\Delta p_{0S}, |\Delta p_{12}|, |\Delta p_{34}|) \quad (3.9a)$$

$$\mathbf{x}_0 = \begin{bmatrix} q_0 \\ \arcsin\left(\frac{\Delta p_{12}}{4.8q_0}\right) \\ \arcsin\left(\frac{\Delta p_{34}}{4.8q_0}\right) \end{bmatrix} \quad (3.9b)$$

The algorithm converges quickly when using a relaxation factor of $w = 0.5$ in (3.8b), but equation (3.8a) still involves solving one linear system per iteration, which is computationally costly. Therefore a precomputed lookup table of the variables V_T , α , and β in dependence of the three differential pressures Δp_{0S} , Δp_{12} , and Δp_{34} is stored in the Flight Computer's flash memory.

The static pressure port for altitude calculation is positioned on a curved surface at the side of the Air Data Sensor Unit's housing (see also the technical drawing in appendix F). The static pressure measurement therefore also needs to be compensated. Figure 3.9a shows a CFD analysis of the housing's cross-section. The corrected static pressure p_∞ is obtained from the measured static pressure p_{stat} :

$$p_\infty = p_{stat} + \Delta p_{stat} \quad (3.10)$$

The correction pressure Δp_{stat} can be obtained by performing a quadratic interpolation on the data from the CFD simulation in dependence of the relative air velocity component U' (Figure 3.9b):

$$0.579U'^2 - 0.819U' \quad (3.11)$$

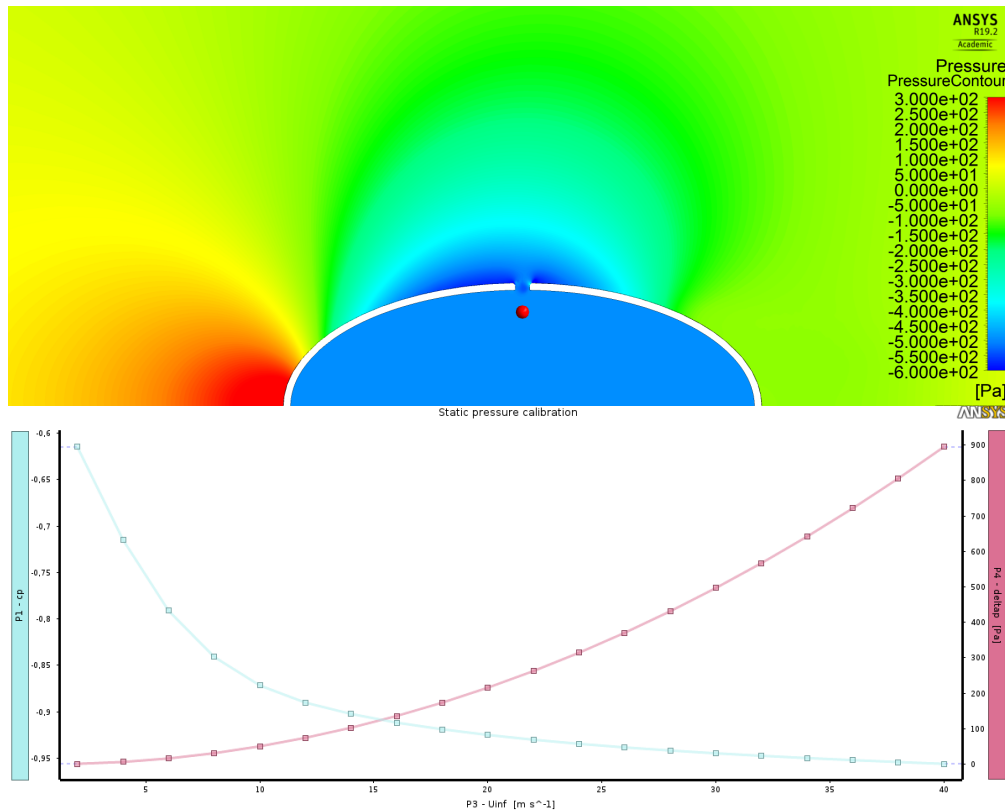


Figure 3.9a (top): ANSYS CFX simulation of the pressure at the static port at 30m/s airspeed
(red point = absolute pressure sensor port)

Figure 3.9b (bottom): Static port pressure calibration $p_{stat}(V_T)$ obtained from CFD simulation

3.4 Inertial Navigation System

The Inertial Navigation System (INS) provides following vehicle states:

- Ground speed v_V^V
- Inertial position r_V^E
- Orientation (both Euler angles Φ and quaternion q)

This is done by measuring the following quantities:

- Specific force f^V (IMU)
- Angular velocity ω_V^V (IMU)
- Magnetic flux density B_E^V (IMU)
- Horizontal position X_E and Y_E (GPS)
- Barometric altitude $Z_E = -h$ from the Air Data Sensor Unit

The position vector is constructed as follows:

$$\mathbf{r}_V^E = [X_E \ Y_E \ Z_E]^T$$

The estimation of the unknown states is done by two Kalman filters (one rotational and one translational one), which use the vehicle's kinematic model (Figure 3.10). The model utilizes the quaternion representation of the vehicle's attitude to avoid the threat of gimbal lock [2, pp.50-51]. Quaternion algebra can be reviewed in [2, pp.45-54], [8, pp.298-314], and [9, pp.420-421]. The following notation will be used in this work:

$$\mathbf{q} = [q_0 \ \mathbf{q}]^T = [q_0 \ q_1 \ q_2 \ q_3]^T \quad (3.12)$$

The rotation matrix from the vehicle coordinate system to the earth coordinate system T_{VE} is given in [2, pp.53] as:

$$T_{VE} = \begin{bmatrix} (q_0^2 + q_1^2 - q_2^2 - q_3^2) & 2(q_1q_2 + q_0q_3) & 2(q_1q_3 - q_0q_2) \\ 2(q_1q_2 - q_0q_3) & (q_0^2 - q_1^2 + q_2^2 - q_3^2) & 2(q_2q_3 + q_0q_1) \\ 2(q_1q_3 + q_0q_2) & 2(q_2q_3 - q_0q_1) & (q_0^2 - q_1^2 - q_2^2 + q_3^2) \end{bmatrix} \quad (3.13)$$

$$T_{EV} = T_{VE}^T$$

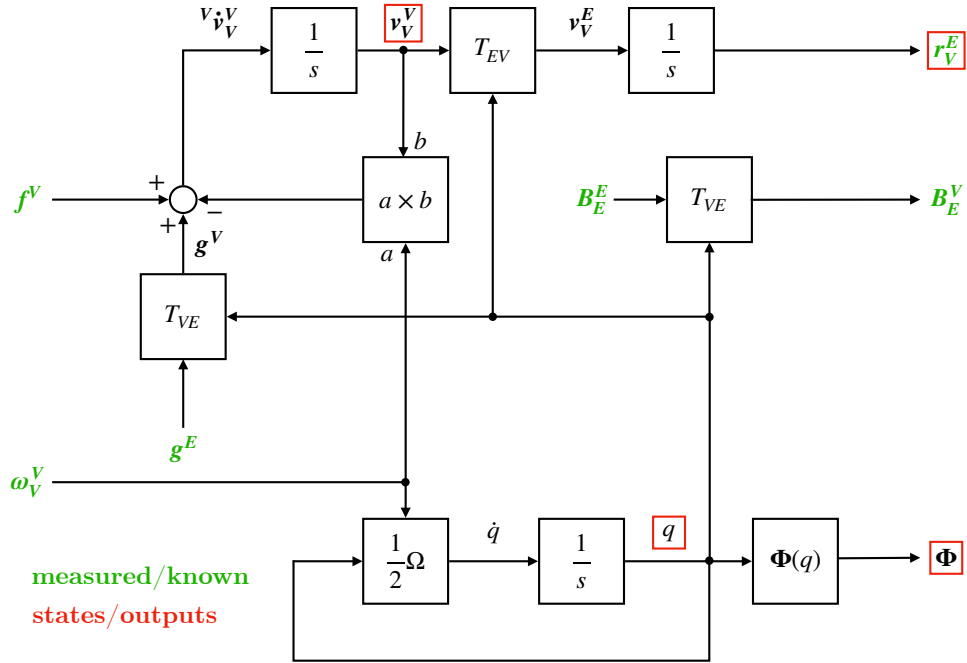


Figure 3.10: Kinematic model of the INS

3.4.1 Inertial Measurement Unit

The Inertial Measurement Unit (IMU) consists of a NXP FXOS8700C combined accelerometer and magnetometer, and a NXP FXAS21002C angular rate gyroscope, both on a BRKT-STBC-AGM01 breakout board. The board is soldered onto a custom interface PCB and protected in an enclosure (Figure 3.11). The housing also provides a solid reference frame for calibration and installation in the plane.

The accelerometer measures the specific force [2, pp.33], which is obtained from the vehicle's acceleration ${}^V\dot{v}_V^V$ and the earth's gravity \mathbf{g}^V vector:

$$\mathbf{f}^V = {}^V\dot{v}_V^V - \mathbf{g}^V \quad (3.14)$$

It is calibrated according to the following scheme⁶:

$$\mathbf{f}^V = C(\mathbf{f}_{acc} - \mathbf{f}_0) \quad (3.15)$$

\mathbf{f}_{acc} ...measured specific force

\mathbf{f}_0 ...specific force bias vector

C ... calibration matrix

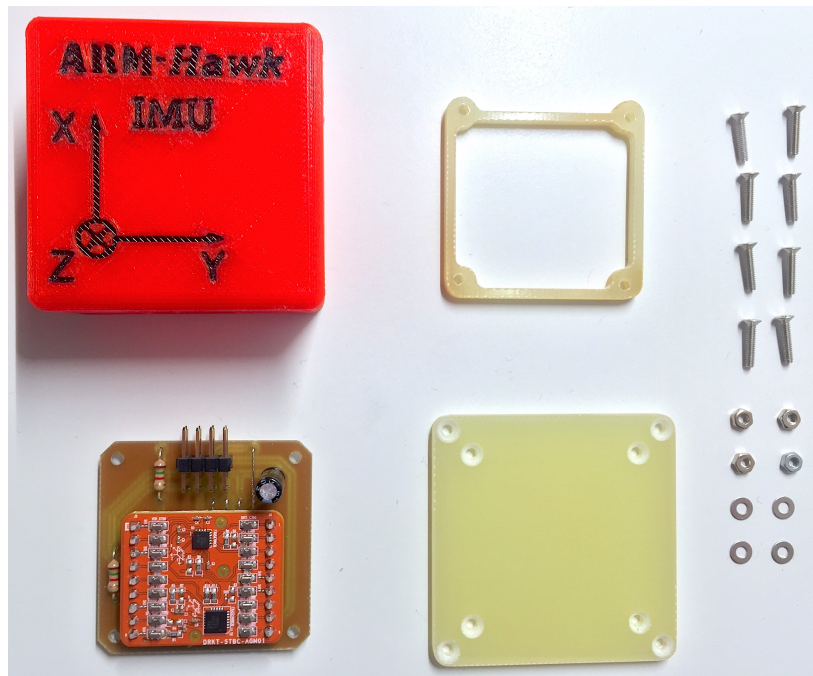


Figure 3.11: IMU on interface PCB with mounting plates and enclosure

⁶ Accelerometer calibration is based on the recommendations from NXP application note AN4399

The calibration parameters are obtained by a 18 point static calibration with a least squares fit [8, pp.973-974]. The reference value for \mathbf{f}^V in the static case is the negative local gravity vector, which is obtained from the *International Gravimetric Bureau*⁷. Since the IMU is not located exactly at the vehicle's centre of gravity, equation (3.14) yields the measured specific force \mathbf{f}_{IMU}^V instead of the desired C.G. specific force \mathbf{f}_{CG}^V . By using some kinematic relations, \mathbf{f}_{CG}^V can be obtained as:

$$\mathbf{f}_{CG}^V = \mathbf{f}_{IMU}^V + \boldsymbol{\omega}_V^V \times (\boldsymbol{\omega}_V^V \times (\mathbf{r}_{CG|REF}^V - \mathbf{r}_{IMU|REF}^V)) \quad (3.16)$$

Angular acceleration terms ${}^V\dot{\boldsymbol{\omega}}_V^V$ have been neglected in the above equation, since they are not readily available from measurements.

The magnetometer calibration scheme includes an additional calibration factor, to compensate for magnetic fields coming from the direct currents I in the powertrain's wires⁸:

$$\mathbf{B}_E^V = C(\mathbf{B}_M^V - \mathbf{B}_0^V - I\mathbf{B}_I^V) \quad (3.17)$$

\mathbf{B}_E^V ...earth's magnetic flux density vector

\mathbf{B}_M^V ...measured magnetic flux density vector

\mathbf{B}_0^V ...magnetic flux density hard iron offset vector

\mathbf{B}_I^V ...motor current dependent hard iron offset vector

C ...calibration matrix

The calibration matrix of the magnetometer can be split the following way:

$$C = (S \cdot M)^{-1} \quad (3.18)$$

S ...soft-iron scale matrix

M ...soft-iron misalignment matrix

The soft-iron scale matrix compensates any distortions of the magnetic field due to ferromagnetic materials in the vicinity of the sensor. This distortion causes the measured vector to lie on an ellipsoid surface instead of a sphere, if the sensor is rotated. The ellipsoid can be described with the symmetric coefficient matrix A :

$$(\mathbf{B}_M^V - \mathbf{B}_0^V)^T A (\mathbf{B}_M^V - \mathbf{B}_0^V) = (M\mathbf{B}_E^V)^T S^T A \ S(M\mathbf{B}_E^V) = 1$$

⁷ <http://bgi.obs-mip.fr/data-products/Toolbox/Prediction-of-gravity-value>

⁸ Magnetometer calibration is based on the recommendations from NXP application note AN4246

Note that S contains no rotations and therefore is also symmetric. To ensure that the right side of above equation is always valid, the following condition must hold⁹:

$$S^T A S = \frac{1}{|\mathbf{B}_E^V|^2} I_{3 \times 3}$$

Several hundred data points are collected by rotating the airplane with all equipment installed, as it would be in flight. The coefficient matrix A can then be obtained by performing an ellipsoidal fit with the measured data. The scale matrix finally follows as:

$$S = \frac{1}{|\mathbf{B}_E^V|} A^{-1/2} \quad (3.19)$$

The hard iron offset vector \mathbf{B}_0^V can be found by repeating the above calculation until an optimal solution is found.

The misalignment matrix M compensates any unwanted rotation of the sensor. To obtain it, reference measurements with the plane leveled and pointing in each of the four cardinal directions are taken. These measurements are then used to minimize the error of the desired rotation matrix, as described in [8, pp.312-313]:

$$P = M^T D$$

Here D is a diagonal matrix and P is obtained from the reference measurements \mathbf{a}_i :

$$\begin{aligned} P &= \sum_i^{n,e,s,w} \mathbf{a}_i \mathbf{b}_i \\ \mathbf{a}_i &= [\mathbf{B}_{En}^V, \mathbf{B}_{Ee}^V, \mathbf{B}_{Es}^V, \mathbf{B}_{Ew}^V] \\ \mathbf{b}_i &= S^{-1}([\mathbf{B}_{Mn}^V, \mathbf{B}_{Me}^V, \mathbf{B}_{Ms}^V, \mathbf{B}_{Mw}^V] - \mathbf{B}_o^V) \end{aligned}$$

The earth's local magnetic field vector \mathbf{b}_i is obtained from the *National Oceanic and Atmospheric Administration*¹⁰. By choosing the diagonal matrix as

$$D^2 = P^T P,$$

the problem can be solved for M :

$$M = \left(P(P^T P)^{-1/2} \right)^T \quad (3.20)$$

⁹ The coefficient matrix for the quadratic form of a sphere is a diagonal matrix with equal elements

¹⁰ <https://www.ngdc.noaa.gov/geomag-web/#igrfwmm>

The motor current is compensated by performing some static runs on the ground and taking an average for \mathbf{B}_I^V , computed from (3.17) with (3.18), (3.19), and (3.20). Figure 3.12 shows the result of the magnetometer calibration.

The angular rate gyroscope is calibrated with the following equation:

$$\omega_V^V = C(\omega_{gyro}^V - \omega_0^V) - Gf^V \quad (3.21)$$

ω_{gyro}^V ...measured angular rate
 ω_0^V ...angular rate bias vector
 C ...calibration matrix
 G ...g-force coupling matrix

For simplicity reasons, G is limited to a diagonal matrix. The calibration parameters are obtained by rotating the sensor 180 degrees around 24 different axes and performing a least squares fit on the collected data. This procedure slightly changes equation (3.21) to the following:

$$\int_0^T \omega_V^V dt = C \left(\int_0^T \omega_{gyro}^V dt - \omega_0^V T \right) - Gf^V T \quad (3.22)$$

$$\left| \int_0^T \omega_V^V dt \right| = \pi$$

Note that the accelerometer has to be calibrated prior to calibrating the gyroscope, due to the need of f^V in (3.21).

Performing the calibrations mentioned in this chapter has led to the following improvements in precision:

Sensor	Error before calibration	Error after calibration
Accelerometer	2.04 %	0.59%
Magnetometer	0.45%	0.16%
Gyroscope	3.27%	1.09%

The obtained calibration parameters are summarized in appendix D.

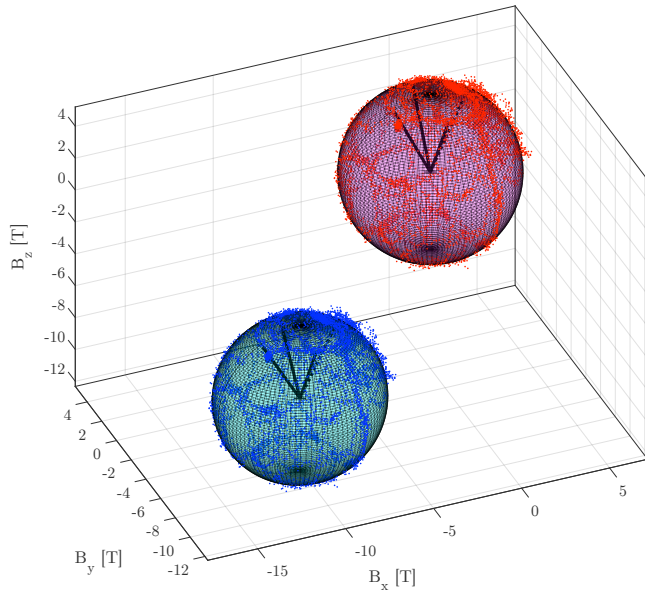


Figure 3.12: Uncalibrated (blue) and calibrated (red) magnetometer output

3.4.2 Measuring the Vehicle's Attitude

The rotational Kalman filter needs the vehicle's orientation for updating its state estimate. Since the orientation cannot be obtained directly from a single sensor, it has to be reconstructed from multiple sensors. In the given approach, the attitude is calculated by measuring the two constant physical quantities \mathbf{g} (gravity vector) and \mathbf{B}_E (earth's magnetic field vector)¹¹ to compute the transformation matrix T_{VE} (Figure 3.13). The magnetic field vector \mathbf{B}_E^V is already available from the compensated magnetometer readings, but the gravity vector \mathbf{g}^V differs from the accelerometer's measured specific force \mathbf{f}^V when the vehicle is under acceleration (3.14). This can be described by the following kinematic relation:

$$\mathbf{g}^V = {}^V\dot{\mathbf{v}}_V^V + \boldsymbol{\omega}_V^V \times \mathbf{v}_V^V - \mathbf{f}^V \quad (3.23)$$

Since both $\boldsymbol{\omega}_V^V$ and \mathbf{v}_V^V are known, as long as the Kalman filters estimate correctly, the gravity vector \mathbf{g}^V can be estimated by setting ${}^V\dot{\mathbf{v}}_V^V = 0$, which is adequate for most phases of flight. To average out measurement errors, an orthogonal basis is formed from the gravity vector \mathbf{g} and the magnetic field vector \mathbf{B}_E in the following way:

¹¹ Note that their values depend on the geographical location, see also chapter 3.4.1

$$\mathbf{e}_1 = \frac{\frac{\mathbf{g}^E}{|\mathbf{g}^E|} + \frac{\mathbf{B}_E^E}{|\mathbf{B}_E^E|}}{\left| \frac{\mathbf{g}^E}{|\mathbf{g}^E|} + \frac{\mathbf{B}_E^E}{|\mathbf{B}_E^E|} \right|} \quad \mathbf{v}_1 = \frac{\frac{\mathbf{g}^V}{|\mathbf{g}^V|} + \frac{\mathbf{B}_E^V}{|\mathbf{B}_E^V|}}{\left| \frac{\mathbf{g}^V}{|\mathbf{g}^V|} + \frac{\mathbf{B}_E^V}{|\mathbf{B}_E^V|} \right|} \quad (3.24a)$$

$$\mathbf{e}_2 = \frac{\mathbf{g}^E \times \mathbf{B}_E^E}{\left| \mathbf{g}^E \times \mathbf{B}_E^E \right|} \quad \mathbf{v}_2 = \frac{\mathbf{g}^V \times \mathbf{B}_E^V}{\left| \mathbf{g}^V \times \mathbf{B}_E^V \right|} \quad (3.24b)$$

$$\mathbf{e}_3 = \mathbf{e}_1 \times \mathbf{e}_2 \quad \mathbf{v}_3 = \mathbf{v}_1 \times \mathbf{v}_2 \quad (3.24c)$$

$$\mathbf{E} = [\mathbf{e}_1 \ \mathbf{e}_2 \ \mathbf{e}_3] \quad \mathbf{V} = [\mathbf{v}_1 \ \mathbf{v}_2 \ \mathbf{v}_3] \quad (3.24d)$$

$$\mathbf{T}_{VE} = \mathbf{V}\mathbf{E}^T \quad (3.24e)$$

The Euler angles can then be obtained from [2, pp.12]:

$$\phi = \arctan\left(\frac{T_{VE}(2,3)}{T_{VE}(3,3)}\right) \quad (3.25a)$$

$$\theta = \arcsin\left(-T_{VE}(1,3)\right) \quad (3.25b)$$

$$\psi = \arctan\left(\frac{T_{VE}(1,2)}{T_{VE}(1,1)}\right) \quad (3.25c)$$

Since the gravity vector \mathbf{g}^E is always aligned vertically along the \mathbf{k}_E axis, it does not provide any yaw information, which results in a poor heading guess from (3.24) and (3.25). Therefore, an alternative approach is used to compute the heading, which only uses the horizontal components of the magnetic field vector \mathbf{B}_E^E .

Firstly, the transformation matrix T_{VE} is split according to [2, pp.12] into two parts:

$$T_{VE} = \begin{bmatrix} \cos \theta & 0 & -\sin \theta \\ \sin \phi \sin \theta & \cos \theta & \sin \phi \cos \theta \\ \cos \phi \sin \theta & -\sin \theta & \cos \phi \cos \theta \end{bmatrix} \begin{bmatrix} \cos \psi & \sin \psi & 0 \\ -\sin \psi & \cos \psi & 0 \\ 0 & 0 & 1 \end{bmatrix}$$

$$T_{VE} = T_1 \ T_2$$

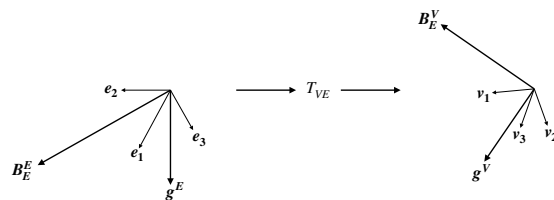


Figure 3.13: Coordinate rotation from earth to vehicle base

The horizontal components of the measured magnetic field vector can then be calculated as:

$$\begin{aligned}\mathbf{B}_E^V &= T_{VE} \mathbf{B}_E^E \\ T_1 \mathbf{B}_E^V &= T_2 \mathbf{B}_E^E = \mathbf{B}'_E\end{aligned}$$

Since the magnetic north direction does not equal the true north direction due to the magnetic declination, the desired heading is found as:

$$\begin{aligned}\psi &= \psi_E - \psi' \\ \psi &= \arctan\left(\frac{B_{Ey}^E}{B_{Ex}^E}\right) - \arctan\left(\frac{B'_{Ey}}{B'_{Ex}}\right)\end{aligned}\quad (3.27)$$

This can be seen by inspecting figure 3.14.

The calculation of the vehicle's attitude relies on the assumption made in (3.23), that the vehicle is not accelerating. If that is the case, the computations are wrong. To avoid problems with the rotational Kalman filter, the heading value from the Euler angles is complementary filtered as follows:

$$\Phi = [\phi \quad \theta \quad \hat{\psi} + a_g(\psi - \hat{\psi})]^T \quad (3.28a)$$

$$a_g = 1 - a_0 \left| \frac{|\mathbf{g}^V|}{|\mathbf{g}^E|} - 1 \right| \quad (3.28b)$$

$$0 \leq a_g \leq 1; \quad a_0 = 10$$

Here $\hat{\psi}$ is the estimated heading from the Kalman filter and a_g the acceleration gain, which indicates how certain the computed vehicle orientation is. The value a_0 has been experimentally determined from simulations.

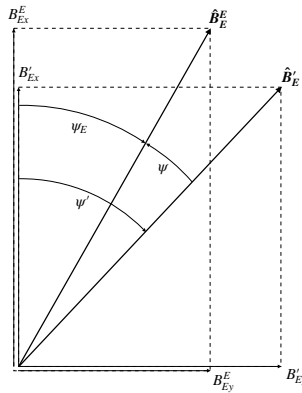


Figure 3.14: Horizontal magnetic field components

3.4.3 State Estimation with Kalman Filter

The INS uses two discrete-time extended Kalman filters, one for rotational and one for translational kinematics, to estimate the vehicle's current state. The Kalman filter estimates the state vector \mathbf{x} for nonlinear systems of the following form:

$$\begin{aligned}\dot{\mathbf{x}} &= \mathbf{f}(\mathbf{x}, \mathbf{u}, \mathbf{w}) \\ \mathbf{y} &= \mathbf{h}(\mathbf{x}, \mathbf{u}, \mathbf{v})\end{aligned}$$

Here \mathbf{u} and \mathbf{y} are the system's inputs and outputs, and \mathbf{w} and \mathbf{v} are the process and measurement noises respectively. Estimated variables are denoted by a hat (for example $\hat{\mathbf{x}}$). Prediction step results are distinguished from the update step by a right superscript (for example $\hat{\mathbf{x}}^{(-)}$ for predicted and $\hat{\mathbf{x}}^{(+)}$ for updated state estimate). Since the filter is used in its discrete form, a right subscript is used to link a variable to a time-step.

The prediction step equations can be summarized as follows:

$$\hat{\mathbf{x}}_k^{(-)} = F_k \hat{\mathbf{x}}_{k-1}^{(+)} + \mathbf{u}_k \quad (3.29a)$$

$$P_k^{(-)} = F_k P_{k-1}^{(+)} F_k^T + L_k Q L_k^T \quad (3.29b)$$

The state covariance matrix P and the process covariance matrix Q are introduced here, as well as the Jacobians F_k and L_k :

$$F_k = \left. \frac{\partial \mathbf{f}}{\partial \mathbf{x}} \right|_{\hat{\mathbf{x}}_k} \quad (3.30a)$$

$$L_k = \left. \frac{\partial \mathbf{f}}{\partial \mathbf{w}} \right|_{\hat{\mathbf{x}}_k} \quad (3.30b)$$

Note that the INS performs the prediction step at a higher pace than the update step. The update step, though, always samples at 50Hz and can be described as follows:

$$K_k = P_k^{(-)} H_k^T (H_k P_k^{(-)} H_k^T + M_k R M_k^T)^{-1} \quad (3.31a)$$

$$\hat{\mathbf{x}}_k^{(+)} = \hat{\mathbf{x}}_k^{(-)} + K_k (\mathbf{y}_k - H_k \hat{\mathbf{x}}_k^{(-)}) \quad (3.31b)$$

$$P_k^{(+)} = (I_{n \times n} - K_k H_k) P_k^{(-)} \quad (3.31c)$$

The Kalman gain matrix K and the measurement covariance matrix R are introduced here, as well as the Jacobians H_k and M_k :

$$H_k = \frac{\partial \mathbf{h}}{\partial \mathbf{x}} \Big|_{\hat{\mathbf{x}}_k} \quad (3.32a)$$

$$M_k = \frac{\partial \mathbf{h}}{\partial \mathbf{v}} \Big|_{\hat{\mathbf{x}}_k} \quad (3.32b)$$

The translational Kalman filter uses six states:

$$\mathbf{x} = [U \ V \ W \ X_E \ Y_E \ Z_E]^T$$

Its output vector is written as:

$$\mathbf{y} = [X_E \ Y_E \ Z_E]^T$$

The translational kinematic model can be obtained by inspecting figure 3.10. It eventually leads to the following Jacobians:

$$F_k = \begin{bmatrix} 1 & T_s R & -T_s Q & 0 & 0 & 0 \\ -T_s R & 1 & T_s P & 0 & 0 & 0 \\ T_s Q & -T_s P & 1 & 0 & 0 & 0 \\ T_s(q_0^2 + q_1^2 - q_2^2 - q_3^2) & 2T_s(q_1q_2 - q_0q_3) & 2T_s(q_1q_3 + q_0q_2) & 1 & 0 & 0 \\ 2T_s(q_1q_2 + q_0q_3) & T_s(q_0^2 - q_1^2 + q_2^2 - q_3^2) & 2T_s(q_2q_3 - q_0q_1) & 0 & 1 & 0 \\ 2T_s(q_1q_3 - q_0q_2) & 2T_s(q_2q_3 + q_0q_1) & T_s(q_0^2 - q_1^2 - q_2^2 + q_3^2) & 0 & 0 & 1 \end{bmatrix} \quad (3.33a)$$

$$L_k = \begin{bmatrix} T_s & 0 & 0 \\ 0 & T_s & 0 \\ 0 & 0 & T_s \\ 0 & 0 & 0 \\ 0 & 0 & 0 \\ 0 & 0 & 0 \end{bmatrix} \quad (3.33b)$$

$$H_k = \begin{bmatrix} 0 & 0 & 0 & 1 & 0 & 0 \\ 0 & 0 & 0 & 0 & 1 & 0 \\ 0 & 0 & 0 & 0 & 0 & 1 \end{bmatrix} \quad (3.33c)$$

$$M_k = I_{3 \times 3} \quad (3.33d)$$

$$T_s = \frac{1}{400}s$$

Additionally, the discretized input vector is needed:

$$\mathbf{u}_k = \begin{bmatrix} f_x + 2g(q_1q_3 - q_0q_2) \\ f_y + 2g(q_2q_3 + q_0q_1) \\ f_z + g(q_0^2 - q_1^2 - q_2^2 + q_3^2) \\ 0 \\ 0 \\ 0 \end{bmatrix} \quad (3.34)$$

Finally, the covariance matrices are obtained from simulations (see appendix D):

$$Q = \sigma_f^2; \quad R = \sigma_r^2$$

The translational Kalman filter's prediction step is performed at 400Hz.

The rotational Kalman filter is almost entirely designed according to the guidelines in [9]. Here the prediction is performed at 800Hz. State and output vector are given as:

$$\begin{aligned} x &= [q_0 \ q_1 \ q_2 \ q_3]^T \\ y &= [\delta q_1 \ \delta q_2 \ \delta q_3]^T \end{aligned}$$

Prediction and update steps differ slightly from those mentioned in (3.29) to (3.32), since the covariance matrix P needs to maintain singularity due to the quaternion representation [9, pp. 423]. From [2, pp.50-51], the following can be obtained for the first Jacobian:

$$F_k = \begin{bmatrix} 1 & -\frac{T_s}{2}P & -\frac{T_s}{2}Q & -\frac{T_s}{2}R \\ \frac{T_s}{2}P & 1 & \frac{T_s}{2}R & -\frac{T_s}{2}Q \\ \frac{T_s}{2}Q & -\frac{T_s}{2}R & 1 & \frac{T_s}{2}P \\ \frac{T_s}{2}R & \frac{T_s}{2}Q & -\frac{T_s}{2}P & 1 \end{bmatrix} \quad (3.35)$$

$$T_s = \frac{1}{800}s$$

The estimated state vector is of fourth order, but the covariance matrix' order is reduced to three [9, pp.425]. Therefore, (3.29b) is replaced by:

$$\tilde{P}_k^{(-)} = \tilde{F}_k \tilde{P}_{k-1}^{(+)} \tilde{F}_k^T + \tilde{L}_k Q \tilde{L}_k^T \quad (3.36a)$$

$$\tilde{F}_k = \begin{bmatrix} 1 & T_sR & -T_sQ \\ -T_sR & 1 & T_sP \\ T_sQ & -T_sP & 1 \end{bmatrix} \quad (3.36b)$$

$$\tilde{L}_k = -\frac{T_s}{2} I_{3 \times 3} \quad (3.36c)$$

The update step replaces (3.31) with:

$$q_k = h(\Phi_k) \quad (3.37a)$$

$$\delta q_k = J_k^T x_k \quad (3.37b)$$

$$\tilde{K}_k = \tilde{P}_k^{(-)} \tilde{H}_k^T (\tilde{H}_k \tilde{P}_k^{(-)} \tilde{H}_k^T + \tilde{M}_k R \tilde{M}_k^T)^{-1} \quad (3.37c)$$

$$\delta \hat{\mathbf{q}}_k = \tilde{K}_k \delta \mathbf{q}_k \quad (3.37d)$$

$$\tilde{P}_k^{(+)} = (I_{3 \times 3} - \tilde{K}_k \tilde{H}_k) \tilde{P}_k^{(-)} \quad (3.37e)$$

$$\hat{q}_k^{(+)} = \hat{q}_k^{(-)} + J \delta \hat{\mathbf{q}}_k \quad (3.37f)$$

The corresponding Jacobians are:

$$\tilde{H}_k = I_{3 \times 3} \quad (3.38a)$$

$$\tilde{M}_k = J_k^T G_k \quad (3.38b)$$

$$J_k^T = \begin{bmatrix} -\hat{q}_1 & \hat{q}_0 & \hat{q}_3 & -\hat{q}_2 \\ -\hat{q}_2 & -\hat{q}_3 & \hat{q}_0 & \hat{q}_1 \\ -\hat{q}_3 & \hat{q}_2 & -\hat{q}_1 & \hat{q}_0 \end{bmatrix} \quad (3.38c)$$

$$G_k = \frac{1}{2} \begin{bmatrix} -\hat{q}_1 & -\hat{r}_2 & -\hat{q}_3 \\ \hat{q}_0 & -\hat{r}_3 & -\hat{q}_2 \\ \hat{q}_3 & \hat{r}_0 & \hat{q}_1 \\ -\hat{q}_2 & -\hat{r}_1 & \hat{q}_0 \end{bmatrix} \quad (3.38d)$$

$$\hat{q}_0 = \cos \frac{\phi}{2} \cos \frac{\theta}{2} \cos \frac{\psi}{2} + \sin \frac{\phi}{2} \sin \frac{\theta}{2} \sin \frac{\psi}{2}$$

$$\hat{q}_1 = \sin \frac{\phi}{2} \cos \frac{\theta}{2} \cos \frac{\psi}{2} - \cos \frac{\phi}{2} \sin \frac{\theta}{2} \sin \frac{\psi}{2}$$

$$\hat{q}_2 = \cos \frac{\phi}{2} \sin \frac{\theta}{2} \cos \frac{\psi}{2} + \sin \frac{\phi}{2} \cos \frac{\theta}{2} \sin \frac{\psi}{2}$$

$$\hat{q}_3 = \cos \frac{\phi}{2} \cos \frac{\theta}{2} \sin \frac{\psi}{2} - \sin \frac{\phi}{2} \sin \frac{\theta}{2} \cos \frac{\psi}{2}$$

$$\hat{r}_0 = \cos \frac{\phi}{2} \cos \frac{\theta}{2} \cos \frac{\psi}{2} - \sin \frac{\phi}{2} \sin \frac{\theta}{2} \sin \frac{\psi}{2}$$

$$\hat{r}_1 = \sin \frac{\phi}{2} \cos \frac{\theta}{2} \cos \frac{\psi}{2} + \cos \frac{\phi}{2} \sin \frac{\theta}{2} \sin \frac{\psi}{2}$$

$$\hat{r}_2 = \cos \frac{\phi}{2} \sin \frac{\theta}{2} \cos \frac{\psi}{2} - \sin \frac{\phi}{2} \cos \frac{\theta}{2} \sin \frac{\psi}{2}$$

$$\hat{r}_3 = \cos \frac{\phi}{2} \cos \frac{\theta}{2} \sin \frac{\psi}{2} + \sin \frac{\phi}{2} \sin \frac{\theta}{2} \cos \frac{\psi}{2}$$

The output function of (3.37a) is obtained from [2, pp.52]:

$$\begin{bmatrix} q_0 \\ q_1 \\ q_2 \\ q_3 \end{bmatrix} = \begin{bmatrix} \cos \frac{\phi}{2} \cos \frac{\theta}{2} \cos \frac{\psi}{2} + \sin \frac{\phi}{2} \sin \frac{\theta}{2} \sin \frac{\psi}{2} \\ \sin \frac{\phi}{2} \cos \frac{\theta}{2} \cos \frac{\psi}{2} - \cos \frac{\phi}{2} \sin \frac{\theta}{2} \sin \frac{\psi}{2} \\ \cos \frac{\phi}{2} \sin \frac{\theta}{2} \cos \frac{\psi}{2} + \sin \frac{\phi}{2} \cos \frac{\theta}{2} \sin \frac{\psi}{2} \\ \cos \frac{\phi}{2} \cos \frac{\theta}{2} \sin \frac{\psi}{2} - \sin \frac{\phi}{2} \sin \frac{\theta}{2} \cos \frac{\psi}{2} \end{bmatrix} \quad (3.39)$$

It is mandatory to match the sign of q_0 and \hat{q}_0 after performing the above calculation, since the quaternion representation is not unique.

After every prediction and update step, the estimated rotation quaternion has to be normalized, to avoid build up of numerical errors:

$$\hat{q}_{k+1} = \frac{\hat{q}_k}{|\hat{q}_k|} \quad (3.40)$$

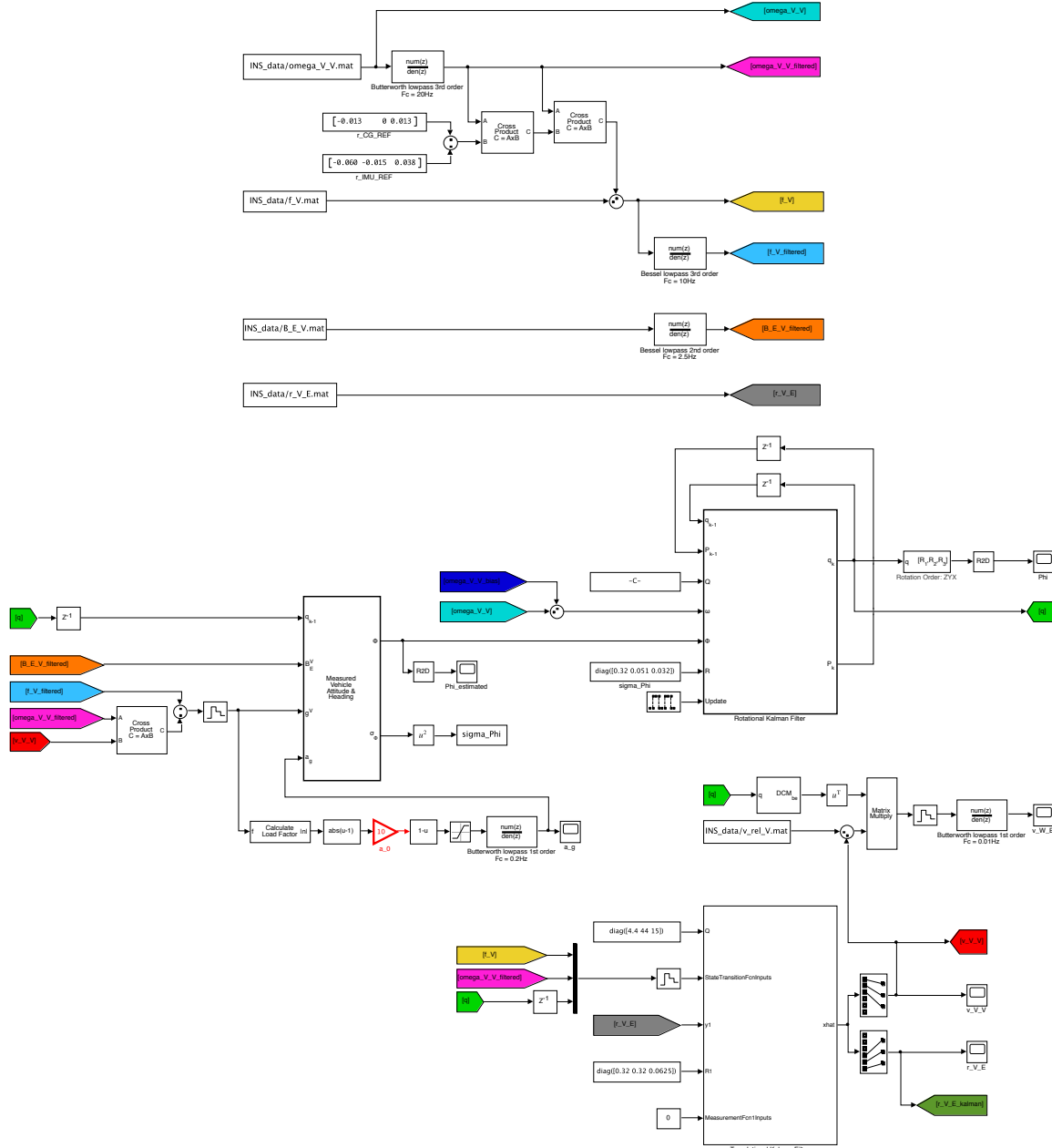


Figure 3.15: INS Simulink model including input data filtering, attitude measurement, vehicle state estimation, and wind speed estimation

Finally, the covariance matrices are obtained from simulations (see appendix D):

$$Q = \sigma_\omega^2; \quad R = \sigma_\Phi^2$$

A simulink model of the complete state estimation algorithm can be seen in figure 3.15.

3.5 RPM Sensor

The stall protection needs knowledge of the vehicle's full state vector, including the propeller's angular velocity. Therefore an RPM sensor had to be installed. The idea behind the sensor is to measure the period of the voltage between two motor phases, which can be related to the motor's RPM by the number of poles. Since the electric speed controller adjusts motor speed by pulse width modulation, the voltage signal has to be smoothed by a lowpass filter ($f_c = 3.4\text{kHz}$). The schematic of the circuit can be found in appendix F, the finished sensor is seen in figure 3.17. The magnetometer from the IMU needs the motor current for calibration purposes. To omit a separate current sensor, an estimation is done by using the measured motor speed and the current throttle input. Using the model derived for the electric powertrain (2.29) the estimated current is given by:

$$I_{est} = \frac{\delta_T U_{bat} - \frac{\omega_P}{kV}}{R_{bat} + R_{ESC} + R_M} \quad (3.41)$$

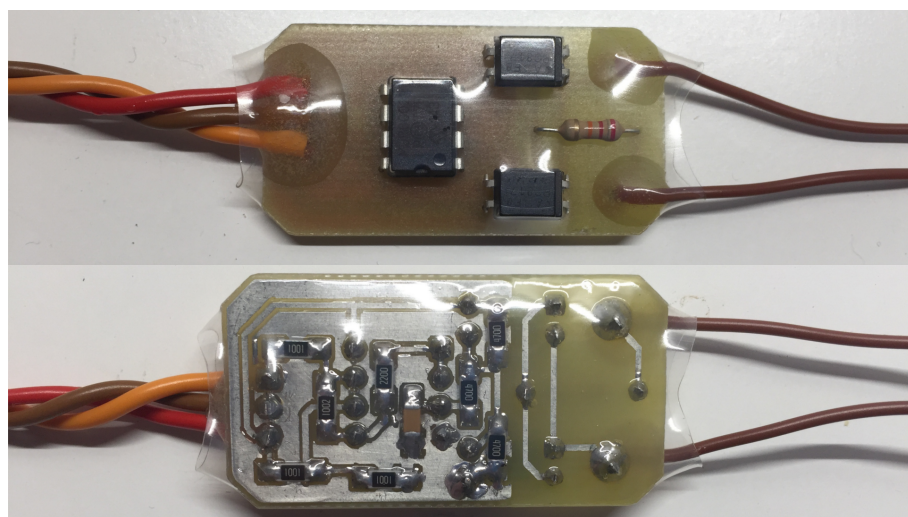


Figure 3.16: RPM sensor

The battery's open-circuit voltage is needed here, which changes as the battery is discharging. The following simple linear model is used¹²:

$$U_{bat} = 36.0V + 6.0V \frac{Q_{bat}}{Q_0} \quad (3.42)$$

The remaining battery capacity Q_{bat} is updated with the estimated current (3.41) as follows:

$$Q_{bat} = Q_0 - \int_{t_0}^t I_{est}(t')dt' \quad (3.43)$$

Figure 3.18 shows the output of the last equation for a recorded test-flight. The modeled battery discharge matches the real one relatively closely, which indicates a good current estimate.

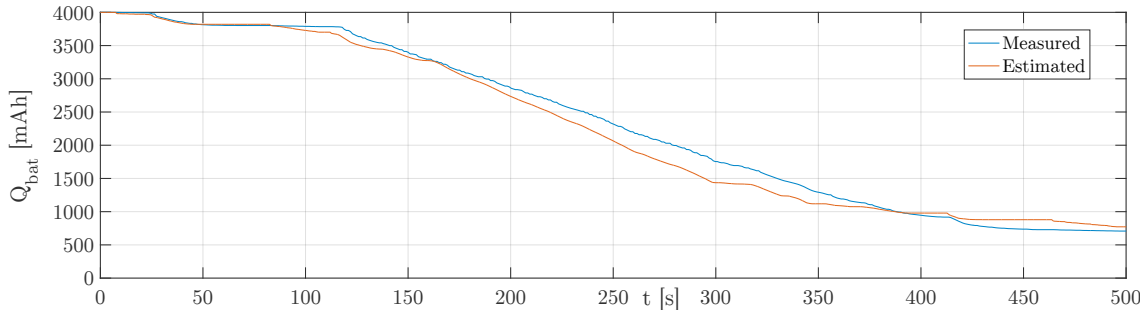


Figure 3.17: Flight battery capacity from measurement (blue) and estimated (red) current

¹² Which matches quite well for LiPo batteries between 20% and 100% charge

Chapter 4

Lateral Stability Augmentation

The lateral stability augmentation system (SAS) consists of a yaw damper, a roll damper, a bank angle controller and a sideslip angle controller (turn coordinator) as seen in Figure 4.1. The controller gains are labeled k_R , k_P , k_ϕ and k_β . In a sustained turn the plane experiences a constant yaw rate, which shall not be corrected by the yaw damper. Therefore a highpass filter (yaw rate washout filter)

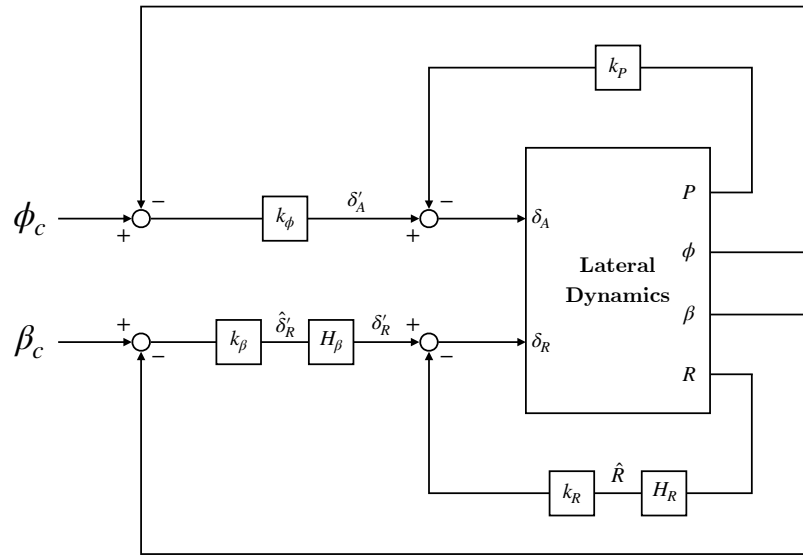


Figure 4.1: Block diagram of lateral stability augmentation system

H_R is added into the yaw damper feedback loop [3, pp.672]. H_β is an integrator to improve the steady state tracking of the sideslip controller.

The pilot's stick inputs no longer control the aileron and rudder deflection, but instead they command a roll rate and sideslip angle. The commanded roll rate is then integrated by the flight computer into a bank angle command for the SAS.

4.1 Linearized Dynamics

The lateral linear state space system is derived from the nonlinear *Simulink* model of chapter 2 with the help of *Simulink's Linear Analysis Tool*:

$$\dot{\mathbf{x}} = A\mathbf{x} + B\mathbf{u} \quad (4.1a)$$

$$\mathbf{y} = C\mathbf{x} \quad (4.1b)$$

with the state, input and output vector:

$$\mathbf{x} = [\phi \ \beta \ P \ R]^T$$

$$\mathbf{u} = [\delta_A \ \delta_R]^T$$

$$\mathbf{y} = [\phi \ \beta \ P \ R]^T$$

The trim conditions are steady-state level flights at three different airspeeds:

- Trim condition 1: $V_T = 15 \frac{m}{s}$; Flaps full down
- Trim condition 2: $V_T = 20 \frac{m}{s}$; Flaps up
- Trim condition 3: $V_T = 30 \frac{m}{s}$; Flaps up

The two inputs (aileron and rudder) from (4.1) are then connected to first order lags, which represent the actuator dynamics [3, pp.709]:

$$H_{servo} = \frac{1}{1 + T_{servo}s} \quad (4.2)$$

Here T_{servo} is the time constant of the actuator (approximately 0.04s)¹³.

The yaw rate washout filter is a first order highpass with time constant T_R [3, pp. 673]:

$$H_R = \frac{T_R s}{1 + T_R s} \quad (4.3)$$

¹³ Special high speed servos are used for maximum performance

Closing the inner control loop with the roll and yaw damper leads to a new state equation:

$$\dot{\mathbf{x}} = (\hat{A}_i - \hat{B}_i K_1 \hat{C}_i) \mathbf{x} + \hat{B}_i \mathbf{u}' \quad (4.4a)$$

$$\mathbf{y} = \hat{C}_i \mathbf{x} \quad (4.4b)$$

\hat{A}_i , \hat{B}_i and \hat{C}_i are found by connecting the yaw rate output R from (4.1) to the washout filter H_R (4.3). The gain matrix K_1 and the new input vector \mathbf{u}' are:

$$K_1 = \begin{bmatrix} 0 & 0 & k_P & 0 \\ 0 & 0 & 0 & k_R \end{bmatrix}$$

$$\mathbf{u}' = [\delta'_A \ \delta'_R]^T$$

The outer control loop can be closed with the bank controller and turn coordinator:

$$\dot{\mathbf{x}} = (\hat{A}_o - \hat{B}_o K_3 \hat{C}_o) \mathbf{x} + \hat{B}_o K_2 \mathbf{w} \quad (4.5a)$$

$$\mathbf{y} = \hat{C}_o \mathbf{x} \quad (4.5b)$$

\hat{A}_o , \hat{B}_o and \hat{C}_o are found by connecting the integrator

$$H_\beta = \frac{T_\beta + s}{s} \quad (4.6)$$

to the rudder input δ'_R of (4.4). The gain matrices K_2 , K_3 and the input vector of the closed outer loop system are:

$$K_2 = \begin{bmatrix} k_\phi & 0 \\ 0 & k_\beta \end{bmatrix} \quad K_3 = \begin{bmatrix} k_\phi & 0 & 0 & 0 \\ 0 & k_\beta & 0 & 0 \end{bmatrix}$$

$$\mathbf{w} = [\phi_c \ \beta_c]^T$$

4.2 Controller Design

All four gains and all two time constants in Figure 4.1 are gain-scheduled in dependence of the airspeed V_T . They are computed by performing a linear fit on the controller parameters found for the different trim conditions. To avoid unexpected values, the airspeed used to compute the six SAS parameters is limited to a sensible range:

$$15 \frac{m}{s} \leq V_T \leq 40 \frac{m}{s} \quad (4.7)$$

4.2.1 Roll Damper

The design requirement for the roll damper is to achieve a damping of $\zeta = \sqrt{2}/2$ for the dominant pole pair of the transfer function from δ'_A to P (4.4).

Using *Matlab Control System Designer* and performing a linear fit leads to:

$$k_P = -0.58 + 0.016V_T \quad (4.8)$$

4.2.2 Bank Controller

The step response of the transfer function from ϕ_c to ϕ (4.4) shall follow a second-order reference system with:

$$\zeta = \sqrt{2}/2 \Rightarrow \% OS = 4.33 \quad \text{from [10, pp.180]}$$

$$T_r = \frac{0.8rad}{P_{max}/2} \Rightarrow \omega_n = \frac{2.150P_{max}}{1.6rad} \quad \text{from [10, pp.181]}$$

P_{max} is the maximum achievable roll rate with full aileron deflection.

Using *Matlab Control System Tuner* and performing a linear fit leads to:

$$k_\phi = -3.23 + 0.051V_T \quad (4.9)$$

The bank command for the SAS is computed by integrating the pilot's aileron stick command. The integration factors are chosen to yield a maximum commanded roll rate P_{cmax} half of the achievable roll rate P_{max} :

$$P_{cmax} = 0.425 + 0.125V_T \quad (4.10)$$

In a vertical climb or descent, the bank angle becomes singular. Therefore the bank controller is bypassed for pitch angles above/below 60 degrees. During these phases the stick input is fed forward to δ'_A with a gain k_A , to ensure a similar roll-rate with and without the bank controller. It is found to be¹⁴:

$$k_A = 1 - k_P P_{cmax} \quad (4.11)$$

¹⁴ By assuming that $P \simeq \delta_A P_{cmax}$

4.2.3 Yaw Damper

The yaw damper is designed to achieve a damping of $\zeta = \sqrt{2}/2$ on the dominant pole pair of the transfer function δ'_R to R . Furthermore, the washout filter pole is placed at the same distance from the origin as the two complex zeros in the open loop transfer function [3, pp.674].

Using *Matlab Control System Designer* and performing a linear fit leads to:

$$k_R = -0.44 + 0.0084V_T \quad (4.12)$$

$$T_R = 0.56 + 0.054V_T \quad (4.13)$$

Discretizing the controller at a sampling rate of 50Hz with the Tustin method [11, pp.186] leads to:

$$H_R = \frac{1}{\frac{1}{T_R} + 100} \cdot \frac{100 - 100z^{-1}}{1 + \frac{\frac{1}{T_R} - 100}{\frac{1}{T_R} + 100}z^{-1}} \quad (4.14)$$

4.2.4 Turn Coordinator

The turn coordinator is tuned to have a slow response for safety reasons. The requirements are:

$$\% OS < 1$$

$$T_r \leq 0.8s$$

Using *Matlab Control System Designer* and performing a linear fit leads to:

$$k_\beta = 0.37 - 0.0091V_T \quad (4.15)$$

$$T_\beta = -12 + 1.5V_T \quad (4.16)$$

Discretizing the controller at a sampling rate of 50Hz with the Tustin method [11, pp.186] leads to:

$$H_\beta = \frac{\left(\frac{T_\beta}{100} + 1\right) + \left(\frac{T_\beta}{100} - 1\right)z^{-1}}{1 - z^{-1}} \quad (4.17)$$

To solve the problem of integration windup, the control law is rewritten as follows:

$$\Delta\delta_R^k = k_\beta \left(\left(\frac{T_\beta}{100} + 1 \right) \Delta\beta^k + \left(\frac{T_\beta}{100} - 1 \right) \Delta\beta^{k-1} \right) \quad (4.18a)$$

$$\delta_R^k = \text{sat}(\delta_R^{k-1} + \Delta\delta_R^k) \quad (4.18b)$$

The final performance of the SAS on the linear system can be seen in figure 4.2. The poles on the far left represent the actuator dynamics. It can be seen that the damping of the dutch roll is greatly increased. Two additional complex poles are introduced by the roll damper and bank controller. The transmission zero (the closed loop system (4.5) is both controllable and observable) is added by the integrator (4.6).

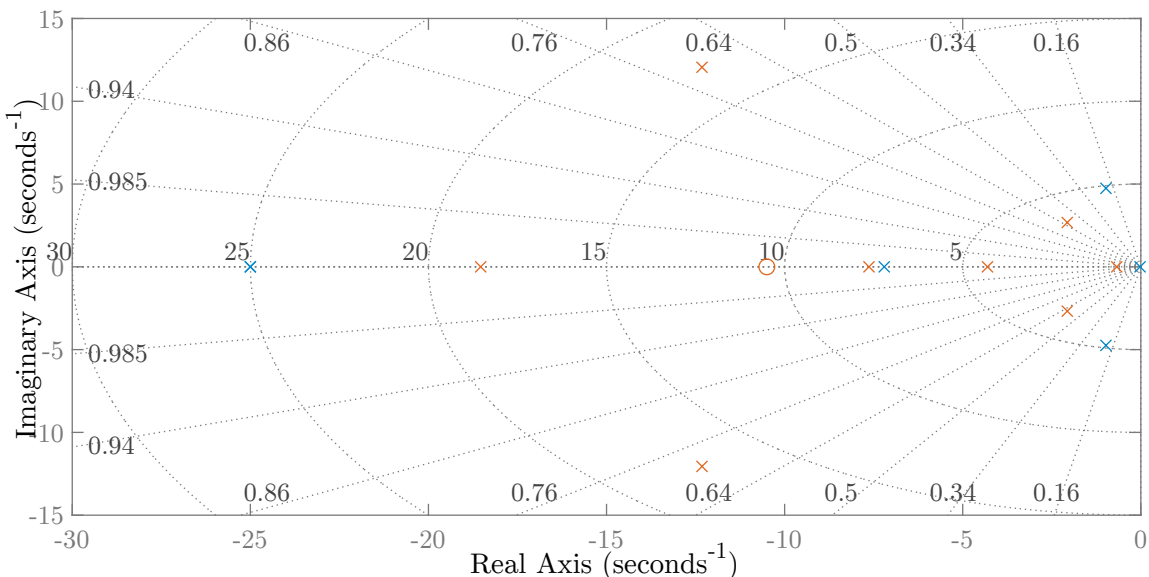


Figure 4.2: Pole-zero map of the open loop (blue) and closed loop (red) lateral system at trim condition 1

4.3 Flight Test Results

The performance of the SAS has been validated with test flights.

Figure 4.3 shows good performance of the bank controller. At 140s a stall has been conducted. Even during this phase no degradation of SAS performance can be seen. A small lag of the bank angle with respect to the command can be seen, since the δ_A to ϕ transfer function is of system type 1 and the controller is of type 0. This although poses no problem, as it cannot be recognized by the pilot and the tracking is still excellent under all flight conditions (even while flying a fast roll, as seen at 170s).

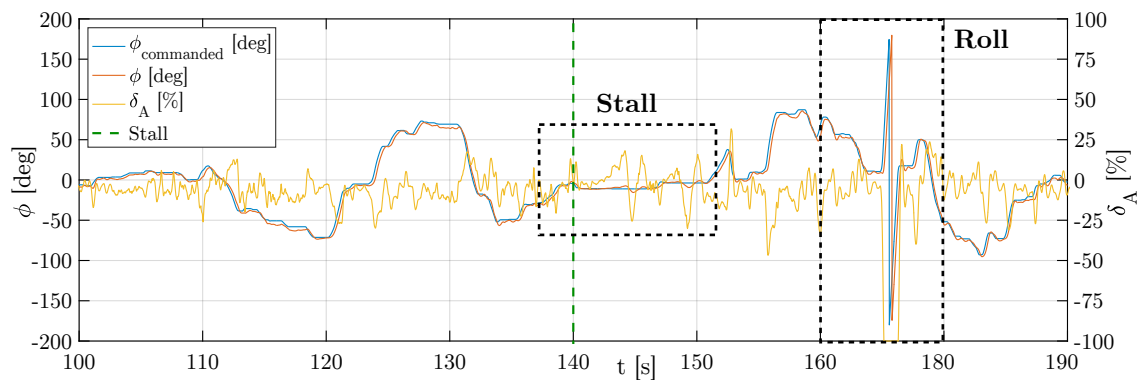


Figure 4.3a: Bank controller performance during test flight

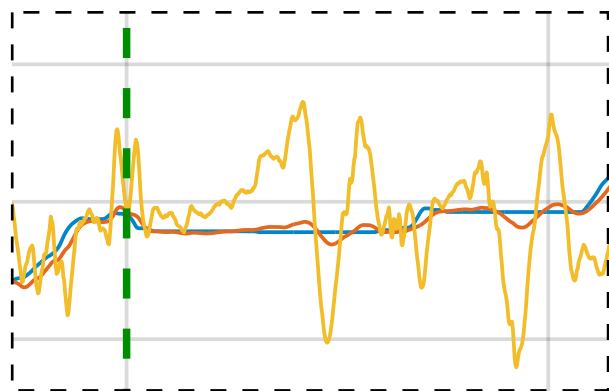


Figure 4.3b (left): Bank controller performance during stall

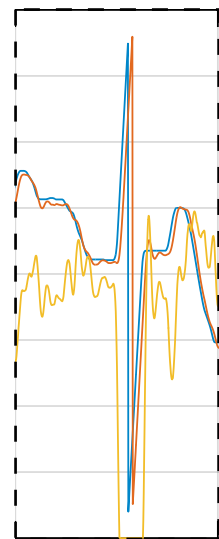


Figure 4.3c (right): Bank controller performance during a fast roll

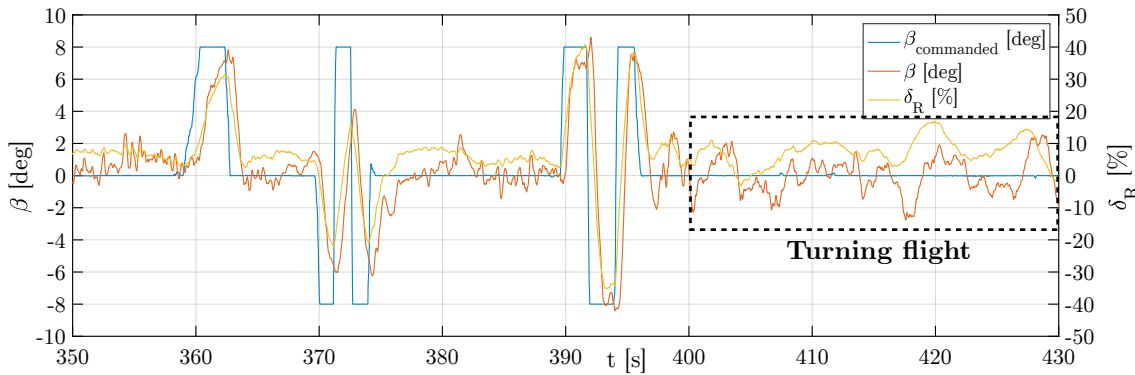


Figure 4.4a: Turn coordinator performance during test flight

Turn coordinator removes steady state error

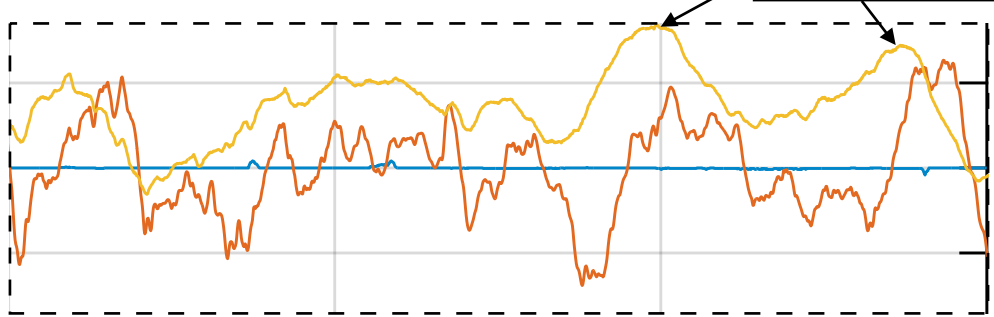


Figure 4.4b: Turn coordinator performance during turning flight

Turn coordinator performance is shown in figure 4.4. As designed, it does not excessively fight against turbulences and the step response is smooth. This is important to reduce the risk of entering a spin at slow airspeeds. The steady state error is removed, especially in sustained turns (performed between 400s and 430s).

Chapter 5

Stall Protection

The idea of the stall protection is to transition the plane into a safe flight state, as soon as the danger of stalling arises. The trajectory must ensure the highest possible climb gradient at any time, since the stall can also happen at a low altitude (e.g. when turning from base to final in a traffic pattern). This can be ensured by guiding the plane at its maximum angle of attack (AOA), regardless of its current energy state (Figure 5.1). The trajectory can be described as follows:

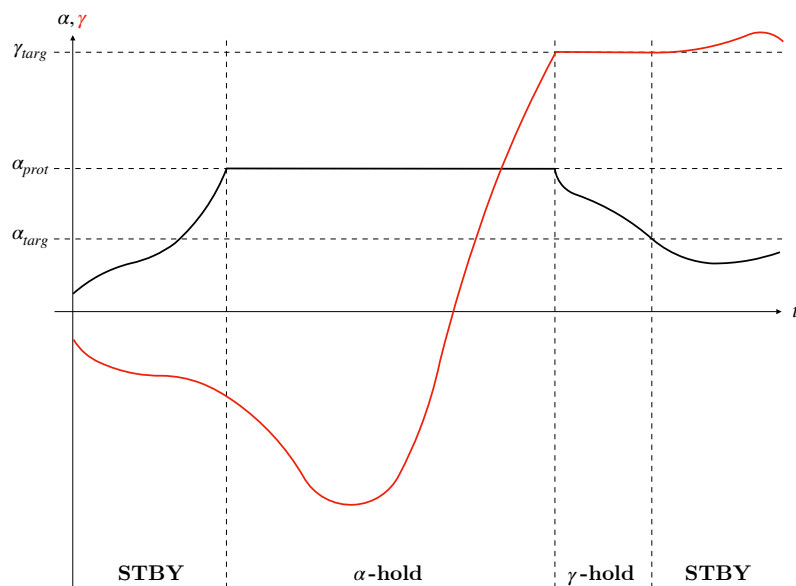


Figure 5.1: Stall protection trajectory

As soon as the AOA reaches the protection AOA α_{prot} , the stall protection changes into α -hold mode. Throttle is applied, either by the flight computer or by the pilot. The guidance system will keep descending, to maintain kinetic energy until the propeller can provide a sufficient amount of thrust. The plane is guided into an ascent, until the required climb gradient γ_{targ} is achieved. At this point the stall protection advances into γ -hold mode until the AOA drops below α_{targ} . At this point stall protection is completed and the system releases elevator control.

5.1 Longitudinal State Space Model

The longitudinal states, inputs and outputs are:

$$\begin{aligned}\mathbf{x} &= [\theta \ V_T \ \alpha \ Q \ \omega_P]^T \\ \mathbf{u} &= [\delta_E \ \delta_T]^T \\ \mathbf{x}_o &= [\alpha \ \gamma]^T\end{aligned}$$

The flight path angle γ can be computed as follows:

$$\gamma = \arcsin(\sin \theta \cos \alpha - \cos \phi \cos \theta \sin \alpha) \quad (5.1)$$

The nonlinear model has to be linearized at a non steady-state point. This leads to the following linear state space representation:

$$\dot{\mathbf{x}} = A\Delta\mathbf{x} + B\Delta\mathbf{u} + \dot{\mathbf{x}}_0 \quad (5.2)$$

Throttle is fixed during stall protection, therefore the state ω_P can be eliminated. By choosing $\delta_{E0} = 0$ and $\Delta\omega_P = 0$, the linear state space model reduces to:

$$\begin{bmatrix} \dot{\theta} \\ \dot{V}_T \\ \dot{\alpha} \\ \dot{Q} \end{bmatrix} = A \begin{bmatrix} \Delta\theta \\ \Delta V_T \\ \Delta\alpha \\ \Delta Q \end{bmatrix} + \begin{bmatrix} 0 \\ 0 \\ 0 \\ B \end{bmatrix} \delta_E + \begin{bmatrix} \dot{\theta}_0 \\ \dot{V}_{T0} \\ \dot{\alpha}_0 \\ \dot{Q}_0 \end{bmatrix} \quad (5.3)$$

The matrix A , scalar B and vector $\dot{\mathbf{x}}_0$ depend on the complete 9-component state vector. Some simplifications are now made, to reduce the dependency to only three independent parameters. The state ω_P is the first independent state. If it is

assumed, that the state of the plane may be unsteady, but still controllable, following states can be fixed¹⁵:

$$\alpha_0 = \alpha_{prot}; P_0 = 0; \beta_0 = 0$$

A logical step would be, to choose the bank angle ϕ and climb gradient γ as the remaining independent parameters. But γ can not be measured directly and the dynamics change significantly under high load factors n_z with zero bank, as it is the case in a pull-up maneuver¹⁶. An alternative choice is n_z and the pitch attitude θ , which are both readily available from measurements. With these assumptions, the linearization point is found to be¹⁷:

$$\phi_0 = \arccos\left(\frac{\cos \alpha_0}{n_z \cos \gamma_0}\right) \quad (5.4a)$$

$$V_{T0} = \sqrt{\frac{2mg n_z}{\rho S_W C_A(\alpha_0) \cos \alpha_0}} \quad (5.4b)$$

$$Q_0 = \frac{g \cos \theta_0}{V_T \cos \alpha_0} \left(n_z \frac{\cos \gamma_0}{\cos \alpha_0} - \frac{1}{n_z} \frac{\cos \alpha_0}{\cos \gamma_0} \right) \quad (5.4c)$$

$$R_0 = \frac{g \cos \theta_0}{V_T \cos \alpha_0} \sin \phi_0 \quad (5.4d)$$

It can be shown, that the substitution of ϕ with n_z only changes Q_0 ¹⁸.

The dependent parameters can now be approximated by a second-order fit (see also figure 5.2) of the following form ($e(n_z, \theta, \omega_P)$ stands for an arbitrary element of (5.3)):

$$\begin{aligned} e(n_z, \theta, \omega_P) = & p_1 n_z^2 + p_2 \theta^2 + p_3 \omega_P^2 + p_4 n_z \theta + p_5 n_z \omega_P \\ & + p_6 \theta \omega_P + p_7 n_z + p_8 \theta + p_9 \omega_P + p_{10} \end{aligned} \quad (5.5)$$

¹⁵ The SAS ensures the latter two conditions

¹⁶ Initial tests showed, that the load factor can easily exceed 2g at the end of the α -hold phase

¹⁷ γ_0 can be found by solving (5.1) and (5.4a)

¹⁸ Compare [3, pp.526] with [3, pp.539]

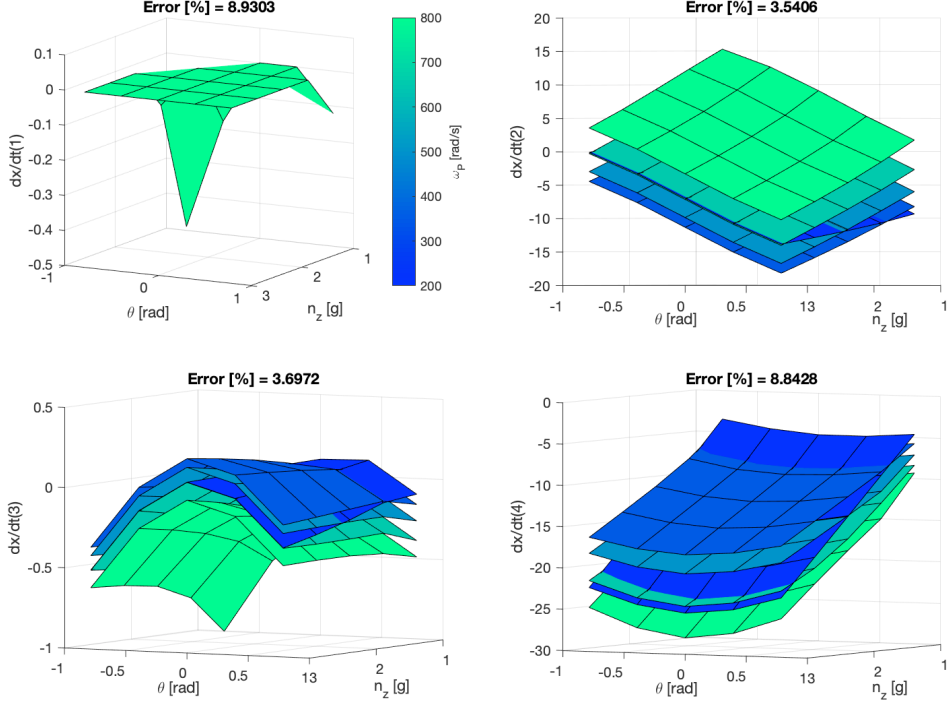


Figure 5.2: Parameter surfaces for \dot{x}_0

5.2 Control Laws

The linear state space model (5.3) can be discretized, yielding:

$$\begin{bmatrix} \theta^{k+1} \\ V_T^{k+1} \\ \alpha^{k+1} \\ Q^{k+1} \end{bmatrix} = \begin{bmatrix} \theta^k \\ V_T^k \\ \alpha^k \\ Q^k \end{bmatrix} + \Delta T A \begin{bmatrix} \Delta\theta^k \\ \Delta V_T^k \\ \Delta\alpha^k \\ \Delta Q^k \end{bmatrix} + \Delta T \begin{bmatrix} 0 \\ 0 \\ 0 \\ B \end{bmatrix} \delta_E + \Delta T \begin{bmatrix} \dot{\theta}_0 \\ \dot{V}_{T0} \\ \dot{\alpha}_0 \\ \dot{Q}_0 \end{bmatrix} \quad (5.6)$$

ΔT is the discretization time step and will be adjusted later on to limit the control action of the dead-beat controller. (5.6) can be further simplified to improve computational efficiency, by removing elements close to zero and elements not needed due to $\Delta\theta^k = 0$:

$$\begin{bmatrix} \Delta\theta^{k+1} \\ \Delta V_T^{k+1} \\ \Delta\alpha^{k+1} \\ \Delta Q^{k+1} \end{bmatrix} = \begin{bmatrix} \Delta\theta^k \\ \Delta V_T^k \\ \Delta\alpha^k \\ \Delta Q^k \end{bmatrix} + \Delta T \begin{bmatrix} \sim 0 & 0 & a_1 \\ \sim A_{11} & A_{12} & A_{13} \\ a_2 & A_{21} & A_{22} & A_{23} \\ \sim A_{31} & A_{32} & A_{33} \end{bmatrix} \begin{bmatrix} \Delta\theta^k \\ \Delta V_T^k \\ \Delta\alpha^k \\ \Delta Q^k \end{bmatrix} + \Delta T \begin{bmatrix} 0 \\ 0 \\ 0 \\ B \end{bmatrix} \delta_E + \Delta T \begin{bmatrix} 0 \\ dx_1 \\ dx_2 \\ dx_3 \end{bmatrix} \quad (5.7)$$

Since high bank angles impose high load factors, the SAS reduces the allowed bank to 45 degrees in α -hold and γ -hold mode.

5.2.1 Standby Mode

In this mode the controller is deactivated. The AOA is monitored and as soon as it reaches α_{prot} the controller switches to α -hold mode.

5.2.2 α -Hold Mode

In α -hold, a dead-beat controller based on (5.7) is applied to the elevator. The goal is to predict any deviations of the AOA based on the plane's current state and apply corrective actions in advance. This is achieved by the following three step process:

- Predict states θ^{k+1} , V_T^{k+1} , α^{k+1}

$$\Delta\theta^{k+1} = \Delta T a_1 \Delta Q^k \quad (5.8a)$$

$$\Delta V_T^{k+1} = \Delta T \left(\left(\frac{1}{\Delta T} + A_{11} \right) \Delta V_T^k + A_{12} \Delta \alpha^k + A_{13} \Delta Q^k + d x_1 \right) \quad (5.8b)$$

$$\Delta \alpha^{k+1} = \Delta T \left(A_{21} \Delta V_T^k + \left(\frac{1}{\Delta T} + A_{22} \right) \Delta \alpha^k + A_{23} \Delta Q^k + d x_2 \right) \quad (5.8c)$$

- Compute the required state Q^{k+1} by setting $\Delta\alpha^{k+2} = 0$

$$\Delta Q^{k+1} = \frac{1}{A_{23}} \left(-a_2 \Delta\theta^{k+1} - A_{21} \Delta V_T^{k+1} - \left(\frac{1}{\Delta T} + A_{22} \right) \Delta \alpha^{k+1} - d x_2 \right) \quad (5.9)$$

- Compute the elevator deflection δ_E^k to achieve Q^{k+1}

$$\delta_E = \frac{1}{B} \left(\frac{\Delta Q^{k+1}}{\Delta T} - A_{31} \Delta V_T^k - A_{32} \Delta \alpha^k - \left(\frac{1}{\Delta T} + A_{33} \right) \Delta Q^k - d x_3 \right) \quad (5.10)$$

The step time has been experimentally adjusted utilizing flight tests in *Simulink* to $\Delta T = 0.05\text{s}$. If the flight path γ reaches γ_{trag} at any time, the stall protection advances into γ -hold mode.

5.2.3 γ -Hold Mode

After reaching the safe climb gradient, the flight computer holds the elevator at zero degree deflection to reduce the AOA. Since the propeller already produces a high amount of thrust at this point, the AOA drops very fast below α_{targ} and the stall protection switches to standby mode.

5.3 Flight Test Results

Three flights in different environmental conditions (including rain, heavy turbulence and winds up to 20kts) with a total of sixteen stall tests have been performed up to the publishing date of this work. Every time the controller was able to prevent a stall and hold the AOA in a small band. Figure 5.3 shows two such stall tests.

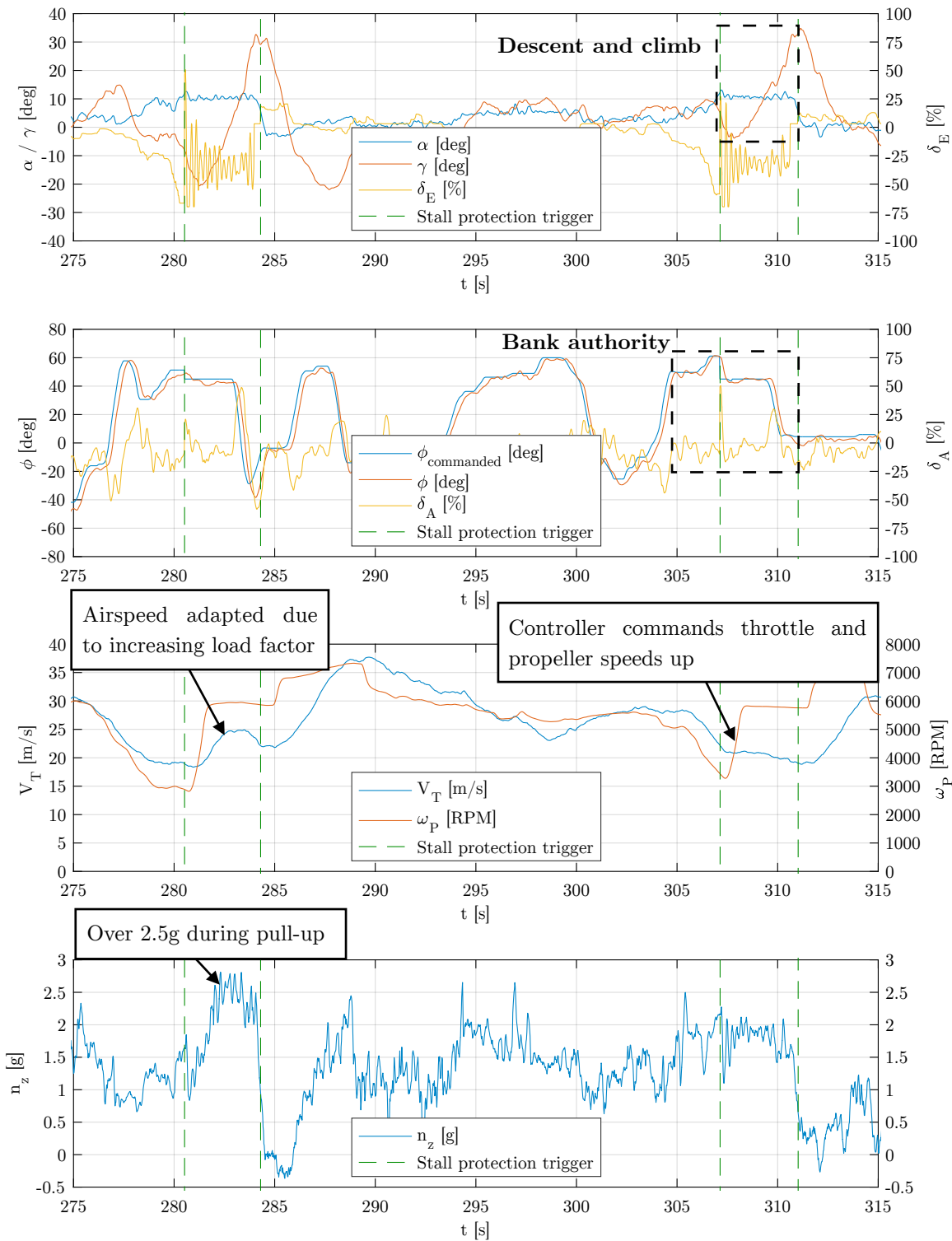


Figure 5.3a: Stall protection performance

The second one especially shows the performance under different bank angles. Upon entering the stall protection, a right bank of 60 degrees was automatically reduced to 45 degrees. After 5 seconds a quick pilot input was issued to roll the plane back to wings level, still under control of the stall protection.

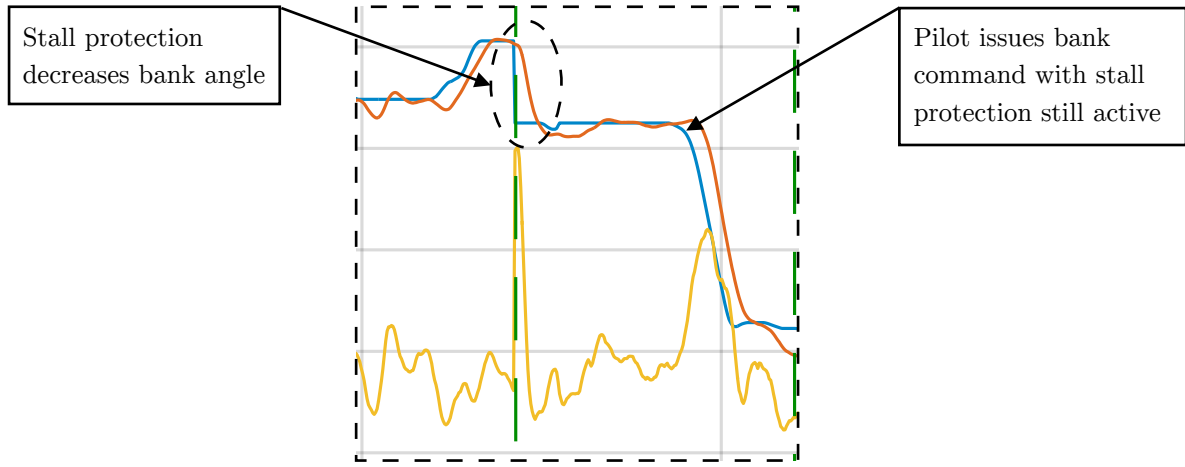


Figure 5.3b: Stall protection performance at high bank angles

Both tests also show how the controller continues the descent at the beginning of the α -hold phase, waiting until the accelerating propeller produces enough thrust to allow a climb. Furthermore, the controller successfully manages to adjust the plane's airspeed depending on the load factor, which justifies the substitution of ϕ with n_z made in chapter 5.1.

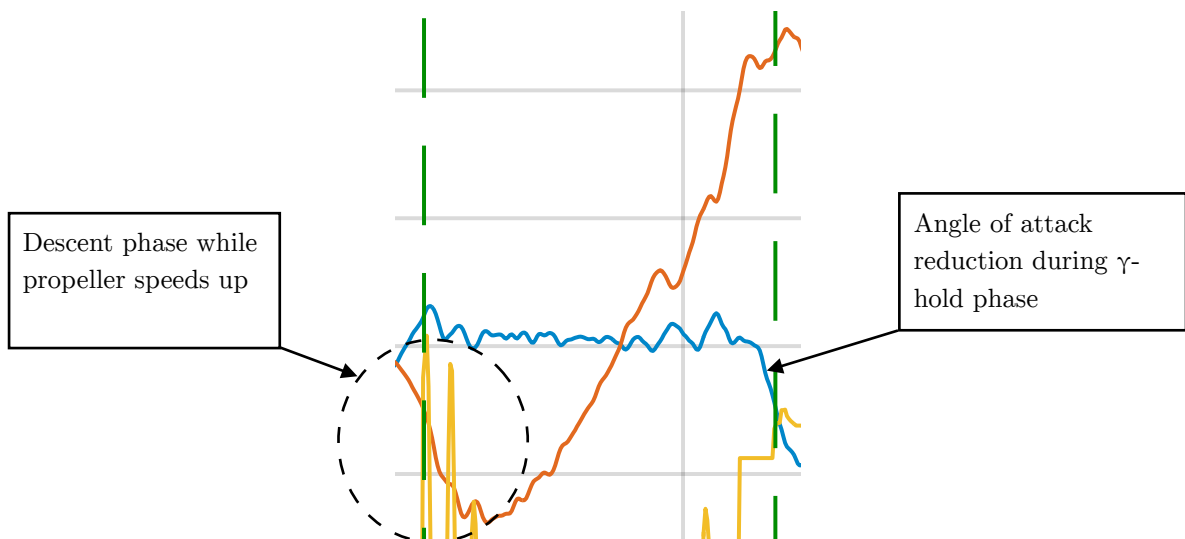


Figure 5.3c: Energy management through descending and climbing during stall protection

Appendix A

Nomenclature

Notation of vectors is the same as in [1], if not explicitly stated otherwise. It shall be briefly summarized here:

A bold letter indicates a vector.

A right subscript adds an object or point to the vector's physical context.

A right superscript specifies a coordinate system, the vector's components are given in.

A left superscript specifies a frame, in which a derivative is taken.

Symbol	Definition
b	Wing span
B	Magnetic flux density vector
c	Chord length
$c_{l/d/m}$	Section lift/drag/moment coefficient
c_p	Pressure coefficient
c_{pw}	Propwash factor
C	Aerodynamic side force (crosswind force)
$C_{L/D/C}$	Body lift/drag/side force coefficient
$C_{LA/M/N}$	Body rolling/pitching/yawing moment coefficient
D	Aerodynamic drag force

Symbol	Definition
\mathbf{f}	Specific force vector
$F_{\bullet x}$	Force in x-direction
$F_{\bullet y}$	Force in y-direction
$F_{\bullet z}$	Force in z-direction
\mathbf{F}_A	Aerodynamic forces
\mathbf{F}_T	Propulsive forces (Propeller forces)
\mathbf{i}_{\bullet}	Unit vector along x-axis of \bullet coordinate system
I	Motor current
$I_{a \times a}$	Identity matrix of size a
I_P	Propeller moment of inertia
\mathbf{j}_{\bullet}	Unit vector along y-axis of \bullet coordinate system
J_0	Free stream advance ratio
J_1	Propeller hub advance ratio
\mathbf{k}_{\bullet}	Unit vector along z-axis of \bullet coordinate system
L	Aerodynamic lift force
L_{\bullet}	Moment in x-direction
L_A	Aerodynamic rolling moment
M	Aerodynamic pitching moment
M_{\bullet}	Moment in y-direction
\mathbf{M}_A	Aerodynamic moments
\mathbf{M}_T	Propulsive moments (Propeller moments)
\mathbf{n}	Load factor (vector)
N	Aerodynamic yawing moment
N_{\bullet}	Moment in z-direction

Symbol	Definition
p	Propeller pitch
P	Roll rate
q	Rotation quaternion
Q	Pitch rate
r	Position vector
r_V	Inertial position of the plane's C.G.
R	Yaw rate
$R_{0/1/2}$	Radius of the propeller streamtube
R_i	Radius of the propeller affected stream
R_P	Propeller radius
S	Reference (wing) area
T_{BA}	Transformation matrix from system A to system B
$u_{0/1/2}$	Axial air velocity in the propeller streamtube
U	Velocity component along i_V axis
U'	Relative air velocity component along i_V axis
U_i	Propeller induced axial air velocity
v	Velocity vector
v_{rel}	Velocity of the plane's C.G. with respect to the air
v_V	Inertial velocity of the plane's C.G.
v_W	Inertial wind velocity (velocity of the surrounding air)
V	Velocity component along j_V axis
V'	Relative air velocity component along j_V axis
V_T	Magnitude of the relative air velocity vector
W	Velocity component along k_V axis

Symbol	Definition
W'	Relative air velocity component along k_V axis
α	Angle of attack
β	Sideslip angle
γ	Flight path angle
$\delta_{A/E/R/T/F}$	Normalized aileron, elevator, rudder, throttle, flaps command
θ	Pitch angle
ϕ	Bank angle
Φ	Orientation vector (Euler angles)
ψ	Heading
ω	Angular velocity vector
ω_V	Inertial angular velocity of the plane
$\Omega_{0/1/2}$	Air vorticity in the propeller streamtube
Ω_i	Propeller induced air vorticity

The different coordinate systems are summarized here:

Name	Index	Definition
Earth	E	Aligned north-east-down (ned)
Vehicle	V	Aligned with vehicle front-right-down
Hub	H	Aligned x with vehicle front, y-z with radial disturbance component
Propeller	P	Aligned x with vehicle front, y with radial outward propeller direction, z in rotation direction
Wind	W	Aligned with the relative air velocity vector, y parallel to vehicle y-axis

Appendix B

Propulsion Data

B.1 Propeller Disk Air Velocity State

The propeller's algebraic equations can only be solved numerically¹⁹, which poses a big computational cost when running a real-time flight simulation. This can be avoided by tabulating data for the advance ratio J_0 , as well as providing an estimation for ω'_P . By utilizing (2.8), (2.10), and (2.27a), one can find following identity:

$$\frac{u_0}{\omega'_P R_P} = \frac{u_1}{\omega'_P R_P} - \frac{C_{TFx}}{2\pi} \frac{\omega'_P R_P}{u_1}$$

With the definition of the free stream advance ratio

$$J_0 = \frac{u_0}{\omega'_P R_P} \quad (\text{B.1})$$

a relation between the free stream advance ratio J_0 and the propeller hub advance ratio J_1 can be established:

$$J_0 = J_1 - \frac{C_{TFx}}{2\pi J_1} \quad (\text{B.2})$$

Combining equations (2.10) and (2.27a) leads to the following expression:

$$u_2 = u_0 \sqrt{\frac{2C_{TFx}}{\pi J_0^2} + 1}$$

¹⁹ The desired values are U_i (2.10), Ω_i (2.11), F_{Tx} (2.19a), and L_T (2.19b)

Using further (2.9), (2.11), (2.16), and (2.27b), one can show that:

$$\omega'_P = \frac{\omega_P}{1 - \frac{4C_{TMx}A(J_0)}{\pi J_0(1 + A(J_0))^2}} \quad (\text{B.3a})$$

$$A(J_0) = \sqrt{\frac{2C_{TFx}}{\pi J_0^2} + 1} \quad (\text{B.3b})$$

The last result could be numerically solved for ω'_P (J_0 also depends on ω'_P), but by calculating the advance ratio as

$$J_0 = \frac{u_0}{\omega_P R_P}$$

instead of (B.1), one obtains a close estimate for ω'_P , which is used in real-time flight simulation.

B.2 Thrust Coefficients

Equation (2.28) contains 18 parameters, dependent only on the hub advance ratio J_1 . These coefficients are obtained by numerically integrating parts of (2.19) as it is described in chapter 2.1.2. The integrals for the force coefficients are given below:

$$f_{x1} = \int_0^{\bar{R}_{stall}(J_1)} \frac{1}{2} (J_1^2 + \bar{r}^2) \bar{c}(\bar{r}) \cos(\alpha_U(J_1, \bar{r})) d\bar{r} \quad (\text{B.4a})$$

$$f_{x2} = \int_{\bar{R}_{stall}(J_1)}^1 \frac{1}{2} (J_1^2 + \bar{r}^2) (\alpha_0(\bar{r}) - \alpha_U(J_1, \bar{r})) \bar{c}(\bar{r}) \cos(\alpha_U(J_1, \bar{r})) d\bar{r} \quad (\text{B.4b})$$

$$f_{x3} = - \int_0^1 \frac{1}{2} (J_1^2 + \bar{r}^2) (\alpha_0(\bar{r}) - \alpha_U(J_1, \bar{r}))^2 \bar{c}(\bar{r}) \sin(\alpha_U(J_1, \bar{r})) d\bar{r} \quad (\text{B.4c})$$

$$f_{y1} = \int_0^{\bar{R}_{stall}(J_1)} \frac{1}{2} \left[-\bar{r} \sin(\alpha_U(J_1, \bar{r})) + \frac{1}{2} J_1 \cos(\alpha_U(J_1, \bar{r})) \right] \bar{c}(\bar{r}) d\bar{r} \quad (\text{B.4d})$$

$$f_{y2} = \int_{\bar{R}_{stall}(J_1)}^1 \frac{1}{2} \left[\left(-\bar{r} (\alpha_0(\bar{r}) - \alpha_U(J_1, \bar{r})) - \frac{1}{2} J_1 \right) \sin(\alpha_U(J_1, \bar{r})) + \frac{1}{2} J_1 (\alpha_0(\bar{r}) - \alpha_U(J_1, \bar{r})) \cos(\alpha_U(J_1, \bar{r})) \right] \bar{c}(\bar{r}) d\bar{r} \quad (\text{B.4e})$$

$$f_{y3} = \int_0^1 \frac{1}{2} \left[\left(-\bar{r}(\alpha_0(\bar{r}) - \alpha_U(J_1, \bar{r}))^2 - J_1(\alpha_0(\bar{r}) - \alpha_U(J_1, \bar{r})) \right) \cos(\alpha_U(J_1, \bar{r})) - \frac{1}{2} J_1(\alpha_0(\bar{r}) - \alpha_U(J_1, \bar{r}))^2 \sin(\alpha_U(J_1, \bar{r})) \right] \bar{c}(\bar{r}) d\bar{r} \quad (\text{B.4f})$$

$$f_{y4} = \int_0^{\bar{R}_{stall}(J_1)} \frac{1}{2} \left[\bar{r} J_1 \sin(\alpha_U(J_1, \bar{r})) + \frac{1}{2} \bar{r}^2 \cos(\alpha_U(J_1, \bar{r})) \right] \bar{c}(\bar{r}) d\bar{r} \quad (\text{B.4g})$$

$$f_{y5} = \int_{\bar{R}_{stall}(J_1)}^1 \frac{1}{2} \left[\left(\bar{r} J_1(\alpha_0(\bar{r}) - \alpha_U(J_1, \bar{r})) - \frac{1}{2} \bar{r}^2 \right) \sin(\alpha_U(J_1, \bar{r})) + \frac{1}{2} \bar{r}^2(\alpha_0(\bar{r}) - \alpha_U(J_1, \bar{r})) \cos(\alpha_U(J_1, \bar{r})) \right] \bar{c}(\bar{r}) d\bar{r} \quad (\text{B.4h})$$

$$f_{y6} = \int_0^1 \frac{1}{2} \left[\left(\bar{r} J_1(\alpha_0(\bar{r}) - \alpha_U(J_1, \bar{r}))^2 - \bar{r}^2(\alpha_0(\bar{r}) - \alpha_U(J_1, \bar{r})) \right) \cos(\alpha_U(J_1, \bar{r})) - \frac{1}{2} \bar{r}^2(\alpha_0(\bar{r}) - \alpha_U(J_1, \bar{r}))^2 \sin(\alpha_U(J_1, \bar{r})) \right] \bar{c}(\bar{r}) d\bar{r} \quad (\text{B.4i})$$

The integrals for the moment coefficients are similar:

$$m_{x1} = - \int_0^{\bar{R}_{stall}(J_1)} \frac{1}{2} (J_1^2 + \bar{r}^2) \bar{c}(\bar{r}) \sin(\alpha_U(J_1, \bar{r})) \bar{r} d\bar{r} \quad (\text{B.5a})$$

$$m_{x2} = - \int_{\bar{R}_{stall}(J_1)}^1 \frac{1}{2} (J_1^2 + \bar{r}^2) (\alpha_0(\bar{r}) - \alpha_U(J_1, \bar{r})) \bar{c}(\bar{r}) \sin(\alpha_U(J_1, \bar{r})) \bar{r} d\bar{r} \quad (\text{B.5b})$$

$$m_{x3} = - \int_0^1 \frac{1}{2} (J_1^2 + \bar{r}^2) (\alpha_0(\bar{r}) - \alpha_U(J_1, \bar{r}))^2 \bar{c}(\bar{r}) \cos(\alpha_U(J_1, \bar{r})) \bar{r} d\bar{r} \quad (\text{B.5c})$$

$$m_{y1} = \int_0^{\bar{R}_{stall}(J_1)} \frac{1}{2} \left[-\bar{r} \cos(\alpha_U(J_1, \bar{r})) - \frac{1}{2} J_1 \sin(\alpha_U(J_1, \bar{r})) \right] \bar{c}(\bar{r}) \bar{r} d\bar{r} \quad (\text{B.5d})$$

$$m_{y2} = \int_{\bar{R}_{stall}(J_1)}^1 \frac{1}{2} \left[\left(-\bar{r}(\alpha_0(\bar{r}) - \alpha_U(J_1, \bar{r})) - \frac{1}{2} J_1 \right) \cos(\alpha_U(J_1, \bar{r})) - \frac{1}{2} J_1(\alpha_0(\bar{r}) - \alpha_U(J_1, \bar{r})) \sin(\alpha_U(J_1, \bar{r})) \right] \bar{c}(\bar{r}) \bar{r} d\bar{r} \quad (\text{B.5e})$$

$$m_{y3} = - \int_0^1 \frac{1}{2} \left[\left(-\bar{r}(\alpha_0(\bar{r}) - \alpha_U(J_1, \bar{r}))^2 - J_1(\alpha_0(\bar{r}) - \alpha_U(J_1, \bar{r})) \right) \sin(\alpha_U(J_1, \bar{r})) + \frac{1}{2} J_1(\alpha_0(\bar{r}) - \alpha_U(J_1, \bar{r}))^2 \cos(\alpha_U(J_1, \bar{r})) \right] \bar{c}(\bar{r}) \bar{r} d\bar{r} \quad (\text{B.5f})$$

$$m_{y4} = \int_0^{\bar{R}_{stall}(J_1)} \frac{1}{2} \left[\bar{r} J_1 \cos(\alpha_U(J_1, \bar{r})) - \frac{1}{2} \bar{r}^2 \sin(\alpha_U(J_1, \bar{r})) \right] \bar{c}(\bar{r}) \bar{r} d\bar{r} \quad (\text{B.5g})$$

$$m_{y5} = \int_{\bar{R}_{stall}(J_1)}^1 \frac{1}{2} \left[\left(\bar{r} J_1 (\alpha_0(\bar{r}) - \alpha_U(J_1, \bar{r})) - \frac{1}{2} \bar{r}^2 \right) \cos(\alpha_U(J_1, \bar{r})) - \frac{1}{2} \bar{r}^2 (\alpha_0(\bar{r}) - \alpha_U(J_1, \bar{r})) \sin(\alpha_U(J_1, \bar{r})) \right] \bar{c}(\bar{r}) \bar{r} d\bar{r} \quad (\text{B.5h})$$

$$m_{y6} = - \int_0^1 \frac{1}{2} \left[\left(\bar{r} J_1 (\alpha_0(\bar{r}) - \alpha_U(J_1, \bar{r}))^2 - \bar{r}^2 (\alpha_0(\bar{r}) - \alpha_U(J_1, \bar{r})) \right) \sin(\alpha_U(J_1, \bar{r})) + \frac{1}{2} \bar{r}^2 (\alpha_0(\bar{r}) - \alpha_U(J_1, \bar{r}))^2 \cos(\alpha_U(J_1, \bar{r})) \right] \bar{c}(\bar{r}) \bar{r} d\bar{r} \quad (\text{B.5i})$$

Properties denoted with an over-bar are normalized with respect to the propeller radius R_p . When evaluating the above integrals, one has to take care of the singularity at $\bar{r} = 0$. Equations (B.4) and (B.5) only contain J_1 , the blade stall angle α_{max} ²⁰, and three geometric parameters: the propeller radius R_p , the propeller pitch p , and the propeller chord c . The propeller in use is a *XOAR PJA 20x10* with:

$$R_p = 0.254m ; p = 0.254m$$

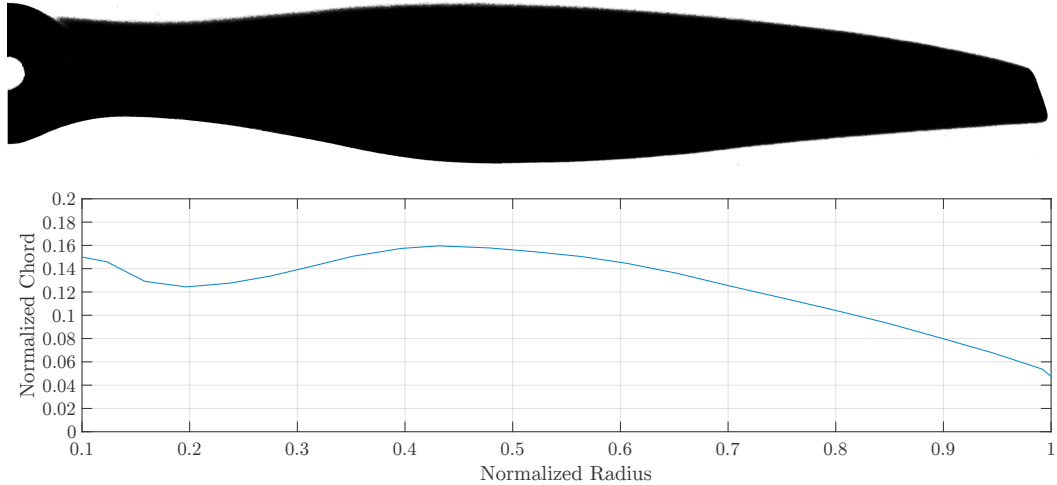


Figure B.1a (top): Propeller photographic projection

Figure B.1b (bottom): Propeller chord length over radius

²⁰ Hidden in \bar{R}_{stall} ; see (2.26)

The chord distribution was determined by a photographic projection of the propeller blade (Figure B.1). This leaves only the three aerodynamic parameters $c_{l\alpha}$, α_{max} , and $c_{d\alpha}$ to be determined, which has been done by performing a static thrust test (Figure B.2). The procedure can be summarized as follows:

1. Thrust F_{Tx} , propeller speed ω_P , motor voltage U , and motor current I are gathered for different throttle settings. With this data, the motor torque can be computed as:

$$L_T = - \frac{UI}{\omega_P} \eta_{mot}$$

2. The static thrust and torque coefficients (C_{TFx} and C_{TMx}) are computed according to (2.27) by taking an average of all measurements.
3. The advance ratio in the static case is $J_0 = 0$. Therefore J_1 results from (B.2).
4. By assuming an α_{max} , $c_{l\alpha}$ and $c_{d\alpha}$ can be computed from (2.28a) and (2.28d).



Figure B.2a: Static thrust test setup

Figure B.2b: Measurement equipment



Figure B.2c: Load cell amplifier

Figure B.2d: Load cell

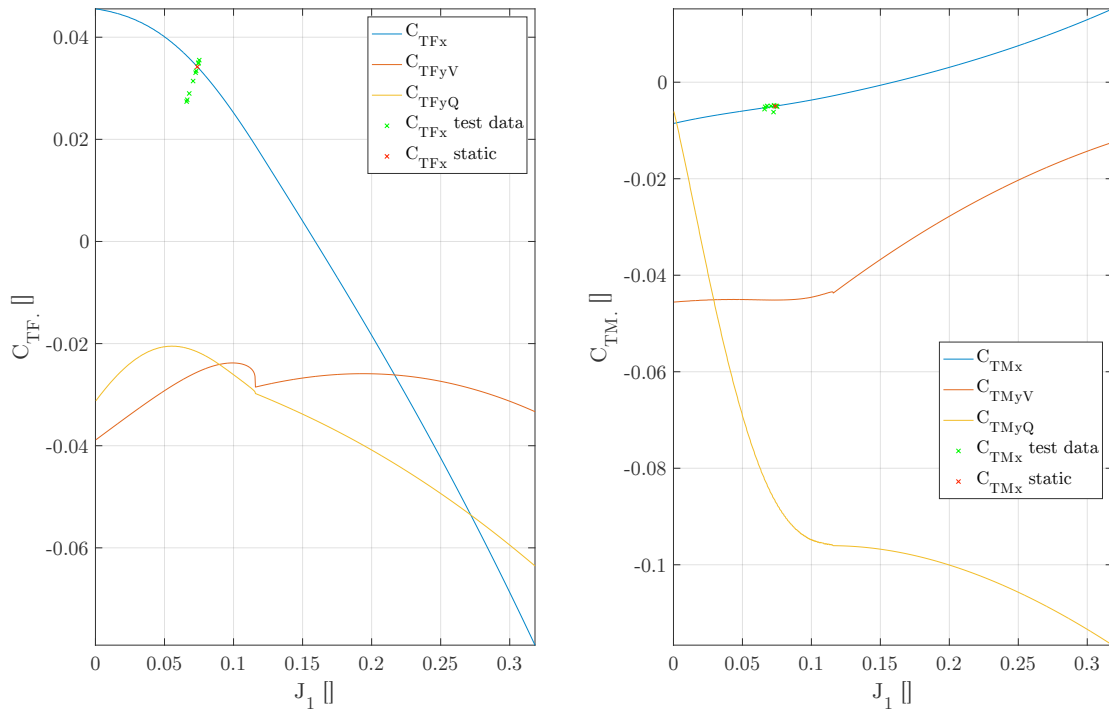


Figure B.3: Experimentally determined thrust coefficients (left forces, right moments)

The resulting thrust coefficients can be seen in figure B.3. By substituting (2.27) into (2.12), the following identity for the propeller efficiency factor can be found:

$$\eta_{prop} = \left| \frac{C_{TFx}}{C_{TMx}} \right| J_1 \quad (\text{B.6})$$

Figure B.4 shows the efficiency factor obtained from the static thrust tests.

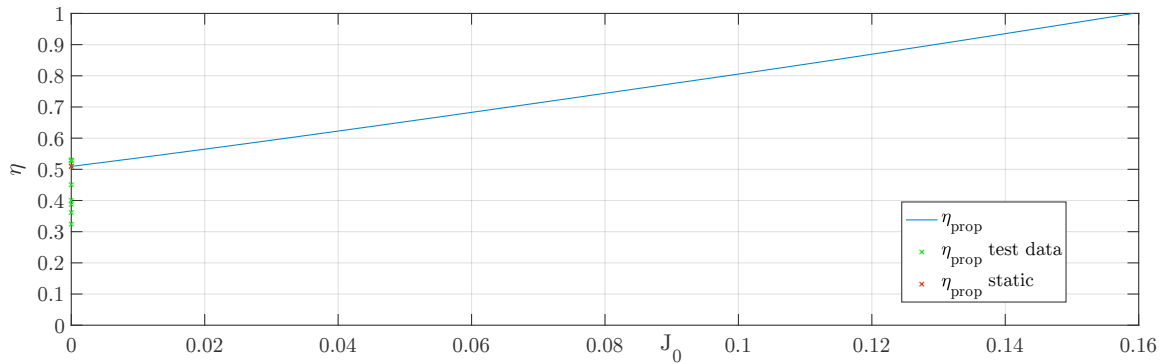


Figure B.4: Efficiency factor of propeller in dependence of free stream advance ratio

B.3 Powertrain

Data for the electric components of the powertrain is obtained from the manufacturer's specifications.

- Motor: Hacker A60-7S V2

Parameter	Value	Description
R_M	26mΩ	Internal resistance
I_0	1.2A	Current due to friction
k_V	22.5V ⁻¹ s ⁻¹	Velocity constant
k_T	44.4e-3 NmA ⁻¹	Torque constant

- Electronic speed controller: Jeti MasterBasic 90 Opto

Parameter	Value	Description
R_{ESC}	2.2mΩ	Internal resistance
t_{acc}	1.11s	Acceleration time constant*
t_{dec}	0.36s	Deceleration time constant*

*The ESC limits motor acceleration and deceleration to avoid overcurrent and losing synchronization.

- Battery: SLS Quantum 65C 10s 4Ah

Parameter	Value	Description
U_{bat}	36V - 42V	Idle voltage
R_{bat}	100mΩ	Internal resistance

Appendix C

Aerodynamic Data

This section describes the derivation of the aerodynamic properties of the vehicle's three lifting surfaces: the main wing, horizontal stabilizer and vertical stabilizer. Some geometric properties of a trapezoidal wing, which are needed for further calculations, are found at [3, pp.174-176]:

$$\begin{aligned} c(y) &= c_t \frac{2y}{b} + c_r \left(1 - \frac{2y}{b}\right) \\ S &= 2 \int_0^{b/2} c(y) dy \\ A &= \frac{b^2}{S} \\ \lambda &= \frac{c_t}{c_r} \\ \bar{c} &= \frac{2}{3} c_r \frac{1 + \lambda + \lambda^2}{1 + \lambda} \\ y_{MAC} &= \frac{b}{2} \frac{\bar{c} - c_r}{c_t - c_r} \end{aligned}$$

Airfoil section data is obtained from a transient CFD simulation in *ANSYS CFX*. The resulting coefficients have to be corrected for the three dimensional flow around a wing. Lift and drag are corrected with simple factors multiplied to the section coefficients. The factors are found by comparing the lift distribution of the wing in question to that of an elliptical wing [7, pp.133-147]:

$$C_{L\alpha} = C_{L\alpha ell} \left(1 - \frac{\tau}{1 + \frac{A}{2\eta}} \right) = \frac{c_{l\alpha}}{1 + \frac{2\eta}{A}} \left(1 - \frac{\tau}{1 + \frac{A}{2\eta}} \right)$$

$$\eta = \frac{c_{l\alpha}}{2\pi}$$

$$k = \frac{C_{L\alpha}}{c_{l\alpha}}$$

$$C_D = C_{Dp} + C_{Di} = C_{Dp} + \frac{C_L^2}{\pi e A}$$

$$e = \frac{1}{1 + \delta}$$

δ, τ from [7, pp.136]

The effects of trailing edge flaps (control surfaces) on the lift and moment coefficients are included in form of empirical data found in [3, pp.168-171].

Finally, the main wing's downwash is estimated with the use of graphical data from [3, pp.216] and:

$$A_{eff} = \frac{A}{1 + \delta} \quad \text{from [7, pp.148]}$$

C.1 Main Wing

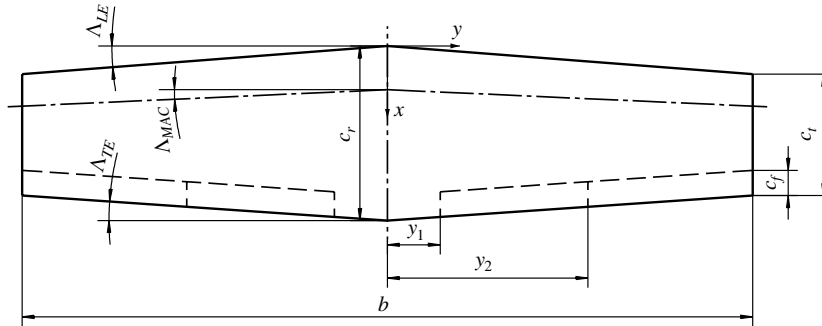


Figure C.1: Main wing geometric properties

Parameter	Value	Description
b	1.5m	wing span
c_r	0.335m	root chord length

Parameter	Value	Description
c_t	0.260m	tip chord length
c_f	0.040m	flap length
y_1	0.070m	
y_2	0.405m	
S	0.446m ²	wing area
A	5.04	aspect ratio
λ	0.776	taper ratio
\bar{c}	0.299m	mean aerodynamic chord (MAC)
y_{MAC}	0.360m	spanwise location of MAC
Λ_{LE}	4.04deg	sweep angle of leading edge
Λ_{TE}	-1.68deg	sweep angle of trailing edge
Λ_{MAC}	2.62deg	sweep angle of MAC
X_{LE}	-0.22m	location of wing leading edge along i_V axis

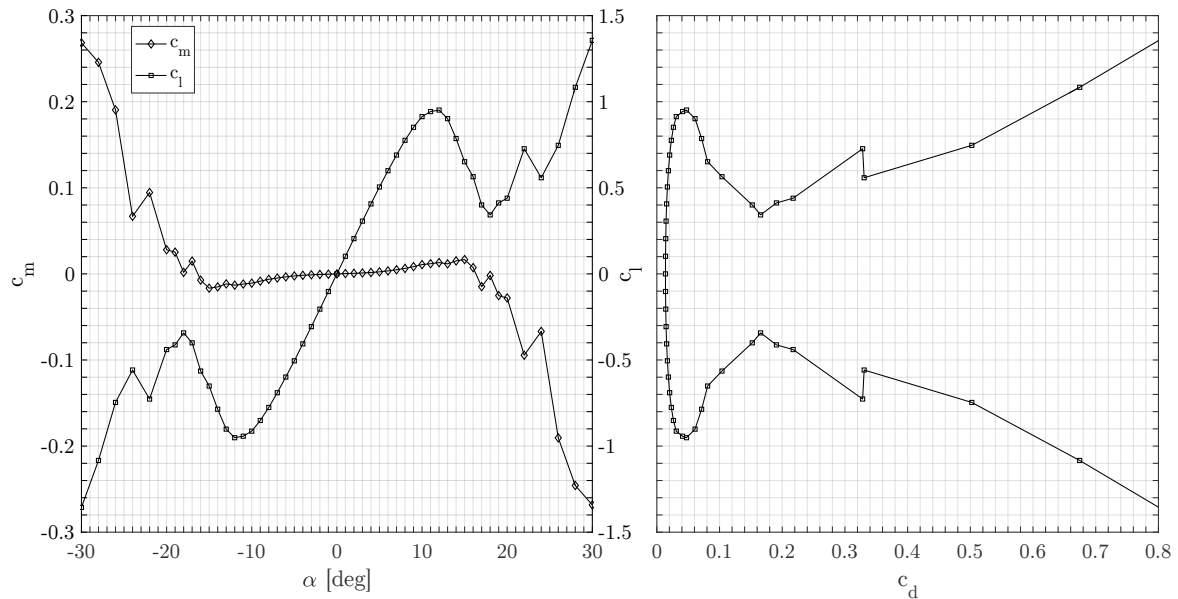


Figure C.2: Section coefficients of the main wing's airfoil at $Re=286000$

Parameter	Value	Description
\bar{x}_{ac}	0.25	normalized position of aerodynamic chord (a.c.)
t/c	0.146	airfoil thickness ratio
i_W	1deg	wing incidence
$c_{l\alpha}$	5.73rad ⁻¹	section lift effectiveness
η	0.912	airfoil efficiency factor
k	0.714	lift correction for 3D-wing
e	0.981	Oswald efficiency number
X_{ac}	0.100m	location of a.c. of 3D-wing
$c_{l\delta_F}$	2.5rad ⁻¹	flap lift effectiveness
$c_{m\delta_F}$	-0.584rad ⁻¹	flap moment effectiveness
$c_{l\delta_A}$	2.7rad ⁻¹	aileron lift effectiveness
$c_{m\delta_A}$	-0.602rad ⁻¹	aileron moment effectiveness
$\frac{d\varepsilon}{d\alpha} \Big _H$	0.48	downwash gradient at horizontal stabilizer

C.2 Horizontal Stabilizer

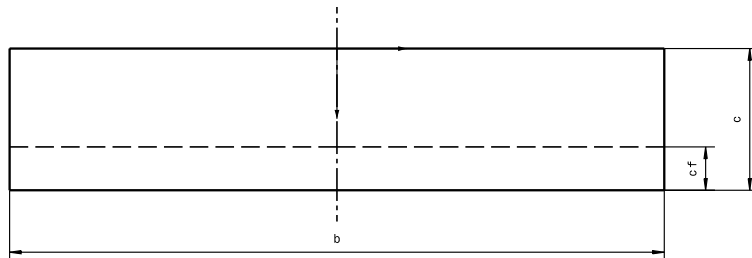


Figure C.3: Horizontal stabilizer geometric properties

Parameter	Value	Description
b	0.65m	wing span
c	0.174m	chord length
c_f	0.050m	flap length
S	0.1131m ²	wing area
A	3.74	aspect ratio
X_{LE}	-1.21m	location of wing leading edge along i_V axis

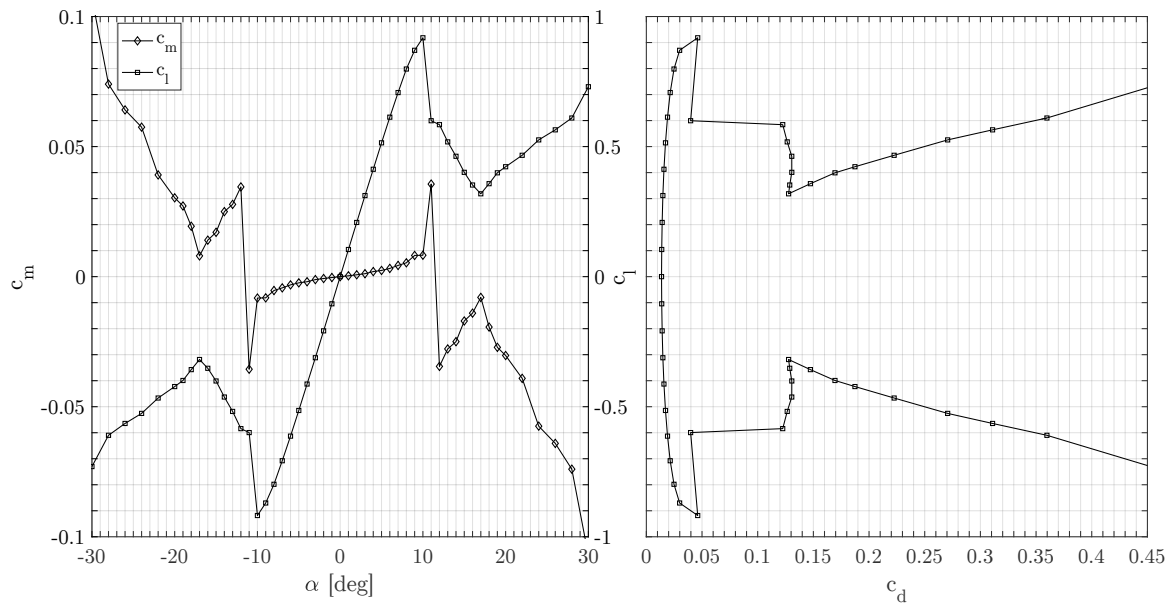


Figure C.4: Section coefficients of the horizontal stabilizer's airfoil (NACA0009) at $Re=168000$

Parameter	Value	Description
\bar{x}_{ac}	0.25	normalized position of aerodynamic chord (a.c.)
t/c	0.09	airfoil thickness ratio
i_H	0deg	wing incidence
c_{la}	5.90rad ⁻¹	section lift effectiveness
η	0.939	airfoil efficiency factor

Parameter	Value	Description
k	0.639	lift correction for 3D-wing
e	0.976	Oswald efficiency number
X_{ac}	0.0435	location of a.c. of 3D-wing
$c_{l\delta_E}$	4.0rad ⁻¹	flap lift effectiveness
$c_{m\delta_E}$	-0.645rad ⁻¹	flap moment effectiveness

C.3 Vertical Stabilizer

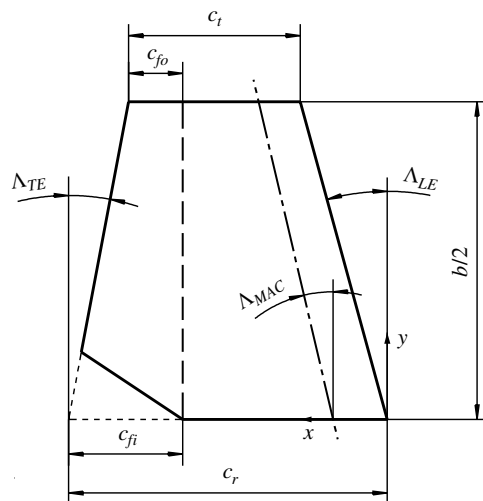


Figure C.5: Vertical stabilizer geometric properties

Parameter	Value	Description
b	0.56m	wing span
c_r	0.200m	root chord length
c_t	0.115m	tip chord length
c_{fi}	0.070m	flap inner length
c_{fo}	0.040m	flap outer length
S	0.0441m ²	wing area

Parameter	Value	Description
A	3.56	aspect ratio
λ	0.575	taper ratio
\bar{c}	0.161m	mean aerodynamic chord (MAC)
y_{MAC}	0.128m	spanwise location of MAC
Λ_{LE}	11.1deg	sweep angle of leading edge
Λ_{TE}	-6.12deg	sweep angle of trailing edge
Λ_{MAC}	6.87deg	sweep angle of MAC
X_{LE}	-1.21m	location of wing leading edge along i_V axis

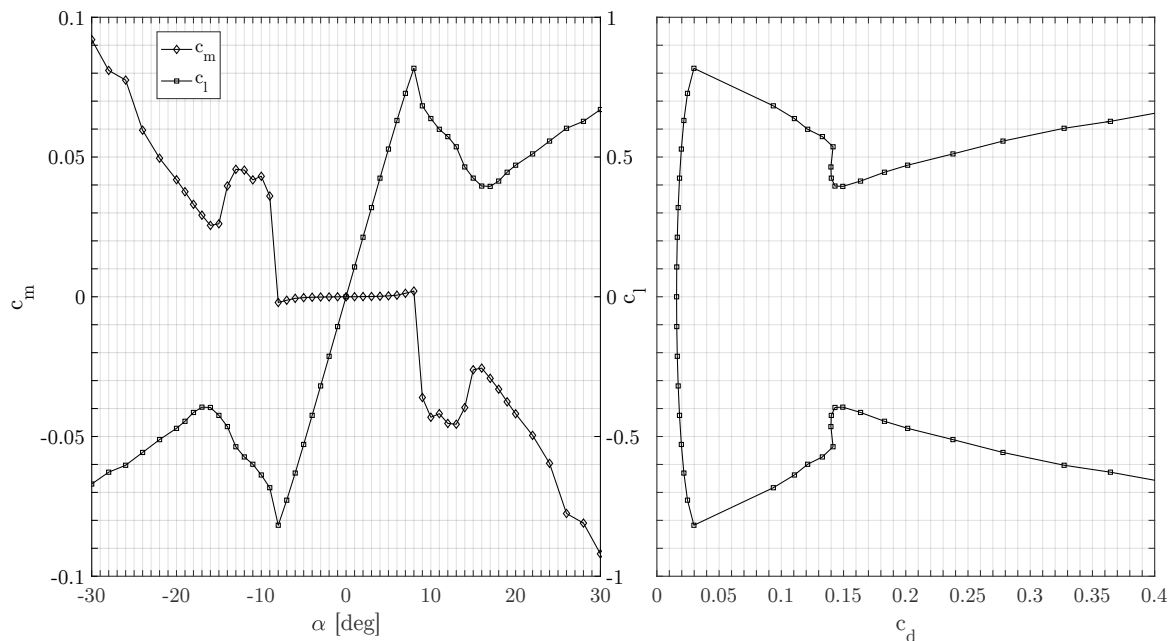


Figure C.6: Section coefficients of the vertical stabilizer's airfoil at $Re=152000$

Parameter	Value	Description
\bar{x}_{ac}	0.25	normalized position of aerodynamic chord (a.c.)
t	0.01m	airfoil thickness (const.)

Parameter	Value	Description
$c_{l\alpha}$	6.07rad ⁻¹	section lift effectiveness
η	0.966	airfoil efficiency factor
k	0.639	lift correction for 3D-wing
e	0.995	Oswald efficiency number
X_{ac}	0.0654m	location of a.c. of 3D-wing
$c_{l\delta_R}$	4.5rad ⁻¹	flap lift effectiveness
$c_{m\delta_R}$	-0.620rad ⁻¹	flap moment effectiveness

C.4 Parasitic Drag

The remaining drag of the airplane is estimated according to [7, pp.237-239]:

Body	c_d	S_d [m ²]	$c_d \cdot S_d$ [m ²]
Fuselage	0.20	0.0141	0.0028
Landing gear	0.15	0.0045	0.00068
2 Main wheels	0.35	0.011	0.0039
Tailgear + wheel	0.30	0.0013	0.0004
Antennas	2.0	0.00069	0.0014
4 Control horns	0.2	0.0010	0.0002
3 Servos + linkage	1.1	0.0015	0.0017
Air Data Sensor Unit	0.1	0.0041	0.00041
Motor	0.5	0.0028	0.0014
Σ			0.01289

$$C_{DF} = \frac{\sum (c_d \cdot S_d)}{S_W} = 0.029 \quad \text{from [7, pp.239]}$$

C.5 Aerodynamic Coefficients of the Vehicle

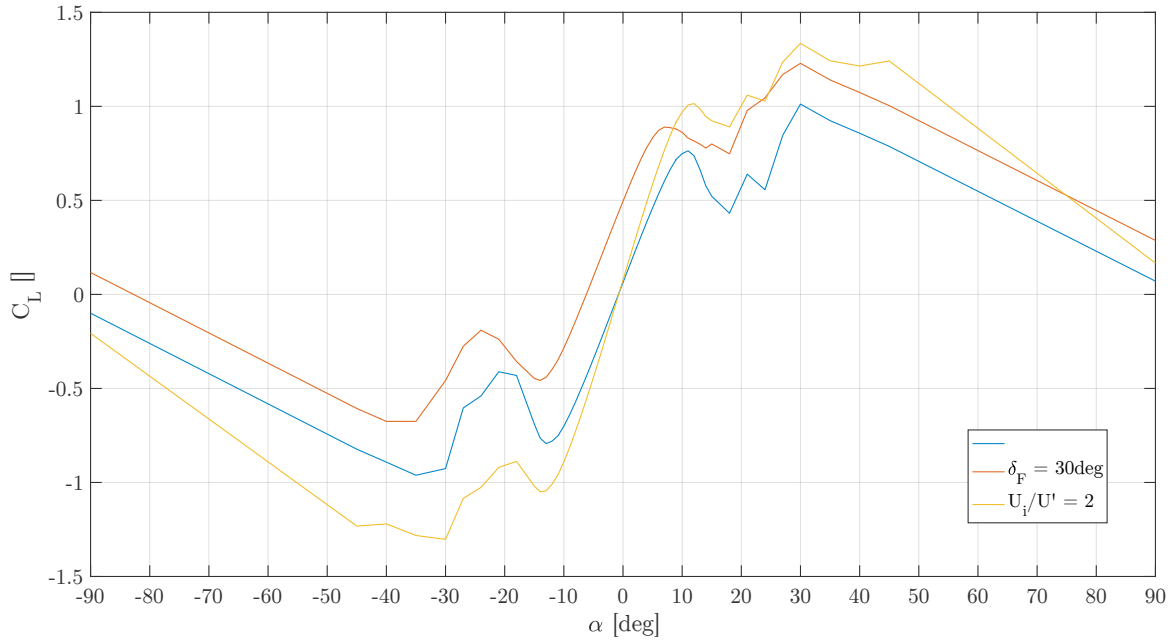


Figure C.7: Vehicle lift coefficient in dependence of the AOA; (blue) base curve; (red) flaps full down; (yellow) maximum propwash effect

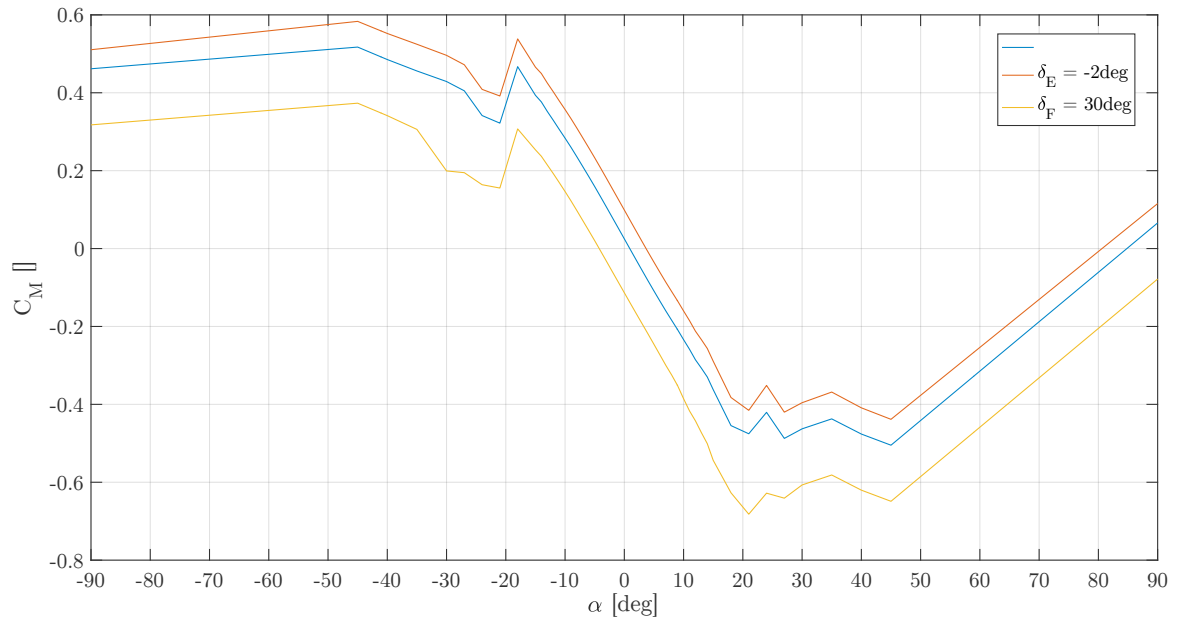


Figure C.8: Vehicle pitching moment coefficient in dependence of the AOA; (blue) base curve; (red) elevator 2 degrees up; (yellow) flaps full down

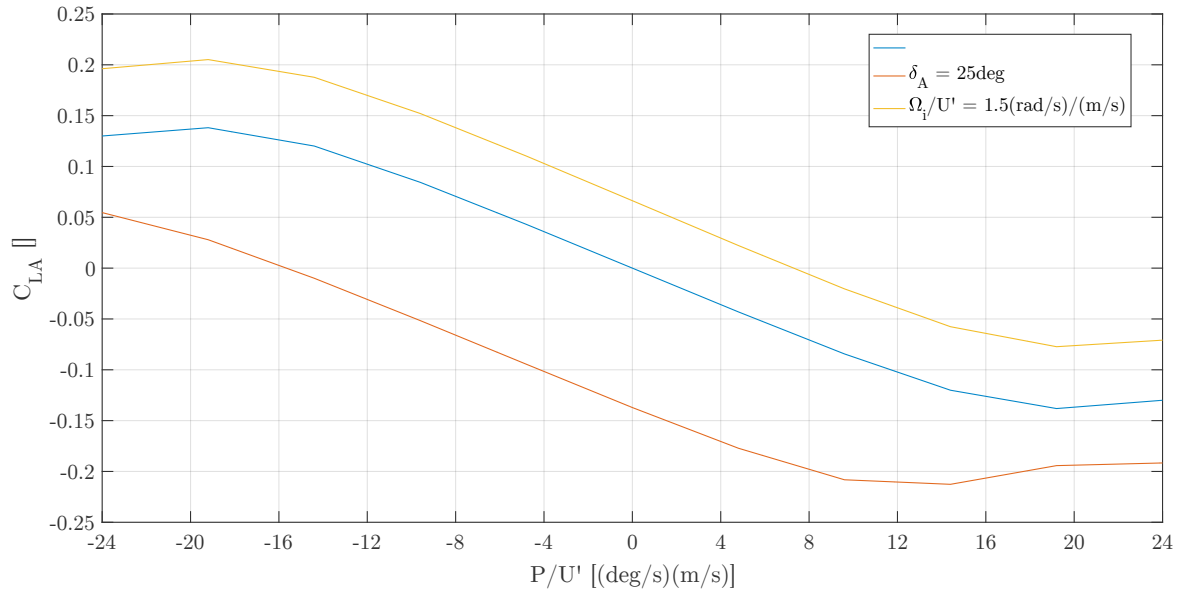


Figure C.9: Vehicle rolling moment coefficient in dependence of the roll rate per axial airspeed; (blue) base curve; (red) aileron full left; (yellow) maximum propwash effect

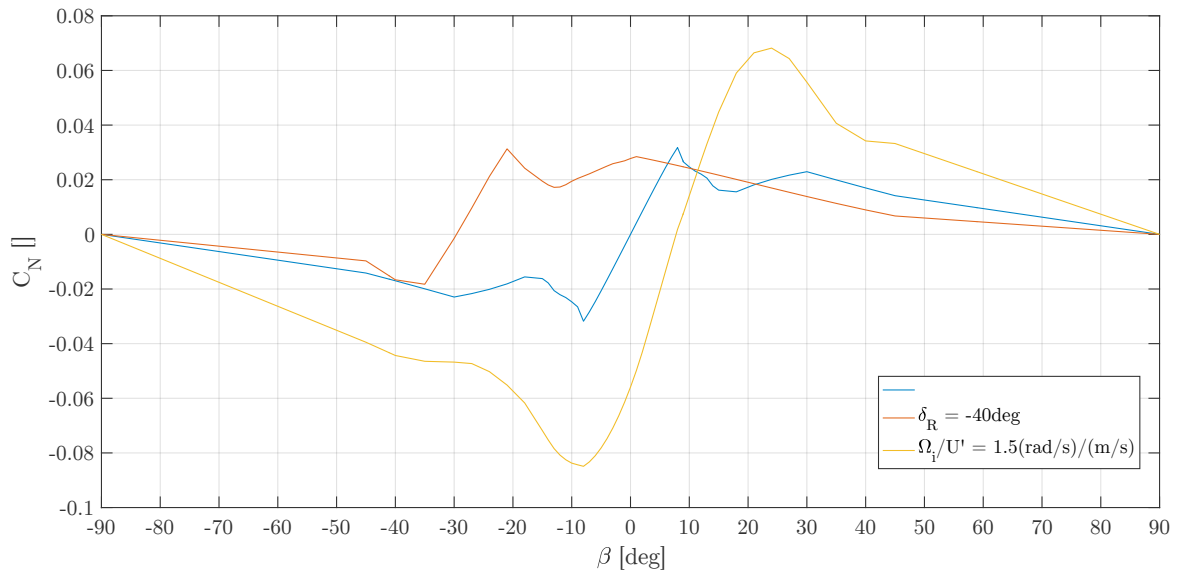


Figure C.10: Vehicle yawing moment coefficient in dependence of the sideslip angle; (blue) base curve; (red) rudder full right; (yellow) maximum propwash effect

Appendix D

INS Parameters

Accelerometer calibration parameters and covariance matrix:

$$C = \begin{bmatrix} 9.8459 \cdot 10^{-1} & 8.0660 \cdot 10^{-4} & -2.3062 \cdot 10^{-2} \\ -3.3592 \cdot 10^{-3} & 1.0027 & 2.4024 \cdot 10^{-3} \\ 4.9667 \cdot 10^{-3} & -3.3054 \cdot 10^{-3} & 1.0109 \end{bmatrix}$$

$$f_0^V = \begin{bmatrix} -7.6722 \cdot 10^{-2} \\ -8.5341 \cdot 10^{-2} \\ -7.2458e \cdot 10^{-2} \end{bmatrix} \frac{m}{s^2}$$

$$\sigma_f^2 = \begin{bmatrix} 4.4 & 0 & 0 \\ 0 & 44 & 0 \\ 0 & 0 & 15 \end{bmatrix} \frac{m^2}{s^4}$$

Magnetometer calibration parameters and covariance matrix:

$$C = \begin{bmatrix} 1.0491 & 1.7427 \cdot 10^{-2} & 1.7537 \cdot 10^{-2} \\ -1.7268 \cdot 10^{-2} & 1.0827 & -9.2422 \cdot 10^{-3} \\ -4.1222e \cdot 10^{-2} & 3.3487 \cdot 10^{-3} & 1.0721 \end{bmatrix}$$

$$B_0^V = \begin{bmatrix} -1.0318 \cdot 10^{-4} \\ -6.9476 \cdot 10^{-5} \\ -7.3740 \cdot 10^{-5} \end{bmatrix} T$$

$$B_I^V = \begin{bmatrix} 8.2807 \cdot 10^{-9} \\ 1.2813 \cdot 10^{-8} \\ -2.3106 \cdot 10^{-8} \end{bmatrix} \frac{T}{A}$$

$$\sigma_B^2 = \begin{bmatrix} 1.5 \cdot 10^{-12} & 0 & 0 \\ 0 & 3.5 \cdot 10^{-12} & 0 \\ 0 & 0 & 4.7 \cdot 10^{-12} \end{bmatrix} T^2$$

Gyroscope calibration parameters and covariance matrix:

$$C = \begin{bmatrix} 1.0313 & -1.1339 \cdot 10^{-2} & -7.2564 \cdot 10^{-3} \\ -7.8347 \cdot 10^{-3} & 9.8760 \cdot 10^{-1} & 7.4846 \cdot 10^{-3} \\ 1.9856 \cdot 10^{-3} & 6.5120 \cdot 10^{-4} & 1.0242 \end{bmatrix}$$

$$\omega_0^V = \begin{bmatrix} 6.9040 \cdot 10^{-2} \\ -4.8245 \cdot 10^{-2} \\ 4.1435 \cdot 10^{-3} \end{bmatrix} \frac{\text{rad}}{\text{s}}$$

$$G = \begin{bmatrix} 1.0539 \cdot 10^{-3} & 0 & 0 \\ 0 & 9.4485 \cdot 10^{-4} & 0 \\ 0 & 0 & 1.2274 \cdot 10^{-3} \end{bmatrix}$$

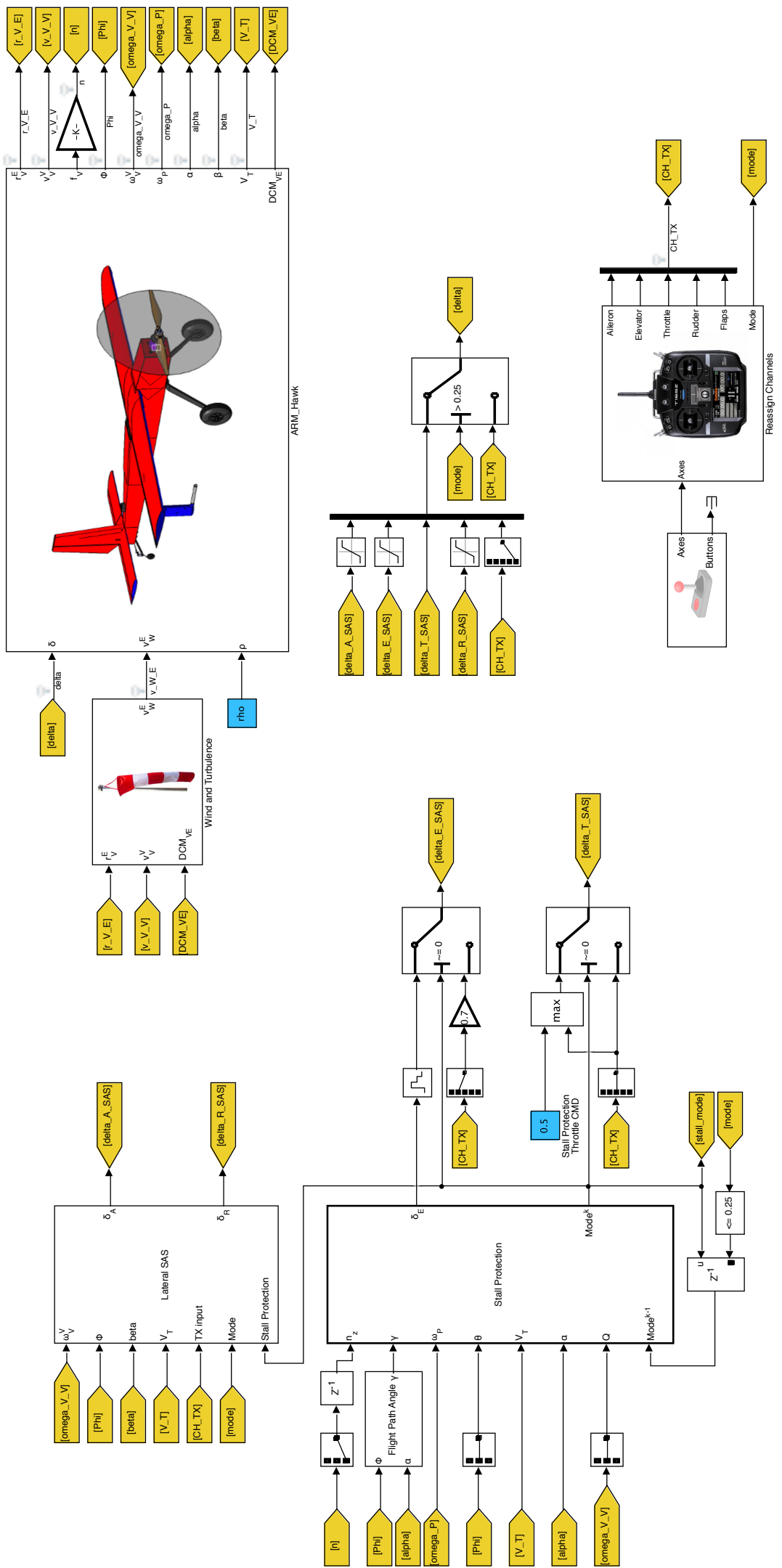
$$\sigma_\omega^2 = \begin{bmatrix} 3.3 \cdot 10^{-2} & 0 & 0 \\ 0 & 7.4 \cdot 10^{-3} & 0 \\ 0 & 0 & 3.4 \cdot 10^{-4} \end{bmatrix} \frac{\text{rad}^2}{\text{s}^2}$$

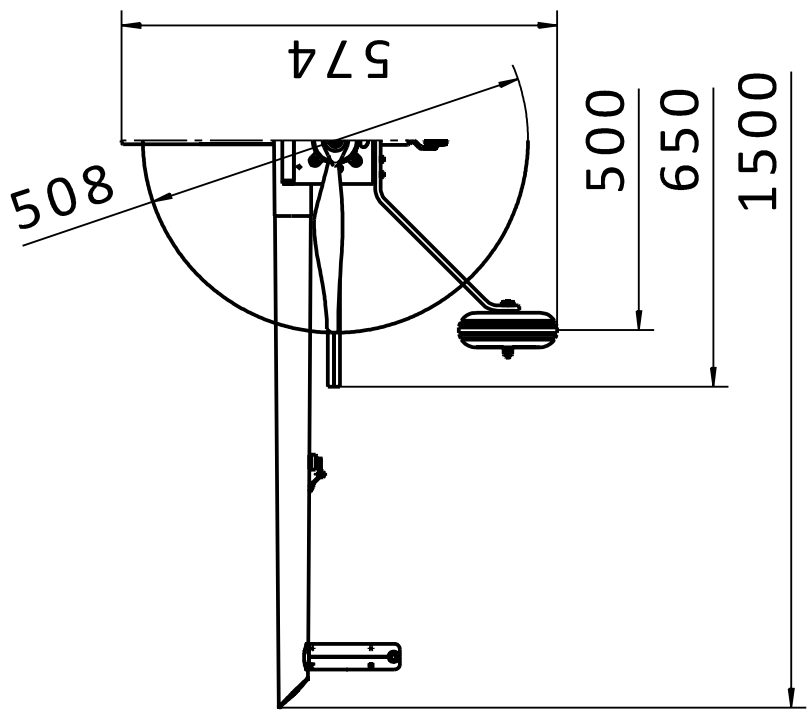
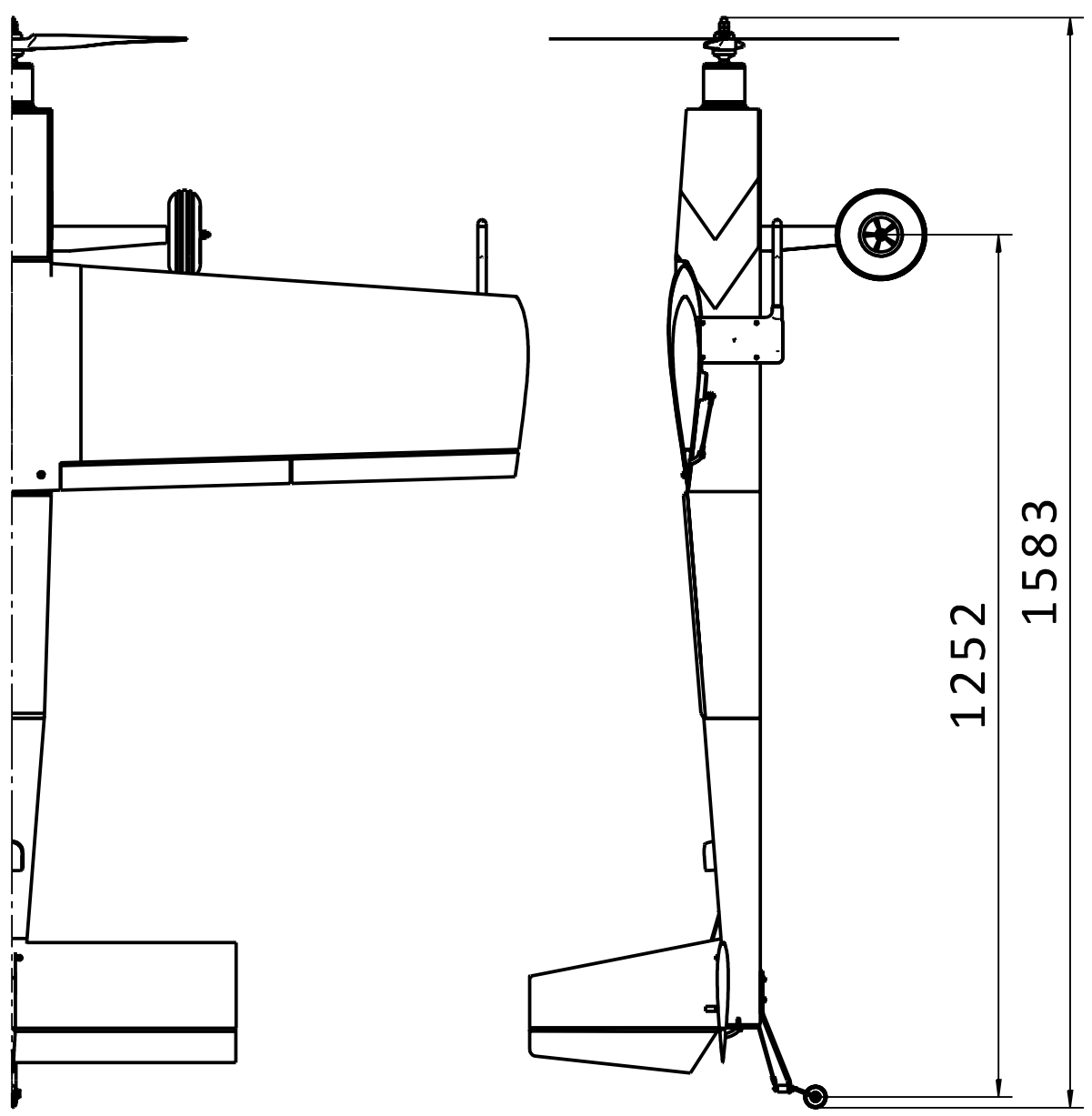
Position measurement (GPS and Barometer) covariance matrix:

$$\sigma_r^2 = \begin{bmatrix} 0.32 & 0 & 0 \\ 0 & 0.32 & 0 \\ 0 & 0 & 0.0625 \end{bmatrix} \text{m}^2$$

Attitude measurement covariance matrix:

$$\sigma_\Phi^2 = \begin{bmatrix} 0.32 & 0 & 0 \\ 0 & 0.051 & 0 \\ 0 & 0 & 0.032 \end{bmatrix} \text{rad}^2$$

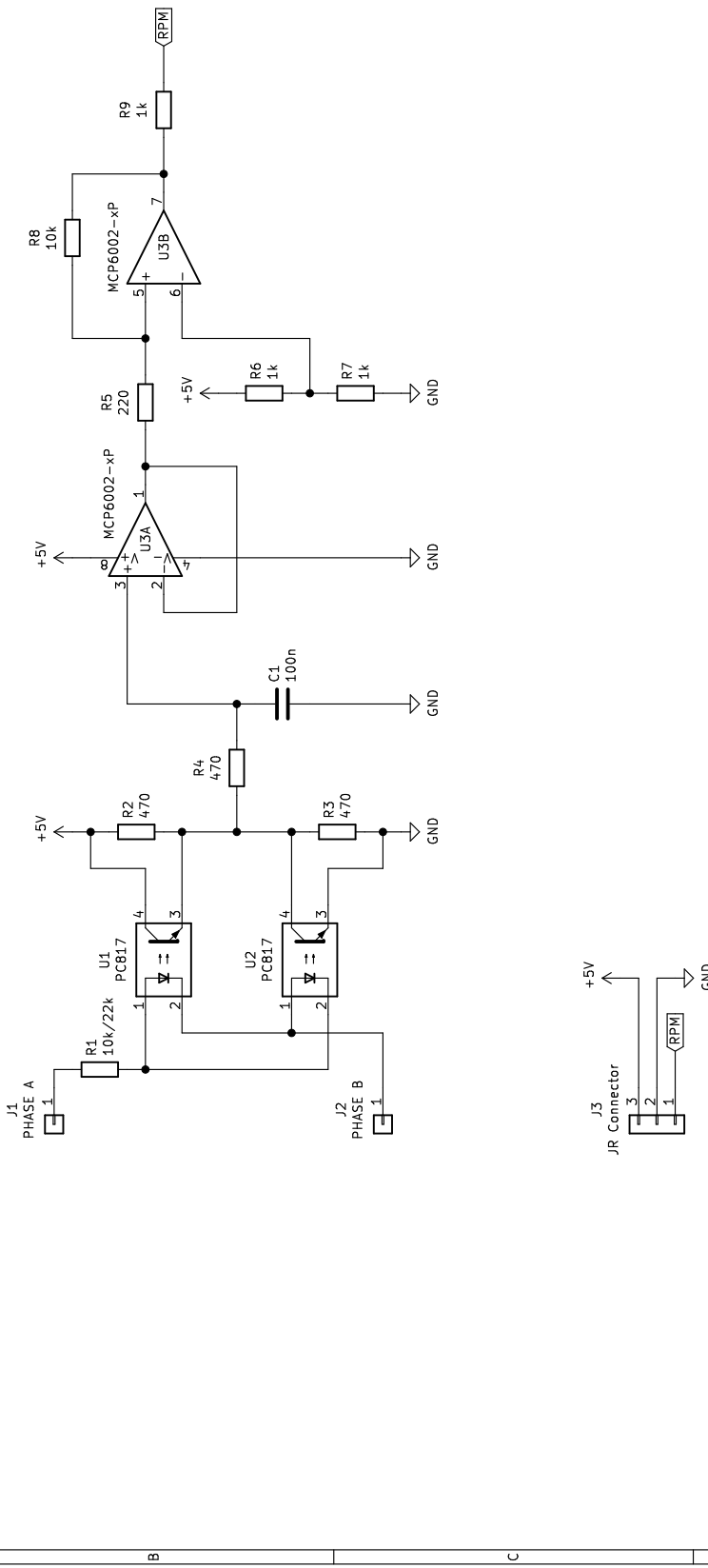




Scale: 1:10	ARM-Hawk	Name: Daniel Pusztai
Drawing Nr.: ARM-Hawk-01-00	Date: 06.11.2018	

$$\begin{aligned} R_1 &= 10k \quad \dots \quad 2S - 6S \\ R_1 &= 22k \quad \dots \quad 7S - 14S \end{aligned}$$

U3C MCP6002-xP



Daniel Puszta

Sheet: /
File: Brushless_RPM_sensor.sch

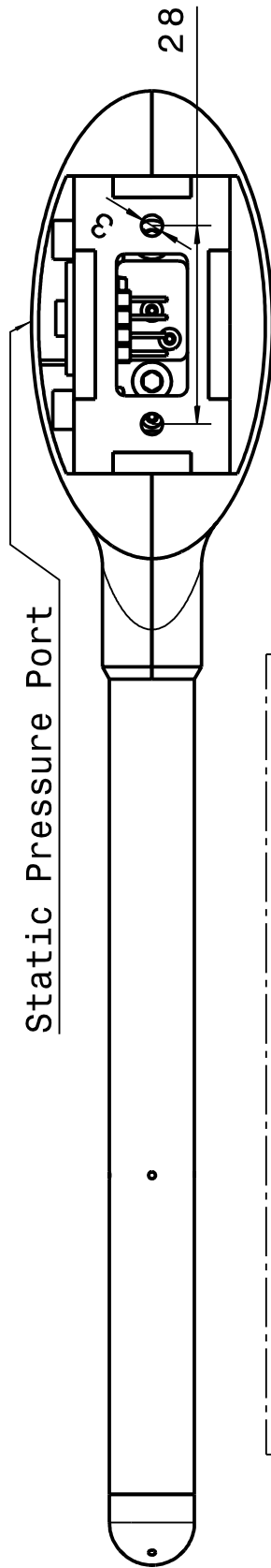
Title: Brushless RPM sensor

Size: A4 Date: 2018-09-04
KiCad E.D.A. eschema (5.0.0-3-95eb66b6) Rev: 1.0
Id: 1/1

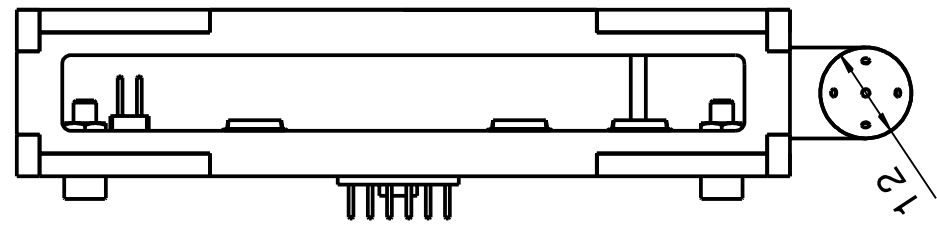
1 2 3 4 5 6

1 2 3 4 5 6

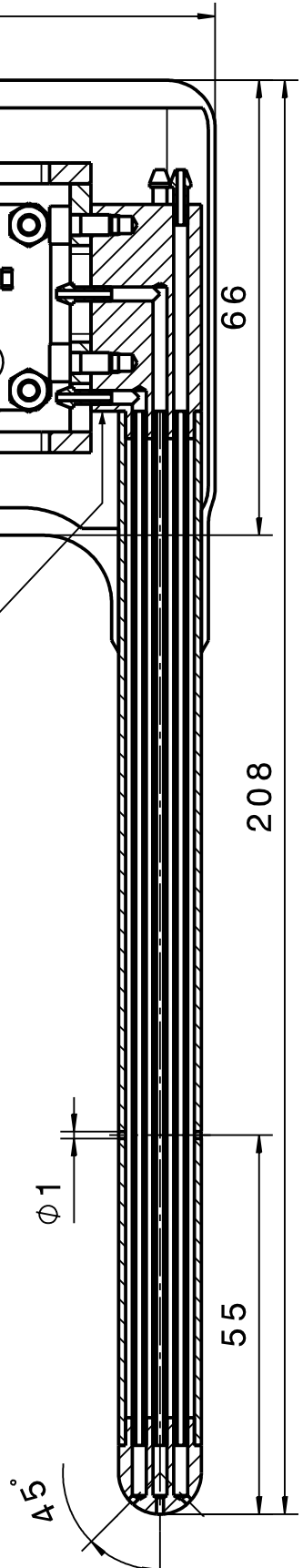
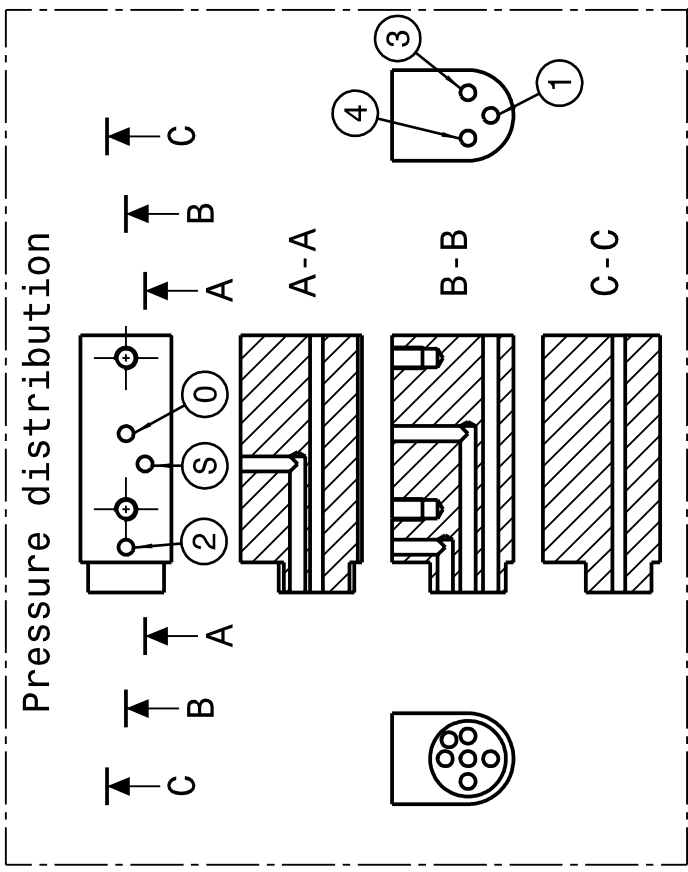
Static Pressure Port



View without
housing:



Pressure distribution



Metal parts glued together with anaerobic glue
(e.g. Loctite 648)

Mount pieces (glassfibre) glued together with
slow curring epoxy (e.g. Loctite EA 9466)

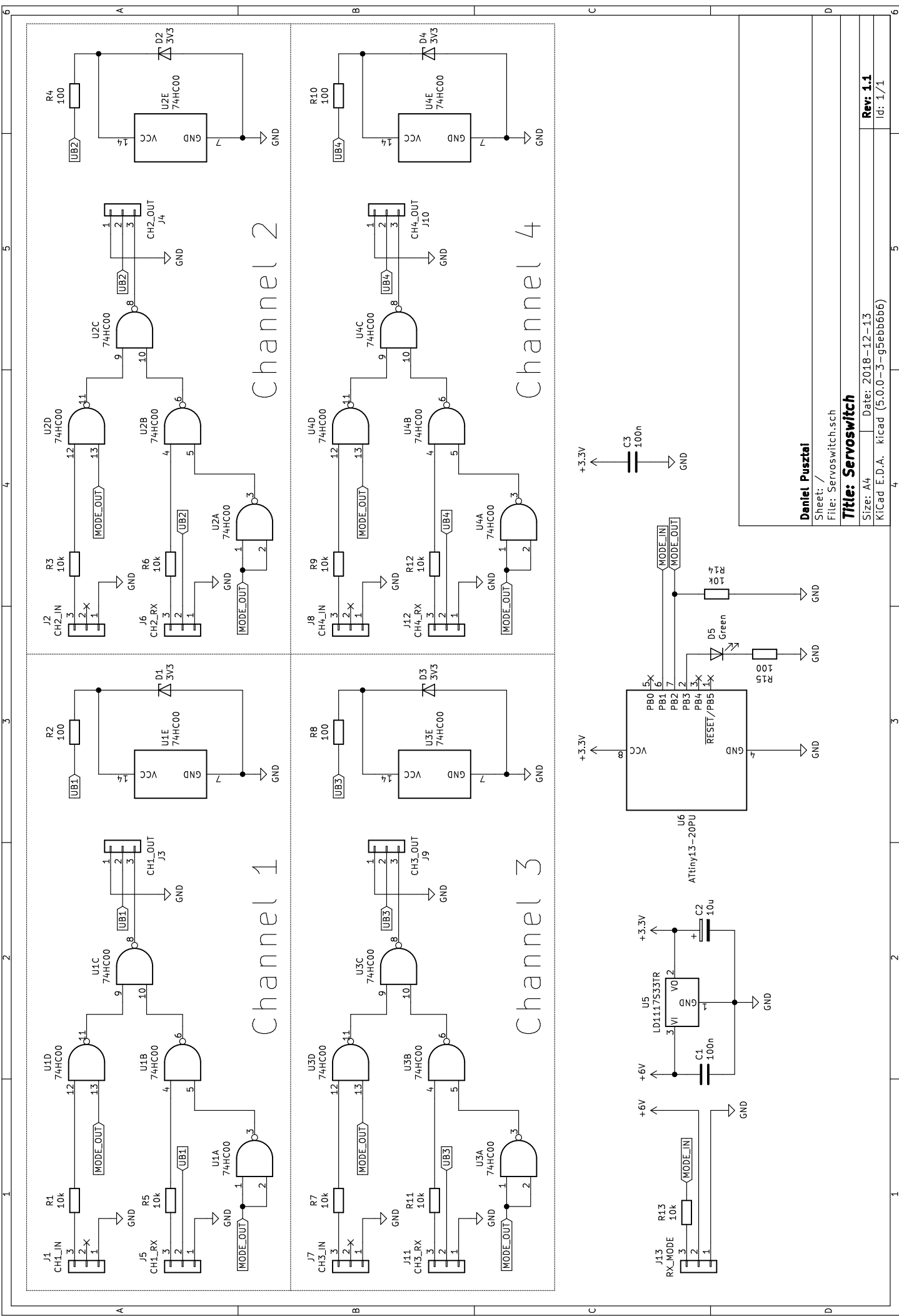
5-Hole Probe

Scale:
1:1

Drawing Nr.:
ARM-Hawk-02-00

Name:
Daniel Pusztai

Date:
04.02.2018



References

- [1] Brockhaus, R., Alles, W. and Luckner, R. (2011). *Flugregelung*. 3rd ed. New York: Springer
- [2] Stevens, B. L., Lewis, F. L. and Johnson, E. N. (2016). *Aircraft Control and Simulation*. 3rd ed. New Jersey: John Wiley & Sons.
- [3] Schmidt, D. K. (2012). *Modern Flight Dynamics*. New York: McGraw-Hill.
- [4] Barlow, J. B., Rae, W. H. and Pope, A. (1999). *Low-Speed Wind Tunnel Testing*. 3rd ed. New York: John Wiley & Sons.
- [5] Bohl, W. and Elmendorf, W. (2014). *Technische Strömungslehre*. 15th ed. Würzburg: Vogel Verlag.
- [6] Kuhlmann, H. (2014). *Strömungsmechanik*. 2nd ed. Hallbergmoos: Pearson Deutschland.
- [7] Dubs, F. (1987). *Aerodynamik der reinen Unterschallströmung*. 5th ed. Basel: Birkhäuser Verlag.
- [8] Bronstein, I. N., Semendjajew, K. A., Musiol, G. and Mühlig, H. (2016). *Taschenbuch der Mathematik*. 10th ed. Haan-Gruiten: Europa-Lehrmittel.
- [9] Lefferts, E. J., Merkley, F. L. and Shuster, M. D. (1982). *Kalman Filtering for Spacecraft Attitude Estimation*. Journal of Guidance and Control, Vol. 5, Sept.-Oct 1982.
- [10] Nise, N. S. (2011). *Control Systems Engineering*. 6th ed. New Jersey: John Wiley & Sons.
- [11] Fadali, M. S. and Visioli, A. (2013). *Digital Control Engineering*. 2nd ed. Waltham: Elsevier
- [12] Allred, R. (2015). *Digital Filters for Everyone*. 3rd ed. West Melbourne: Creative Arts & Sciences House